


1-1-2014

The Application Of Graphene Films In Biosensing And Electrowetting

Xuebin Tan
Wayne State University,

Follow this and additional works at: http://digitalcommons.wayne.edu/oa_dissertations

 Part of the [Biomedical Engineering and Bioengineering Commons](#), [Electrical and Computer Engineering Commons](#), and the [Nanoscience and Nanotechnology Commons](#)

Recommended Citation

Tan, Xuebin, "The Application Of Graphene Films In Biosensing And Electrowetting" (2014). *Wayne State University Dissertations*. Paper 928.

This Open Access Dissertation is brought to you for free and open access by DigitalCommons@WayneState. It has been accepted for inclusion in Wayne State University Dissertations by an authorized administrator of DigitalCommons@WayneState.

**THE APPLICATION OF GRAPHENE FILMS IN BIOSENSING AND
ELECTROWETTING**

by

XUEBIN TAN

DISSERTATION

Submitted to the Graduate School

of Wayne State University,

Detroit, Michigan

in partial fulfillment of the requirements

for the degree of

DOCTOR OF PHILOSOPHY

2014

MAJOR: ELECTRICAL ENGINEERING

Approved by:

Advisor

Date

© COPYRIGHT BY

XUEBIN TAN

2014

All Rights Reserved

DEDICATION

To my family

ACKNOWLEDGEMENTS

First of all, I want to thank my advisor Dr. Mark Ming-Cheng Cheng. You taught me not only how to do research, but also helped me to develop scientific abilities which will benefit my future career. I really appreciate all your contributions of time, ideas, and funding to my Ph.D. Your enthusiasm and persistence for the research was contagious and motivational for me. I feel so lucky to have spent my graduate student life under the guidance of you. It is my great honor to be your first Ph.D. student.

I want thank all the help and company I received from the members of Dr. Cheng's lab: Hyeun Joong Yoon, Chad Huard, Wasif Khan, Ming-Wei Lin, Jing Yang, Jinho Yang, Peng Zeng, Wenwen Yi, Ali Shahini, Ehsan Majidi, and Jimmy Chen. Not only you helped me with the experiments and result discussion throughout the research, but you have also enriched my life in Michigan. It has been the most precious four years be with you and without the pleasure from being with you, I will not survive for my Ph.D.

I would also like to thank all of my collaborators from other groups and departments at Wayne State University. I owe special thanks to Dr. Zhixian Zhou and his's group, who contribute so much for the part of graphene sensing. Dr. Zhou always gave me great suggestions not only about experiment but also the paper writing. Ming-Wei and "Ben" Hsun-Jen are the truly experts in e-beam lithography and I learned a lot from them about how to make nice graphene nano ribbons with EBL. Bhim and Perera are always helpful when I want to use the semiconductor parameter analyzer system and probe station. I also enjoyed the time working with other members in his lab: Cheng Ling, Jin Jin, Lezhang Liu, Qing Lan, Chongyu Wang, and Kulwinder Dhindsa. Thanks to Dr. Gregory Auner for offering me the access of measurement for ellipsometry, probe station,

faraday cage, and XPS. Thanks to Gopakumar and Razieh from Dr. Amar Basu's lab for the help of microscope and microfluidics test. Thanks to Hongen and Yating from Dr. Yong Xu's lab for the help of electrical measurement and Parylene deposition system. Thanks to Gayathri from Dr. Yifan Zhang's lab for providing me the bacteria and phage samples. Thanks to Lingxiao, Li Li, Yi Zou and Sunxi from Dr. Guangzhao Mao's lab for the AFM and zeta potential measurements. Thanks to Lixin and Rhet from Dr. Simon Ng's lab for the help of impedance measurements with potentiostat. Thanks to my previous committee member, Dr. James Granneman for supporting my research of cell sorter and cell perfusion chamber. Thanks to Dr. Mike Mei from CIF for teaching me how to use the SEM. Thanks to Dr. Song Xu from Agilent for the training of AFM. I also thank Mr. Bill funk and Mr. Dan Durisin from ECE for the help in clean room.

In additional, I want to thank all my friends at Wayne State University: Junhui Zhao, Yi Wan, Jia Rao, Jiayi Hu, Hai Jin, Jiayu Gong, Xiao Liu, and Jinqiao Wang, Na Zhu, Kan Zha, Yiyang Zhang and the Chinese student basketball association. I have had great moment with you during my Ph.D.

I want to say special thanks to my mother Weiping Wu and my father Jianping Tan, for your constant, unconditional love, support and understanding during all these years, which become the source of my power to pursue my life and dreams. Finally, my loving thanks to Jing for being with me through all the past 10 years, from college to finishing my dissertation, sharing the bitterness and happiness of life. Making you happy is my sole motivation to achieve anything.

TABLE OF CONTENTS

Dedication	ii
Acknowledgements.....	iii
List of Tables	ix
List of Figures	x
CHAPTER 1 INTRODUCTION OF GRAPHENE.....	1
1.1 Properties of graphene.....	1
1.1.1 Electronic property of graphene	1
1.1.2 Mechanical property of graphene	5
1.1.3 Optical property of graphene	6
1.1.4 Electrochemical property.....	7
1.2 Fabrication of graphene.....	8
1.2.1 Mechanical exfoliation method	9
1.2.2 Chemical Vapor Deposition (CVD) method	9
1.3 Characterization of graphene	10
1.3.1 Optical microscope	10
1.3.2 Atomic force microscope (AFM)	11
1.3.3 Raman spectroscopy	11
1.4 Application of CVD graphene.....	13
1.4.1 Sensing with graphene.....	13

1.4.2 Transparent, flexible, and conducting electrode.....	16
1.5 Scope of this thesis	17
CHAPTER 2 EDGE EFFECTS ON THE pH RESPONSE OF GRAPHENE-NANORIBBON FIELD-EFFECT TRANSISTORS	19
2.1 Introduction	19
2.2 Fabrication process of FET devices made of graphene nanoribbons.....	22
2.3 Results and discussion.....	24
2.3.1 I-V characteristic before edge patterning with different pH.....	24
2.3.2 pH response to the intrinsic defects related to Raman.....	27
2.3.4 Statistic results of pH response with different ribbon edge to surface ratio.....	30
2.4 Summary	31
CHAPTER 3 GRAPHENE BASED BIOSENSOR FOR BACTERIA DETECTION	33
3.1 Introduction	33
3.2 Methods.....	34
3.2.1 Preparation of CVD	34
3.2.2 Device Fabrication.....	35
3.2.3 Zeta Potential measurement.....	37
3.2.4 Immobilization of <i>E.Coli</i> TSPs on graphene surface	38
3.2.5 Device Testing	39
3.3 Results and discussion.....	40

3.3.1 Zeta Potential	40
3.3.2 Electrical testing	40
3.3.3 Sensitivity	44
3.4 Summary	44
CHAPTER 4 ELECTROWETTING ON DIELECTRIC (EWOD) USING GRAPHENE ELECTRODE	46
4.1 Introduction of electrowetting.....	46
4.3 Results and discussion.....	51
4.3.1 Graphene flexible EWOD device structure	51
4.3.2 EWOD performance	52
4.3.3 Electrochemistry modeling of graphene EWOD system.....	55
4.3.4 Leakage current and dielectric breakdown.....	57
4.4 Summary	61
CHAPTER5 DIGITAL MICROFLUIDICS USING GRAPHENE EWOD	62
5.1 Introduction	62
5.2 Experimental methods.....	65
5.3 Results and discussion.....	67
5.4 Summary	73
CHAPTER 6 CONCLUSION AND FUTURE WORK	74
6.1 Conclusion.....	74

6.2 Future work	76
Appendix A.....	77
A.1 Single layer graphene synthesise by CVD.....	77
A.2 Comparison of different CVD graphene Transfer process.....	79
A.2.1 CVD graphene Transfer process by using FeCl ₃ etching	79
A.2.2 CVD graphene Transfer process by using modified RCA clean.....	80
A.3 Graphene sheet patterning	82
A.4 External contact electrode and lift-off.....	85
Appendix B.....	87
B.1 Microfluidics fabrication using PDMS (Polydimethylsiloxane).....	87
Bibliography	89
Abstract.....	110
Autobiographical statement	112

LIST OF TABLES

Table 3.1 Zeta potential of <i>E.coli</i> bacteria, <i>E.coli</i> phage, BSA, and <i>E.coli</i> TSP in tap water.....	41
Table 4.1 Properties of different electrode materials. The optical transmission uses 550nm wavelength as reference.....	49
Table 4.2 Parameters for fitting the Nyquist impedance plot with different electrode materials.....	61

LIST OF FIGURES

Figure 1.1	The structure of graphene (top left), graphite (top right), carbon nanotube (bottom left), and fullerenes.....	3
Figure 1.2	The band structure of the graphene (Left) Electronic dispersion in the honeycomb lattice; (right) zoom in on the energy bands close to one of the Dirac points.....	3
Figure 1.3	A scanning electron microscope (SEM) image shows graphene strain gauge (black) in sharp contrast to the surrounding silicon dioxide (SiO ₂) layer (grey).....	6
Figure 1.4	The optical properties of graphene.....	7
Figure 1.5	Raman spectrum of graphene.....	13
Figure 1.6	Raman mapping of the G line position of the few-layer graphene.....	13
Figure 1.7	Ambipolar electric field effects in single-layer graphene.....	15
Figure 1.8	Working principle of a graphene field effect transistor sensor.....	15
Figure 2.1	Fabrication process of FET devices made of graphene nanoribbons. (a) transfer of CVD graphene onto SiO ₂ /Si substrates; (b) graphene patterning and contact metal deposition; (c) graphene nanoribbon patterning with EBL by using PMMA as the e-beam resist; (d) graphene etching by oxygen plasma; (e) GNR array FET after removing the PMMA.....	22
Figure 2.2	(a) An optical image of graphene FET before edge patterning. The scale bar is 20 μm; (b) schematic illustration of the working principle of electrolyte-gated graphene FET pH sensor; (c) Measured source-drain current density I_{ds} as a function of the top gate reference potential $V_{top-gate}$ in different pH buffer solution for non-patterned pristine graphene FET. (d) the Dirac point shift in response to the different pH. The error bars show the standard deviation of the pH sensitivity.....	24
Figure 2.3	(a) Raman spectrum of the graphene samples with different intrinsic defects; (b) pH sensitivity in response to the Raman peak intensities of G (1588 cm ⁻¹) /D (1344 cm ⁻¹). The error bars show the standard deviation of the pH sensitivity.....	27
Figure 2.4	(a) An image of graphene FET after EBL edge patterning; AFM images to show graphene nanoribbons (b) The drain-source current density I_{ds} as a function of the top gate reference potential $V_{top-gate}$ in different pH buffer solutions for FET made of 100 nm width graphene nanoribbons.	

(c) The Dirac point shift in response to the different pH. The error bars shows the standard deviation of the pH sensitivity.....	28
Figure 2.5 (a) A histogram of sensitivity for the FETs with pristine graphene and graphene ribbons of various widths, Sensitivity of different devices (mV/pH); (b) average pH sensitivity with different edge to surface area ratio. The error bars show the standard deviations.....	30
Figure 3.1 Process flow of device fabrication. (a) CVD graphene growth on copper foil, (b) oxygen plasma etching to remove the backside graphene with a spin-coated PMMA on the top side, (c) wet etching to remove the copper, (d) transfer PMMA/graphene to silicon substrate with thermal oxide, (e) remove PMMA, (f) graphene patterning and contact electrode deposition with e-beam evaporation.....	35
Figure 3.2 Graphene bacteria sensor device structure and testing setup. (a) Optical image of the whole graphene FET device for bacteria sensor, (b) test setup for sensor device, (c) (d) zoom-in microscope images of the device structure, (e) Raman spectrum of the CVD graphene.....	36
Figure 3.3 Chemical reaction mechanism of graphene surface functionalization (a) oxygen plasma to introduce the surface oxygen and hydroxyl group, (b) ATPES reaction to introduce the amine group, (c) glutaraldehyde (GA) to introduce the carboxyl group, (d) <i>E.coli</i> TSPs immobilization with the carboxyl groups, (e) 1% BSA was applied after step d for blocking the unconjugated sites, (f) <i>E.coli</i> bacteria specific binding with <i>E.coli</i>	38
Figure 3.4 (a) I-V curve after <i>salmonella</i> bacteria, show no binding of bacteria, (b) optical microscope image of the device after <i>salmonella</i> bacteria binding.....	42
Figure 3.5 (a) I-V curve after <i>E.coli</i> bacteria, show Dirac point shifted around 20 mV to the left; (b) optical microscope image of the device after <i>E.coli</i> bacteria binding showed there are about 33 ± 2 bacteria counts.....	43
Figure 3.6 (a) I-V curve after <i>E.coli</i> and <i>salmonella</i> bacteria binding, showed no obvious shift after <i>salmonella</i> bacteria binding; (b) optical microscope image of the device after <i>salmonella</i> bacteria binding showed there are about 27 ± 2 bacteria counts.....	43
Figure 3.7 Dirac point shift in response to the bacteria numbers bind to the graphene FET. 7 devices were counted for obtaining the statistic information. Linear fitting showed that the sensitivity was 1.24 mV/ <i>E.coli</i> bacteria.....	44
Figure 4.1 A schematic view of EWOD on a flexible and optically transparent	

graphene electrode.....	51
Figure 4.2 (a) and (b) Two types of EWOD devices with graphene electrodes and Cr/Au contact pads; (c) Raman Spectra of CVD graphene.....	52
Figure 4.3 (a) Captured images of contact angle changes of a KCl droplet on a graphene electrode coated with 1 μm Teflon (6% in FC72); (b) Contact angle changes of a KCl droplet (10 mM) as a function of applied AC voltage (0 V~100 V, 1 kHz) on a 1 μm Teflon (6% in FC72) coated graphene. The solid line is the fitting result by using Lippmann-Young equation. The fitting parameters are: $\theta_0=109.45^\circ$, surface tension $\gamma=72.7$ dyn/cm, relative dielectric constant for Teflon layer $\varepsilon=2.1$, the thickness of the Teflon layer $t=0.96\mu\text{m}$ and $\varepsilon_0=8.85 \times 10^{-12}$ F/m.....	53
Figure 4.4 Reversibility tests of contact angles of a droplet (10 mM KCl) in air with AC voltage switched between 15.3 V and 46.9 V. This result shows a reversible contact angle changes for 50 cycles with a 550nm~750nm thick Teflon layer.....	54
Figure 4.5 (a) An equivalent circuit model of EWOD electrode and the Teflon dielectric layer (b) Impedance measurements and simulations on Teflon coated graphene with 100 mM KCl solution. (blue square) 6% Teflon with graphene electrode; (red triangles) 6% Teflon with gold electrode; (c) 6% Teflon coated on gold electrode at 80V; (d) 6% Teflon on graphene electrode at 80V. There were bubbles from the Teflon coated gold electrodes (c) compared to no bubbles in Teflon coated graphene electrodes (d).....	55
Figure 4.6 Leakage current across the EWOD device with different dielectric layers and electrodes. (a) a 3% Teflon layer with gold and graphene electrodes; (b) a 6% Teflon layer with gold and graphene electrodes; (c) Parylene C as a pinhole-free dielectric layer with a 3% Teflon hydrophobic layer; (d) EWOD device with two-layers stacking (Parylene C/3% Teflon dielectric layers) and graphene electrodes. (The thickness of the Parylene C is around 1 μm .).....	57
Figure 4.7 EWOD on curved PET films with a gold electrode (a, b) and a graphene electrodes (c, d) coated with Teflon dielectric layers. (a) A gold electrode on a PET film with a 6% Teflon layer with the applied voltage 0V; (b) A gold electrode on a PET film with a 6% Teflon layer with the applied voltage 60V; (c) A graphene electrode on a PET film with a 6% Teflon layer with the applied voltage 0V; (d) A graphene electrode on a PET film with a 6% Teflon layer with the applied voltage 60V. As the voltage increased, the contact angles on both electrodes decreased. Compared to the gold electrode, the graphene electrode was more stable. There were no bubbles (electrolysis) at a high voltage on Teflon-	

coated graphene. The voltage was AC sinusoidal wave with frequency 1kHz.....	59
Figure 5.1 Droplets separation in EWOD.....	63
Figure 5.2 Schematics of graphene based EWOD microfluidics system.....	64
Figure 5.3 Process flow of bottom electrodes (graphene electrodes). (a) Transfer graphene onto a glass substrate, (b)Pattern graphene electrodes using photolithography and oxygen plasma etching, (c) Lift-off Ti/Au electrodes, (d) Deposit a Parylene C dielectric layer, (e)Spin-coat a Teflon layer, (f) Remove dielectric layers on the Ti/Au contact electrodes. (g) A schematic view of digital microfluidics using graphene electrodes.....	67
Figure 5.4 (a) An optical image of graphene electrodes with Ti/Au contact pads. (b) Zoom-in image of the transparent graphene electrodes on glass. Scale bar: 1mm.....	68
Figure 5.5 Contact angle change on Parylene C/ 3% Teflon coated graphene electrodes. The voltage was from 0V to 84 V, AC 1kHz.....	69
Figure 5.6 A system for leakage current test.....	71
Figure 5.7 Comparison of leakage currents in the dielectric layers using different electrodes. (A)3% Teflon with graphene, (B) 3% Teflon with gold, (C)Parylene C/ 3% Teflon with graphene, (D)Parylene C/ 3% Teflon with gold.....	71
Figure 5.8 Control of droplet movements using graphene based EWOD. The voltage was AC 70V (1kHz) and the droplet was 1.5 μ L KCl (100mM). The droplet moved from the left side to the right side as voltage was sequentially turned on.....	72
Figure 5.9 The droplet movement on graphene EWOD device with square electrodes.....	73
Figure A.1 A typical CVD furnace setup for graphene growth (on copper).....	77
Figure A.2 A typical time dependent CVD experiment condition for graphene growth (flow rate, pressure, temperature).....	78
Figure A.3 An SEM image of CVD graphene after growth on copper foil, the black islands show the multilayer areas.....	79
Figure A.4 A typical CVD graphene wet transfer process by using FeCl ₃	80

Figure A.5 AFM microscope images of CVD graphene transferred on silicon substrate with a 300 nm thick thermal oxide after (a) modified RCA clean with diluted Hydrochloric acid and ammonia solution, the surface is clean and only very few contamination are remaining on the graphene surface (b) graphene transferred with FeCl₃ and without modified RCA clean, showed very rough surface and some residues are still remaining.....81

Figure A.6 (a) CVD graphene transferred onto SiO₂/Si substrate with oxygen plasma, (b) after e-beam patterning, showed the blue stain remain on the substrate.....82

Figure A.7 Optical microscope images of CVD graphene before patterning with photolithography and oxygen plasma etching (top left), after patterning (top right), 2 μm holes array pattern (bottom left), 2 μm wide line pattern (bottom right).....83

Figure A.8 Process flow of the e-beam lithography for writing sub-micron patten on the graphene FET sensor device (left), graphene FET patterned with circular shape holes with PMMA covered (top right), and after remove PMMA(bottom right).....84

Figure A.9 Graphene nano ribbon pattern wrote by EBL with HSQ e-beam resist. The line width was only 100 nm.....85

Figure B.1 A typical fabrication process of the two-layer microfluidics.....87

CHAPTER 1 INTRODUCTION OF GRAPHENE

Carbon materials widely exist in nature world. They have numerous allotropes and some of them are quite familiar to us. For instance, diamond is built through the sp^3 covalent bonds and graphite is known as a form of the sp^2 bonds. Much smaller allotropes were found as a result of the development of nanoscience and nanotechnology. The 1D carbon nanotube[1] and 0D fullerenes [2] were discovered and extensively studied for their unique physical, electronic and chemical properties. The discovery of these new materials extends the variety of the allotropes of the carbon materials and inspires people to explore the fundamental of two-dimensional carbon atom network.

In 2004, Andre Geim and Kostya Novoselov from Manchester University first published the strong electric field effect from an isolated atomic thick carbon film, which was known as graphene.[3] They proposed a simple mechanical exfoliation method to obtain a single layer graphene, which can be produced from raw graphite after breaking its interlayer van der waals force. The research of this sp^2 hybridized carbon material rapidly becomes an exciting topic for studying its extraordinary electrical and mechanical features. The discovery of the graphene is a breakthrough of the two dimensional materials and thus was awarded as the Physics Nobel prize in 2010.[4]

1.1 Properties of graphene

1.1.1 Electronic property of graphene

A pristine single layer graphene is a 2D crystal built by sp^2 hybridized carbon atoms. It is known as the basic unit of other carbon allotropes as shown in figure 1.1. For

example, graphite can be seen as a stack of graphene layers. Graphene can be rolled to a carbon nanotube or wrapped into fullerenes. When graphene was discovered, it exhibits unique electronic properties. Intrinsic graphene is a semi-metal or non-band gap semiconductor. Its bandgap between the valence band and conduction band is zero. Graphene has a ambipolar electric field effect that has not been found in any other metal or semi-metal materials [3]. Because the graphene has a 2D honeycomb lattice, π electrons of the atoms do not interact with each other. These special lattice structure was known to form a band structure (figure 1.2) that had been reported by Wallace in 1947[5]. The valence band and conductance band of the carbon atoms in the single layer graphene systems touch at the neutrality point, also called Dirac point. At the region of low energy, a linear E-k relation is found close to the Dirac points near the Brillouin zone. The Dirac point can be seen as the lowest energy point of the carbon atom in a 2D graphene system. It is interesting that although the π state (valence band) and π^* state (conductance band) are symmetric about the Dirac point, the electrons are not allowed to spin like traditional fermions.[6] Indeed, the spin of electrons in a graphene system has a pseudospin characteristic where electrons can only hop from one atom to its nearest neighbor atoms.[7] In this case, graphene has a Fermi velocity, $v_F = 1 \times 10^6$ m/s and does not affected by the energy or momentum. In an ideal single layer graphene system, the effective mass of electron is zero. This unique characteristic brings in many attractive electronic properties to the graphene such as quantum Hall effect at room temperature, [8] ambipolar electric field effect, [3, 8] extremely high carrier mobility, [9] and near ballistic carrier transportation in integrated circuit (IC) device scale range.[10]

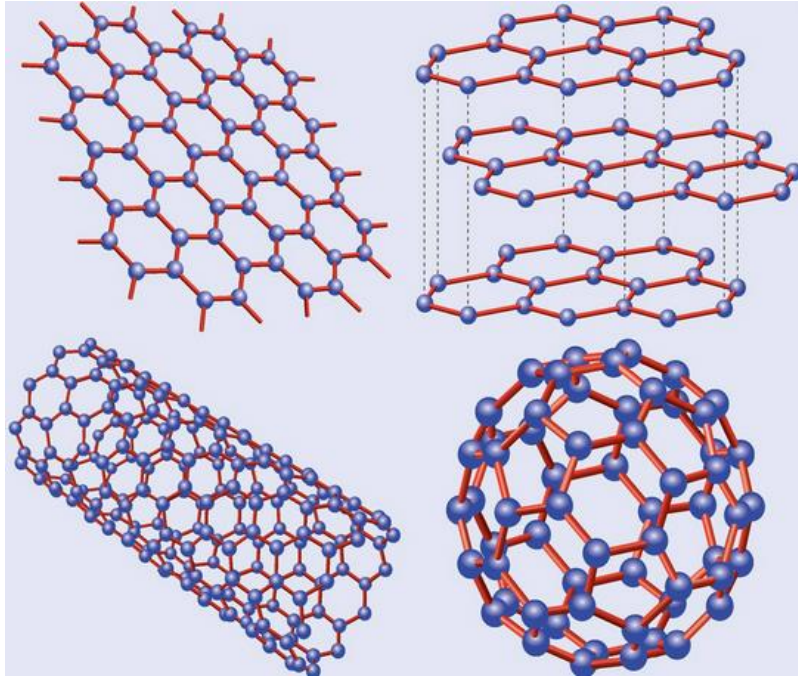


Figure 1.1 The structure of graphene (top left), graphite (top right), carbon nanotube (bottom left), and fullerenes. [11]

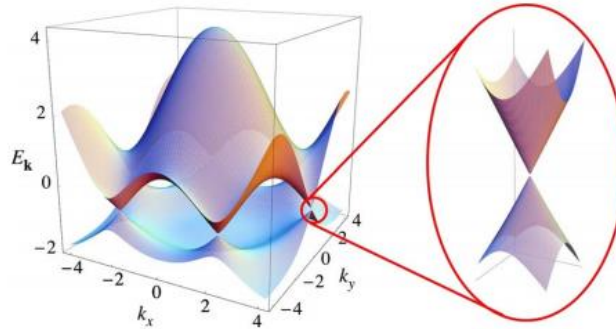


Figure 1.2 The band structure of the graphene (Left) Electronic dispersion in the honeycomb lattice; (right) zoom in on the energy bands close to one of the Dirac points. [10]

The electronic properties of graphene can also be affected by its defects. The defects of graphene can be introduced mainly by three methods: (1) crystal growth, (2) high energy irradiation such as electron beam or ion beam, and (3) chemical treatments. [12] The chemical vapor deposition (CVD) is a popular method to grow polycrystalline graphene. During the CVD process, defect lines are formed around the 2D domains as a

result of the coalesces of the grain boundaries of the two different types of crystals in a metal substrate.[13] These defect lines will reduce the charge carrier mobility and increase the sheet resistance of the graphene. The graphene defects can also be generated by using electron beam irradiation.[14, 15] When the electron beam energy is larger than 18 eV, the carbon atoms in lattice can be ejected out of the graphene or attached to the graphene films as adatoms. Specially, the atoms on the edge have lower energy and are very easy to migrate. Using advanced TEM system (TEAM 0.5 for example, 1Å resolution), Zettl *et al* observed in situ stone-wales defects (carbon rings with 5 or 7 atoms) formation on a suspended graphene film with 80 KV electron beam irradiation. These defects restored to a normal hexagonal ring after the beam was turned off. It is noticed that with continuous radiation of electron-beam, the edge carbon atoms were gradually ejected from the graphene. Using this method, one may obtain arbitrary defects patterns with high resolution (< 5 nm). However, the method is not convenient because of the extremely high vacuum and long writing time of electron-beam. Another method is using ion beams to generate vacancies on suspended graphene. It is shown that the resolution of this method could achieve 10 nm with a focused ion beam.[16] Chemical induced graphene defects are normally done by oxidation treatments with acids such as nitric acid (HNO₃) or sulfuric acid (H₂SO₄). After the treatment, hydroxyl and carboxyl groups will attach on graphene. These chemical groups will act as donors or acceptors, and affect electron transfer in graphene. It is also reported that by plasma treatment, the hydrogen atoms would attach to graphene surfaces and perturb graphene lattice, which leads to the generation of a bandgap in graphene.[17]

1.1.2 Mechanical property of graphene

Graphene is known as one of the strongest materials in the world. A suspended graphene membrane has a Young's modulus of 0.5 TPa, and yield strength of 10^5 MPa.[18] Graphene is stiffer and tougher than silicon and other metals such as steel, aluminum.[19] Unlike traditional bulk materials, a nonlinear elastic response ($\sigma = E\varepsilon + D\varepsilon^2$) was observed in a suspended single layer graphene membrane which corresponds to the existence of both Young's modulus E and third-order elastic modulus D.[18] The mechanic properties of the 2D graphene membrane can be attributed to its strong sp^2 bond energy toward its in-plane direction. Combined with extraordinary electronic and mechanical properties, graphene is suitable for flexible and highly conductive electrodes.[20] Also, the suspended graphene films have the potential to fabricate super sensitive nano-electromechanical system (NEMS) devices that can be used as single molecular sensors, pressure sensors, and RF resonators.[21]

Frank Niklaus *et al* [22] from KTH demonstrate the piezoresistive effect in graphene using a graphene nano-electromechanical membrane configuration that provides direct electrical readout of pressure to strain transduction (figure 1.3). They compared the results with conventional pressure sensors and it shows that the graphene sensors have orders of magnitude higher sensitivity per unit area. They connected the suspended graphene film with the substrates as a gate electrode, and measured the device as a new type of GFET based strain gauge, which has a piezoelectric gauge factor under three. Xu *et al* [23] reported a radio-frequency driven graphene mechanical resonator, which has a resonant frequency of 34 MHz at 77K. A mechanical exfoliated graphene flake was bridged between as-prepared source-drain electrodes. The gate electrode was

defined on a trench between the source and drain and formed a capacitor with the graphene channel. The signal-to-background ratio was demonstrated over 20 dB. Because of the fast response time, graphene RF devices may have potential in the applications of filters and oscillators. The mechanical vibration of graphene sheets can also be visualized by scanning probe microscopy.[24] P.L. McEuen *et al* demonstrated that suspended graphene sheets could be vibrated by an electrostatic force using a RF driving voltage. They also found a nanoscale vibration mode, in which the maximum vibration amplitude happened around the free edges rather than the center of the sheet.

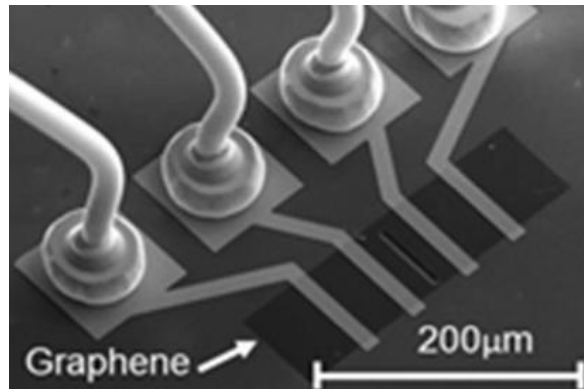


Figure 1.3 A scanning electron microscope (SEM) image shows graphene strain gauge (black) in sharp contrast to the surrounding silicon dioxide (SiO₂) layer (grey).[22]

1.1.3 Optical property of graphene

One of the most interesting properties of graphene is its opacity. It is found that a single layer graphene (~0.34nm) film can absorb a portion ($\pi\alpha=2.3\%$) of light in the visible light range. Here, α is the fine-structure constant and equals to 0.0073. The experimental results also show that the opacity and the layer number N have a linear relationship.[25] The absorption spectrum shows a flat feature from 300nm to 2500nm. The light reflection ability of graphene can be neglected for $R<0.1\%$. The refractive

index of graphene was also reported as $n=2.0-1.1i$ by matching the optical contrast with Fresnel's equation.[20] All of these optical properties of graphene can be attributed to the special conical band gap structure close to the direct point. The graphene itself has no luminescence. However, via bandgap engineering by either size reducing (like nanoribbons) or chemical and physical doping, luminescence has been observed in graphene.[26, 27] The plasmonics of the graphene show unusual behavior that can be used as a tunable terahertz material and a far-infrared detector. [28]

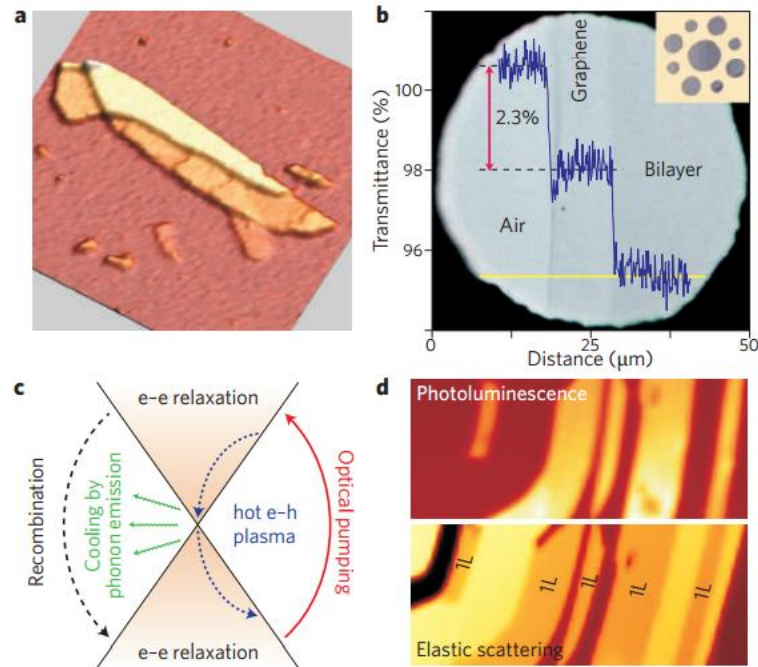


Figure 1.4 The optical properties of graphene. [29]

1.1.4 Electrochemical property

Graphene is known as a promising next-generation material of electrochemical sensing.[30-34] Graphene has similar electrochemistry properties with highly oriented pyrolytic graphite (HOPG) and carbon nanotube materials.[30] The heterogeneous electron transfer in the 2D graphene sheet happens at the edge of graphene rather than the

graphene basal plan [32]. This is because the electron transfer-rate constant on the edges is $k_e=0.01\text{cm/s}$ compared to that on the basal planes $k_b=10^{-9}\text{ cm/s}$. [35] In a defect-free graphene sheet, the sensitivity is actually low. The electrochemistry sensing of the graphene is also affected by oxygen-containing groups at the edges. Reports show that these functional groups will enhance or reduce the sensitivity of the carbon materials. [30] Chou *et al* showed that the electron transfer rate of single-well carbon nanotubes was increased by carboxylic groups. [36] Ji *et al* showed that oxygenated species would decrease the electron transfer rate at the edge of the pyrolytic graphite electrodes. [37] The electron transfer rate can also be affected by the adsorption and desorption of molecules. Advantages of graphene electrochemical sensing are summarized. First, the graphene has excellent electrical conductivity even at a very low doping concentration. Second, compared to other materials such as carbon nanotubes, the 2D structure of graphene provides a larger surface to volume ratio for sensing. And finally, the electrochemical sensing of carbon nanotubes is influenced by metallic impurities because the metal catalysts are typically required in synthesis. [38] Graphene can be fabricated in a simple way such as mechanical exfoliation. It is cheap and can also avoid unexpected contaminations. The graphene-based electrochemical sensor has shown successful detection of cadmium and lead, [39] influenza A H1N1, [35] dopamine, [39] and glucose [40] with enhanced functions by nanoparticles or oxidation.

1.2 Fabrication of graphene

Uniform, high quality and large area graphene films are fundamental for their basic researches and applications. The graphene sheet can be obtained by mechanical

exfoliation,[3] epitaxial growth on SiC,[41, 42] CVD growth on Ni and Copper [43, 44]and chemical reduction of graphite oxide.[45] In our experiment, the first two methods are used to produce graphene samples.

1.2.1 Mechanical exfoliation method

A mechanical-exfoliation method was first introduced by the group from Manchester University.[3] This method is the simplest way to obtain high quality graphene. By peeling off a piece of graphite using a scotch tape and then folding the tape for several times carefully (to break the van der waals forces between the graphene layers in graphite), one can get small pieces of graphene on the tapes. To transfer the graphene flakes onto substrates such as SiO₂/Si, one needs to press the tape gently to stamp the graphene onto the substrates. Both graphene and graphite flakes will be attached to the substrates during this procedure. Thus it requires a lot of patience and skills. Sometime one may get nothing on the substrate or thick graphite (many layers of graphene). The limitations of the mechanical method include low yield and uncontrollable size of the graphene flakes. Thus the method is not suitable for mass production of large quantity of graphene samples.

1.2.2 Chemical Vapor Deposition (CVD) method

Graphene made by a CVD method using nickel (Ni) and copper (Cu) as the catalyst materials have been reported by several groups.[20, 46, 47] For Ni catalyst, when the growth temperature is ramping up to 1000 °C, carbon atoms are thermally decomposed on the Ni surface and partially dissolved into Ni. The precursors are hydrocarbon gases such as methane. Then during the cooling-down process, the carbon

atoms precipitate back onto the Ni surface and form graphene or graphite structure. Nickel has a relatively high solubility to carbon. The cooling-down rate will affect the thickness of graphene, and thus it is hard to achieve single-layer graphene. Ni has a small grain size, which makes it unsuitable to obtain large-area and uniform graphene films with high carrier mobility and conductivity. Compared to Ni, Cu has almost zero solubility to carbon and larger grain sizes.[48] The graphene can form directly on copper surfaces and the thickness is not affected by cooling down rate of the precipitation process of carbon atoms. There are two main advantages of the CVD graphene. First, the method is inexpensive by using methane gas as reaction gases. Second, large area of graphene can be grown by using a CVD method. Currently, the quality of the CVD graphene is not as good as the one made by mechanical exfoliation method because of defects introduced during the fabrication process in CVD growth. After growth of graphene, the underneath metal needs to be etched. Chemical groups from water and organic solvent may cause the doping in graphene during this process. There is a challenge to achieve intrinsic graphene (non-doping) by traditional CVD method. The carrier mobility of CVD graphene sheet is normally lower than that of graphene flakes produced by mechanical exfoliation.

1.3 Characterization of graphene

Here we focus on the physical and electrical properties of CVD graphene and its applications. Several methods are listed for the characterization of the size, quality and 2D crystalline structure of graphene.

1.3.1 Optical microscope

Single layer graphene has been recognized as almost optical transparent (97.7% in visible light range). Nevertheless, it is possible to observe the graphene sample through an optical microscope.[25] [49] According to the Fresnel-law-based model, there is a contrast difference between graphene area and substrate as high as 12% on 100 nm~300 nm thick SiO₂ substrate using the monochromatic illumination. The graphene on a SiO₂ substrate shows a violet-to-purple color, depending on the layer numbers of graphene and the optical source.

1.3.2 Atomic force microscope (AFM)

The thickness of a single layer graphene is only 0.34 nm, and its height information can be measured by an AFM with an angstrom resolution. By using amplitude-modulation AFM with a non-contact mode, the topographies of the graphene samples can be characterized. However, it is challenging to identify a single layer graphene on the substrates that are not flat. Before we took AFM images, the samples need to be cleaned in high temperature annealing in order to remove residues brought by the scotch tapes or PMMA.

1.3.3 Raman spectroscopy

The Raman spectroscopy is a powerful method to characterize the molecular structures of materials. By investigating the vibration or rotation modes related to the molecular system, Raman spectroscopy can identify a molecule by its ‘finger print’. In a typical Raman experiment, the sample molecules are excited by a monochromatic laser. Due to the interaction between the photon and the molecule structure, the photon energy will change and result in a blue or red frequency shift of the original incident light.

In figure 1.5 of the Raman spectrum of graphene, there are two intense bands, G band ($\sim 1580\text{ cm}^{-1}$) and 2D band ($\sim 2700\text{ cm}^{-1}$). [50] The G band can be attributed to the doubly degenerate zone center E_{2g} mode. [51] The 2D band is due to the second order of the two-phonon mode. [52] There is also a band known as D band which can be detected around 1350 cm^{-1} . This band usually refers to the defects of the graphene and cannot be found in pristine graphene. The ratio of the intensity of the G band and 2D band can differentiate the number of layers of graphene. A more accurate method to acquire the topology of a graphene is Raman mapping (figure 1.6). This method can read an area Raman intensity of specific band and allow people to know the properties such as the area and uniformity of the graphene.

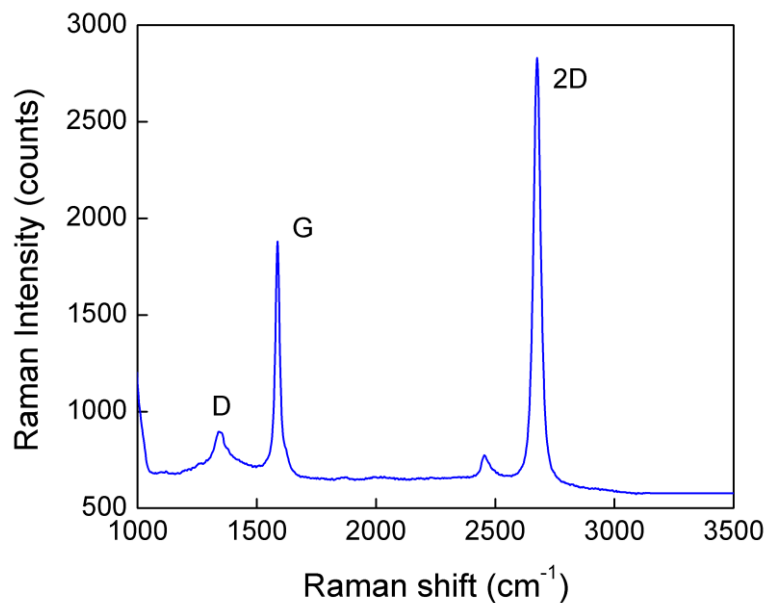


Figure 1.5 Raman spectrum of graphene.

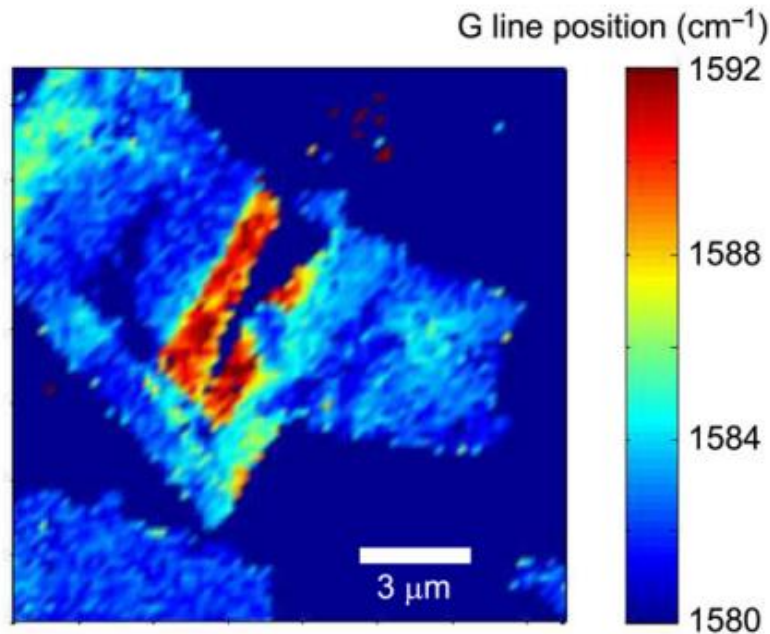


Figure 1.6 Raman mapping of the G line position of the few-layer graphene. [53]

1.4 Application of CVD graphene

1.4.1 Sensing with graphene

Unlike silicon, which is already determined before fabrication as p-type or n-type, graphene has an ambipolar electrical field effect.[3] The doping of the graphene can change from p-type to n-type or n-type to p-type by applying a biased gate voltage. As figure 1.7 shows, the positive gate voltage introduces electrons to the graphene whereas the negative gate voltage introduces holes to the graphene. Ambipolar field effect has been found in some other nanomaterials such as carbon nanotube[54] and silicon nanowires.[55] The conductance of the graphene will change dramatically with these doping near the Dirac point. It is also interesting to find that near the Dirac point where

the carrier density is zero, graphene has a minimum conductance in the order of $\frac{4e^2}{h}$. The phenomenon of minimum conductance is not fully understood yet.[56] Figure 1.8 shows a typical sensor based on graphene field effect transistor (GFET). For an intrinsic graphene field effect transistor, the conductance increases dramatically as the applied back gate voltage changes away from the Dirac point. When a positive gate voltage is applied, the majority carriers in graphene channel are electrons. When a negative gate voltage is applied, the majority carriers become holes in the graphene channel. If there are changes in ion concentration around the graphene channel, the charge carriers of opposite polarity will be introduced into the graphene and affect the I-V curve. In particular, when there are negative charges in the environment, the holes will be introduced into the graphene channel and cause the I-V curve shift to the right. Verse vice; if there are any positive charges, the I-V curve will shift to the left. Compared to the carbon-nanotube based sensor, the advantages of graphene sensing are larger sensing area (with whole surfaces exposed to the chemicals), ballistic carrier transportation, and low noise at low charge carrier concentration. Schedin *et al* reported that the detection of the individual gas molecules such as NO₂, NH₃, H₂O, and CO using graphene.[57] They used pristine exfoliated graphene flakes to pattern Hall-bar shape with the contacts of the source and drain. By exposing the GFET in a gas environment, the conductance of graphene changed linearly with the gas molecule concentration. The conductance change became n-type or p-type depending on the intrinsic charges of gas molecules. The detection limitation was in the order of 1 ppb.

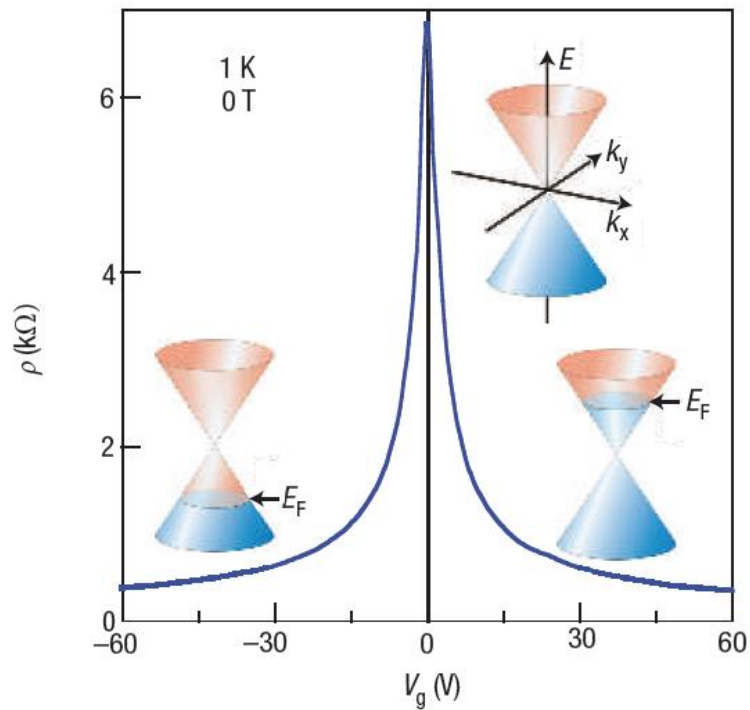


Figure 1.7 Ambipolar electric field effects in single-layer graphene.[58]

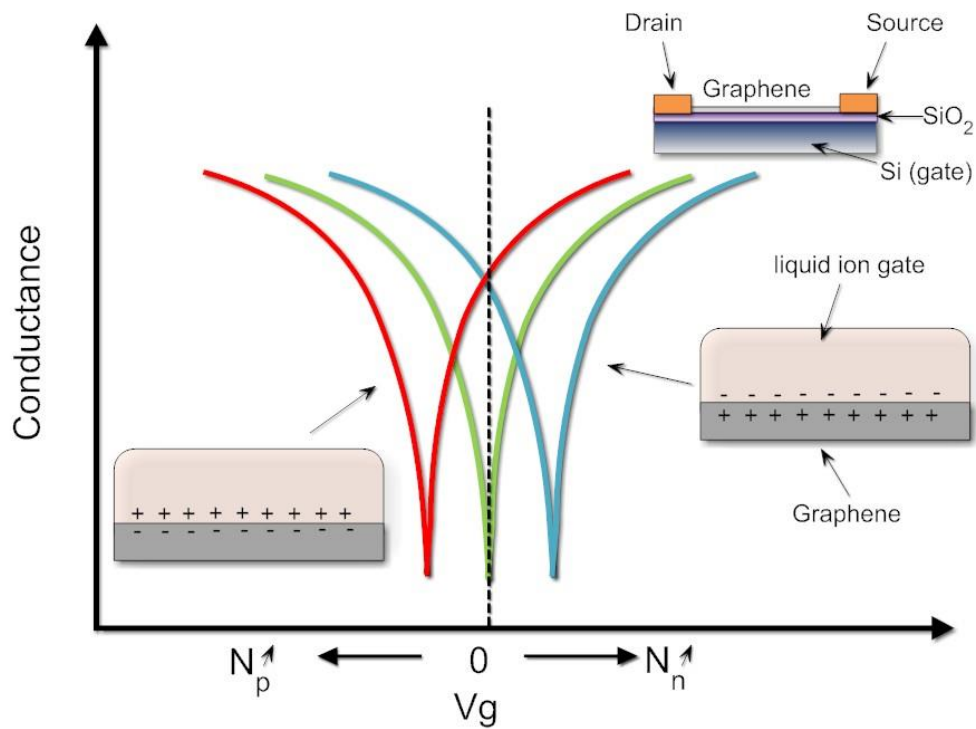


Figure 1.8 Working principle of a graphene field effect transistor sensor.

1.4.2 Transparent, flexible, and conducting electrode

Currently, the price of indium tin oxide (ITO) electrodes is incredibly high due to its scarcity in resource. New materials that can replace the ITO electrodes have attracted extensive attention in both academe and industry. Since the first graphene sheet was reported, many reports show the feasibility of graphene as a transparent electrode material that can replace ITO. In order to meet industrial requirements of transparent electrodes, it is important to improve the transparency and sheet resistance of materials. Graphene has extraordinary optical transparency in itself. Even for 5 layers graphene sheet, the optical transmission rate is still close to 90% according to its linear light absorption relation with layer. ITO electrode has an optical transmission rate of 85%~90%. Resistance per square Ω/\square is another critical parameter for the commercial application of transparent electrode, especially in displays and touch screens. For ITO, the resistor per square can be reduced to $\sim 100 \Omega/\square$ by heavily tin doping (n-type). An idea free standing intrinsic single layer graphene may have larger resistance per square $\sim 6000 \Omega/\square$ by calculation, which seems not promising compared to ITO.[29] However, the experiment results show that single layer graphene made by mechanic exfoliation may have much smaller resistance. Although the CVD graphene has issues such as defects and low carrier motilities, its resistance per square can still reach the similar value as the ITO as a result of the doping by impurities.[20] Wang *et al* has developed a graphene based solar cell by using a thermal reduction method to obtain conductive and transparent graphene films from exfoliated graphite oxide.[59] Blake *et al* demonstrated first graphene based liquid crystal devices which showed a high contrast ratio.[60] In their device, an exfoliated graphene flake was patterned as a hexagonal shape electrode

with Cr/Au contact electrode in a parallel structure. When applied a 100V voltage across the device, the white light contrast ratio is better than 100. Graphene electrode can also be applied to the next generation touch screens.[61] By using a special Roll-to-roll method, the CVD growth graphene can be transferred onto a 30-inch size polymer sheet for further resistive touch screen. The graphene electrode has many advantages compared to conventional electrode materials like ITO. First, the carbon resources used for graphene synthesis is abundant. Second, the conductance is high. And lastly, graphene is thermally and chemically stable and more transparent. [62]

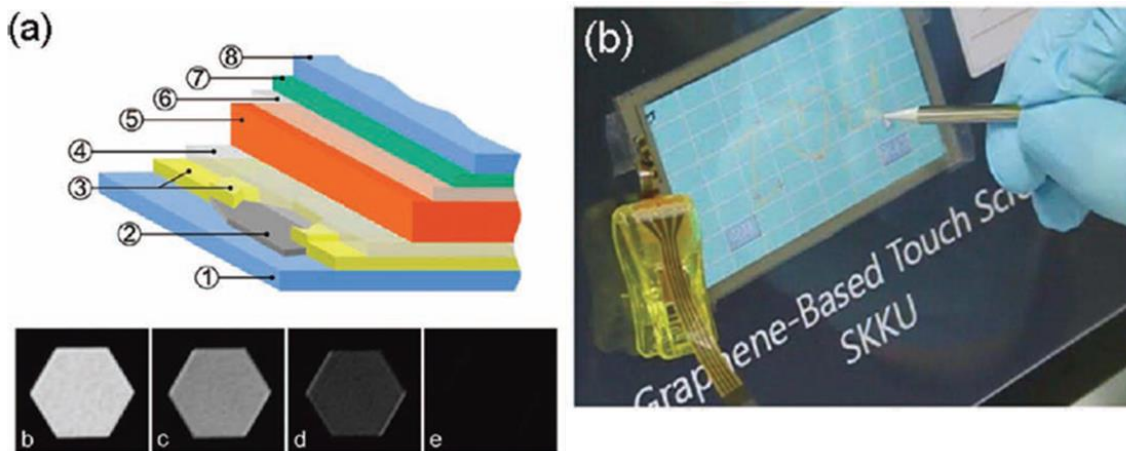


Figure 1.9 Graphene electrode based applications. (a) LCD devices, (b) Touch screen.[63]

1.5 Scope of this thesis

This chapter briefly introduces graphene's properties, fabrication methods, characterization, and applications. The thesis work mainly focused on two projects. First, Chapter 2 and Chapter 3 discuss the sensing applications with graphene field effect transistor. Chapter 2 reported a high sensitive pH sensor with integrated graphene nanoribbons. Chapter 3 proposed a graphene biosensor for detecting *E.coli* bacteria. We

studied the sensitivity variation issues and found a new way to increase the pH response of graphene FET by introducing the edge defects to the graphene. The functionalization of graphene has also been discussed to help to understand the specific binding between biomolecule and graphene.

The second part of the thesis, Chapter 4 and Chapter 5 reports the microfluidics applications of using graphene. Chapter 4 demonstrated the experiment using graphene as the transparent and flexible electrodes for electrowetting-on-dielectric (EWOD) application. Chapter 5 focused on developing a digital microfluidic system with patterned graphene ground electrodes. The dielectric layer on hydrophobic graphene surface was studied by impedance test and leakage current test. We observed a large contact angle change, and high dielectric breakdown with the graphene. Furthermore, we designed a graphene EWOD system for droplet manipulating. These experimental results show that graphene has the potential to be used as the electrode material in EWOD application.

CHAPTER 2 EDGE EFFECTS ON THE pH RESPONSE OF GRAPHENE-NANORIBBON FIELD-EFFECT TRANSISTORS

2.1 Introduction

Graphene is a single atomic layer of graphite that has extremely high carrier mobility and thermal conductivity, [64-66] and is chemically and thermally stable, [67] offering the most tantalizing prospect of high performance carbon-based electronics for the post-silicon era. As the electrons/holes in graphene are confined to an atomically thick plane, the electrical conductance of graphene is extremely sensitive to its surroundings such as substrates,[68] dielectric media[69] and adsorbed foreign molecules,[70] making graphene an ideal sensing material for label-free chemical and biological sensors. Schedin *et al.* demonstrated that micrometer-size gas sensors made from graphene were capable of detecting the adsorption and desorption of individual gas molecules.[70] Such high sensitivity was attributed to the unique combination of graphene's two-dimensional (2D) nature (extremely large surface to volume ratio), low noise level due to its relatively high conductivity and few crystal defects, and the possibility of fabricating graphene devices with ohmic electrical contacts.

Graphene has also been studied for pH,[71] chemical and biological sensor applications.[72] However, a large variation in pH response has been reported for pH sensors based on graphene field-effect-transistors (FETs), ranging from ~ 0 mV/pH to as high as 99 mV/pH.[71, 73-77] Fu *et al.* has recently shown that pristine graphene is insensitive to pH changes in solution and large variation in the pH-induced gate-voltage shift could be attributed to the variation of graphene quality.[73] Similarly, defect free carbon nanotube (CNT) FETs only respond to the electrostatic potential rather than the

pH changes.[78] The insensitivity of graphene and CNT FETs to pH changes could be attributed to the lack of free bonds on the sp^2 bond saturated pristine graphene surface. On the other hand, dangling bonds are anticipated on the surface of defective graphene. Chemical groups such as hydroxyl groups can easily attach to the defect sites of defective graphene through dangling bonds.[79][44] The attached hydroxyl groups can be protonized to OH_2^+ as the pH decreases or deprotonized to O^- as the pH increases. As a result, positively charged OH_2^+ and negatively charged O^- on the graphene surface induces n-type and p-type doping in the graphene channel, respectively. Therefore, in order to improve the sensitivity of the graphene pH sensor, it is necessary to increase the density of the hydroxyl groups attached to the graphene channel.

In contrast to the chemically inert basal plane, the edges of graphene are chemically reactive and can be relatively easily functionalized.[80] For example, graphene nanoribbons (GNR) can be functionalized by nitrogen species at the edges, leading to n-type electronic doping.[81] Moreover, edge doping was shown to be over three orders of magnitude more efficient than that induced by adsorbates on the surface.[82] Amin *et al.* have reported significant sensitivity improvement in graphene based chemical sensors by cutting the 2D graphene sheets into micro ribbons with sizes comparable to the line defects.[83] Similar to the defects in the graphene basal plane, edges are also expected to be receptive to the attachment of hydroxyl groups, which is crucial for pH sensing through the protonization and deprotonization processes. Furthermore, the edges of graphene are less disruptive to the current flow in the graphene channel compared to the defects in the basal plane which can seriously degrade the electrical properties of the graphene channel. High mobility values over $3000 \text{ cm}^2\text{V}^{-1}\text{s}^{-1}$

have been observed in low-disorder GNRs as narrow as 20 nm, suggesting that patterning graphene into GNRs (or arrays of GNRs) is a viable route to creating free bonds for hydroxyl groups to attach to without compromising the excellent electrical characteristics of the graphene sensors.[84]

In this chapter, we report a systematic study of the effects of defects and edges on the pH response of graphene pH sensors by 1) correlating Raman spectroscopy with pH-induced gate voltage shifts in the transfer characteristics of graphene FETs; and 2) patterning 2D graphene sheets into arrays of GNRs to significantly increase the density of attached hydroxyl groups. We observe a slightly increased pH response in graphene devices with a higher level of disorder as quantified by the D-band to G-band intensity ratio in the Raman spectra of the device channel made of chemical vapor deposition (CVD) grown graphene. We further demonstrate, for the first time, that the sensitivity of graphene pH sensors could be controllably increased by patterning the graphene channel into arrays of GNRs with decreasing width, without degrading the electrical properties of the graphene channel. As the width of each GNR in a channel is reduced from 40 μm to 200 nm (or below), the pH response of the devices increases from ~ 0 to ~ 25 mV/pH. This significant improvement can be attributed to the increased number of hydroxyl groups attached to the edges per unit area as the edge to surface area ratio increases with decreasing GNR width.

2.2 Fabrication process of FET devices made of graphene nanoribbons

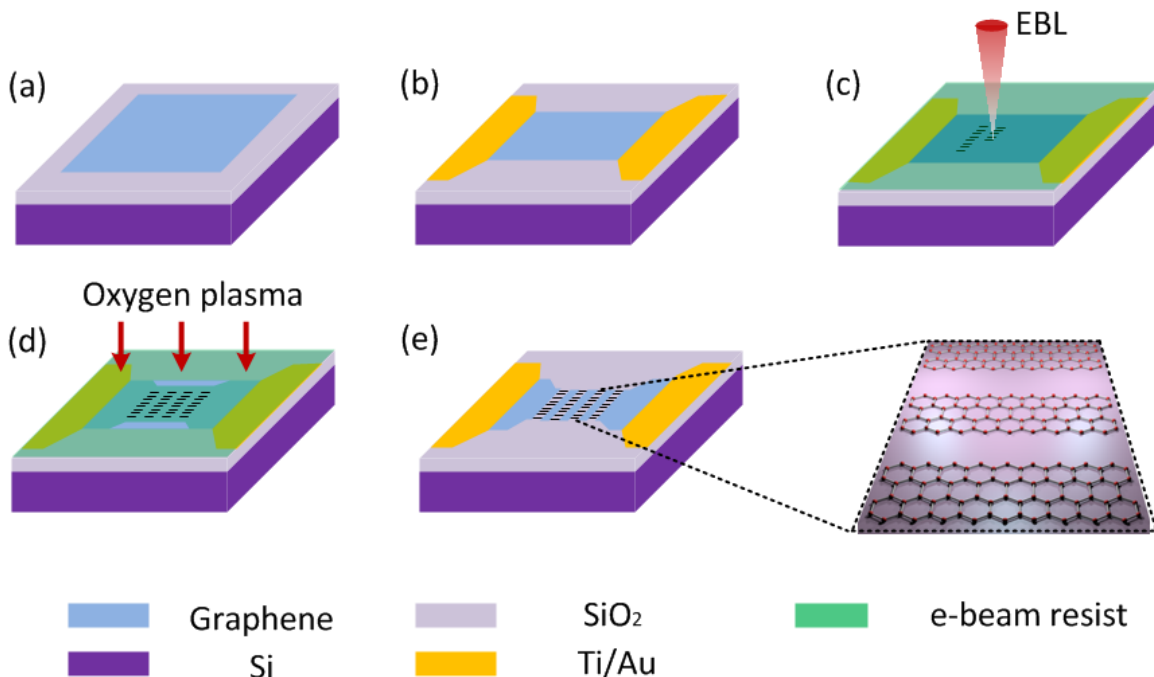


Figure 2.1 Fabrication process of FET devices made of graphene nanoribbons. (a) transfer of CVD graphene onto SiO₂/Si substrates; (b) graphene patterning and contact metal deposition; (c) graphene nanoribbon patterning with EBL by using PMMA as the e-beam resist; (d) graphene etching by oxygen plasma; (e) GNR array FET after removing the PMMA.

Figure 2.1 shows the process flow for the fabrication of graphene FETs. The pristine graphene used in this study was grown on copper using a chemical vapor deposition (CVD) method.[85, 86] Subsequently, graphene was transferred onto a silicon substrate with 300 nm thermal oxide following a method described in the literature.[86] Briefly, the CVD graphene was grown on a 25 μm thick copper foil (Alfa Aesar) in a mixture of methane and hydrogen at 1000 $^{\circ}\text{C}$. A layer of 200 nm thick Poly(methyl methacrylate) (PMMA) was spin-coated and dried at room temperature. After removing the graphene on the backside of the copper using oxygen plasma, the copper foil was etched away using diluted copper etchant (APS-100) for 24 hours. The PMMA/graphene

film was cleaned using a modified RCA cleaning procedure.[86] PMMA/Graphene films were transferred onto the silicon substrate by carefully scooping it out from the solution. Finally, PMMA was dissolved by acetone and left only graphene on top of the substrate as figure 2.1(a) showed. Graphene channels were defined by a standard photolithography and oxygen plasma etching. Next, the source/drain electrodes were fabricated by depositing 10 nm Ti and 50 nm Au by an electron-beam evaporation system (Temescal BJD 1800) as figure 2.1 (b) showed. In order to controllably create edge defects, GNR arrays of different widths were further fabricated using electron-beam lithography (EBL) as shown in Figure 2.1(c). For EBL, a positive e-beam resist (PMMA) was spin-coated, selectively exposed by e-beam and developed. Subsequently, oxygen plasma was used to remove the excess graphene to form nanoribbons [figure 2.1(d)]. Finally, PMMA was removed by acetone [figure 2.1(e)]. HSQ resist was also used to pattern GNRs. After development and oxygen plasma etching to form GNRs, HSQ was removed by buffered oxide etch (BOE) to minimize the doping effects.[82, 87] Before testing, the device was annealed at 600 °C with flow of forming gas (H_2/Ar) to remove the resist residue.[88]

To characterize the pH response of the graphene FET devices, a droplet of pH solution was deposited on the device to cover the graphene channel. The transfer characteristics of the device were measured by a silver/ silver chloride ($Ag/AgCl$) reference gate electrode. A semiconductor parameter analyzer (Keithley 4200) was used to measure the drain-source current as a function of the gate voltage by applying a constant low drain-source voltage of 10 mV. The leak current through the gate electrode was also monitored to ensure that it was negligibly small compared to the drain-source current. All the pH solutions ($6 \leq pH \leq 8$) were prepared using phosphate buffered saline

(PBS) as a buffer solution with a phosphate concentration of 2~3 mM. The devices were rinsed with an ample amount of de-ionized water to thoroughly wash away the adsorbates each time before changing to a different pH solution.

2.3 Results and discussion

2.3.1 I-V characteristic before edge patterning with different pH

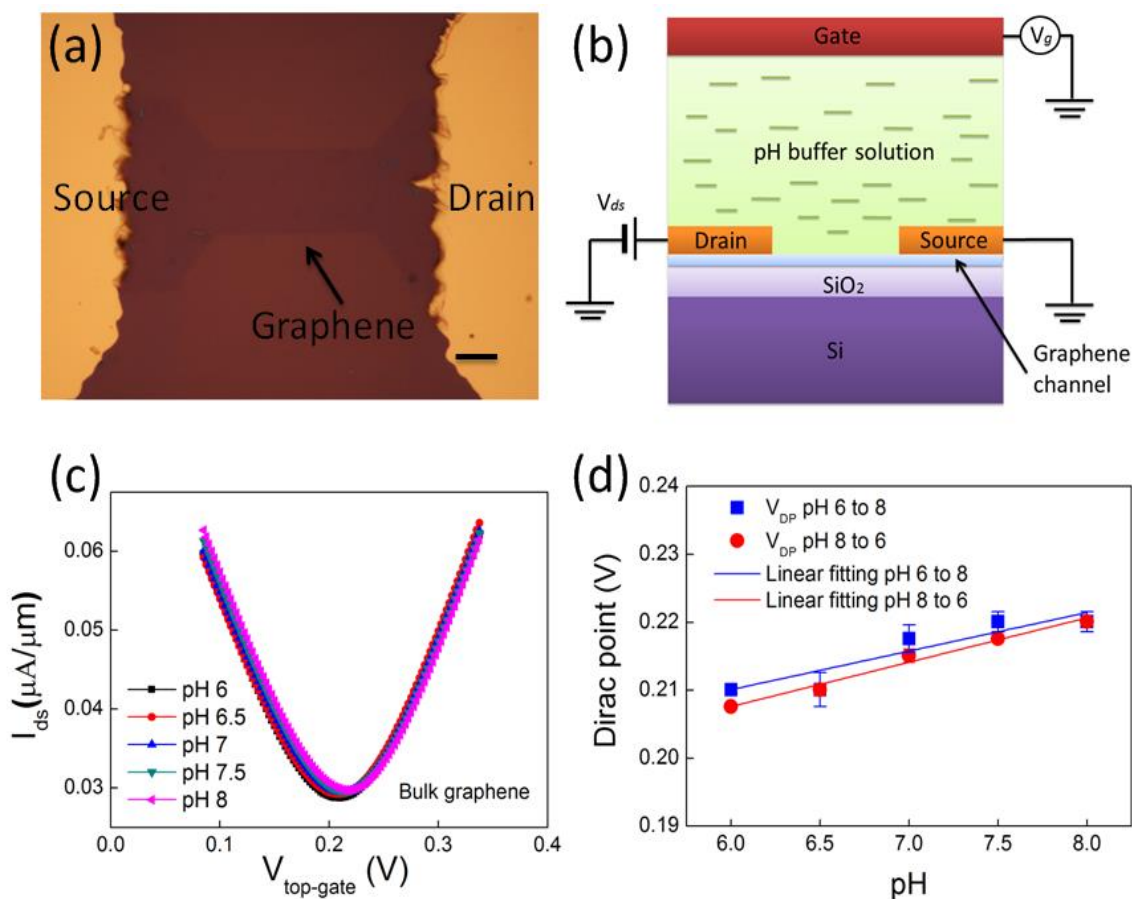


Figure 2.2 (a) An optical image of graphene FET before edge patterning. The scale bar is 20 μm ; (b) schematic illustration of the working principle of electrolyte-gated graphene FET pH sensor; (c) Measured source-drain current density I_{ds} as a function of the top gate reference potential $V_{top-gate}$ in different pH buffer solution for non-patterned pristine graphene FET. (d) the Dirac point shift in response to the different pH. The error bars show the standard deviation of the pH sensitivity.

Figure 2.2(a) shows an optical microscopic image of a representative FET device made of pristine graphene. The graphene was patterned into a dumbbell shape with a dimension of 80 μm by 50 μm . The edge length to surface area ratio in the graphene channel, $S = \frac{L}{A}$, was estimated to be around 0.04 μm^{-1} , where L is the total length of the graphene edge and A is the total area of the graphene channel. Figure 2.2(b) schematically illustrates the experiment setup for the pH sensing measurement using the graphene FET in electrolytes with a leakage free solid-state reference electrode (eDAQ ET-072). The electrical double layer at the graphene/electrolyte interface functions as a top gate dielectric of FET. The thickness of the double layer is a function of ionic concentration and temperature. The Dirac point is determined by the applied gate voltage where the electrical conductivity or source-drain current (I_{ds}) is minimum. As the gate voltage is swept from the left side to right side of the Dirac point, the doping in the graphene changes from p-type to n-type. When the pH in the electrolyte is increased, the I_{ds} vs V_g curve and the Dirac point shift toward the positive voltage direction with the increased amount of net p-doping. By measuring the shift of the Dirac point, the change of pH in the electrolyte can be monitored. The sensitivity is defined as the drift of Dirac point voltage (mV) divided by pH change.

Figure 2.2(c) shows a typical transfer curve of source-drain current I_{ds} as a function of the applied electrolyte gate voltage measured at a constant drain-source voltage (V_{ds}) of 10 mV, where the drain-source current was normalized to the width of the graphene channel. The V shaped I_{ds} - V_g curves indicate nearly symmetrical ambipolar behavior. To minimize the hysteric effect, we took several measurements at each pH to make sure that the random drift of the I_{ds} - V_g curves between different measurements at

the same pH was negligibly small. The Dirac point of the device in Figure 2.2(c) is around 0.22 V at pH 7, suggesting that the graphene channel is p-doped.[81] When the gate voltage is swept between 0.07 V to 0.32 V, the minimum and maximum current densities are determined to be 0.03 $\mu\text{A}/\mu\text{m}$ and 0.062 $\mu\text{A}/\mu\text{m}$ from pH 6 to 8, respectively. The mobility (μ) of the device is derived from the I_{ds} - V_g curve using the equation $m = (1/C_g)(dS/dV_g)$, [71] where C_g is the quantum capacitance of the graphene ($\sim 20 \text{ nFcm}^{-2}$), [89, 90] σ is the conductance, and V_g is the gate voltage. The calculated hole and electron mobility are almost the same ($1.25 \times 10^3 \text{ cm}^2\text{V}^{-1}\text{s}^{-1}$). When the electrolyte pH increases from 6 to 8, the Dirac point shifts slightly from 0.21 V to 0.223 V, yielding a low pH response of $\sim 6 \text{ mV/pH}$. This finding is in good agreement with the pH response values reported by other groups, which indicate that pristine graphene is not sensitive to pH changes.[71, 75, 76] The weak pH response of our graphene FETs along with their reasonably high mobility demonstrates that our CVD graphene is of high quality.[73] For practical pH sensing applications, the measurement results should not be affected by any historic ions or charge effects. Thus, we measured the Dirac point shift with both increasing pH from 6 to 8 and decreasing pH from 8 to 6. Figure 2.2 (d) shows that the pH response is 6 mV/pH as the pH increases from 6 to 8 and 6.5 mV/pH as the pH decreases from 8 to 6, indicating that the pH response of our graphene FETs is reversible. The reversibility of the graphene FET devices is consistent with the protonization and deprotonization of OH^- groups attached to graphene.

2.3.2 pH response to the intrinsic defects related to Raman

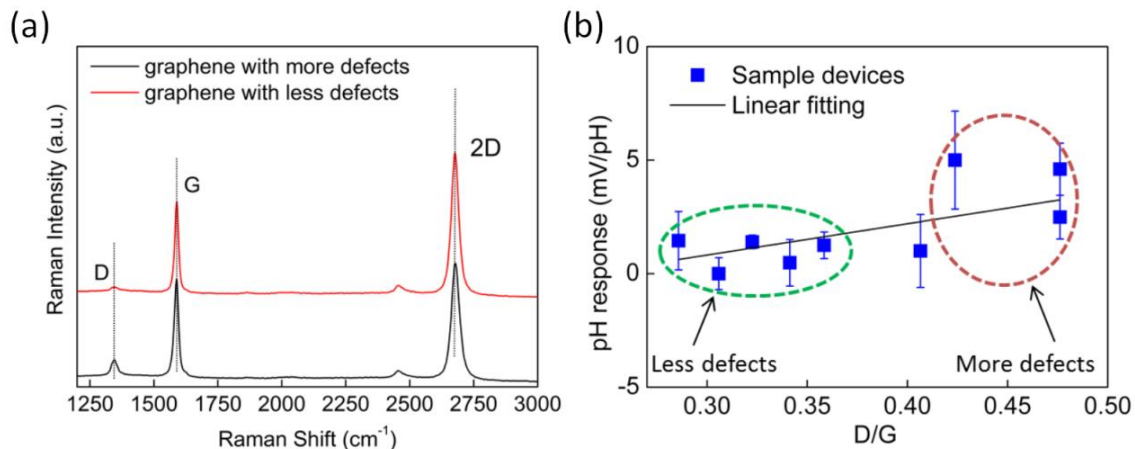


Figure 2.3 (a) Raman spectrum of the graphene samples with different intrinsic defects; (b) pH sensitivity in response to the Raman peak intensities of G (1588 cm^{-1}) /D (1344 cm^{-1}). The error bars show the standard deviation of the pH sensitivity.

Since our graphene was grown by CVD, it is likely to contain a small amount of defects in the basal plane. To understand the impact of the defects on pH response, we performed a combined study of pH response and Raman spectroscopy on a number of graphene FETs.[91] Figure 2.3(a) shows the Raman spectra of two representative graphene FETs. The peak at 1344 cm^{-1} (D band) is associated with the lattice disorder of graphene while the peak at 1580 cm^{-1} (G band) corresponds to the vibration of sp^2 bond carbon atoms. The ratio of the D band to G band intensities can be used to quantify the level of defects or disorder in the graphene, where a high D/G ratio corresponds to a higher level of defects or disorder. Figure 2.3(b) summarizes the pH response of several graphene FET versus the D/G intensity ratio. The pH response increases with the D/G ratio (or defect level in the graphene). The higher pH response in more defective devices can be attributed to the increased number of active dangling bonds on the defect sites that allow adsorption of H_3O^+ or OH^- groups. The sensitivity enhancement can also be

affected by the Poole-Frenkel conduction regime where the electrons could hop through the defects.[92]

2.3.3 I-V characteristic after edge patterning with different pH

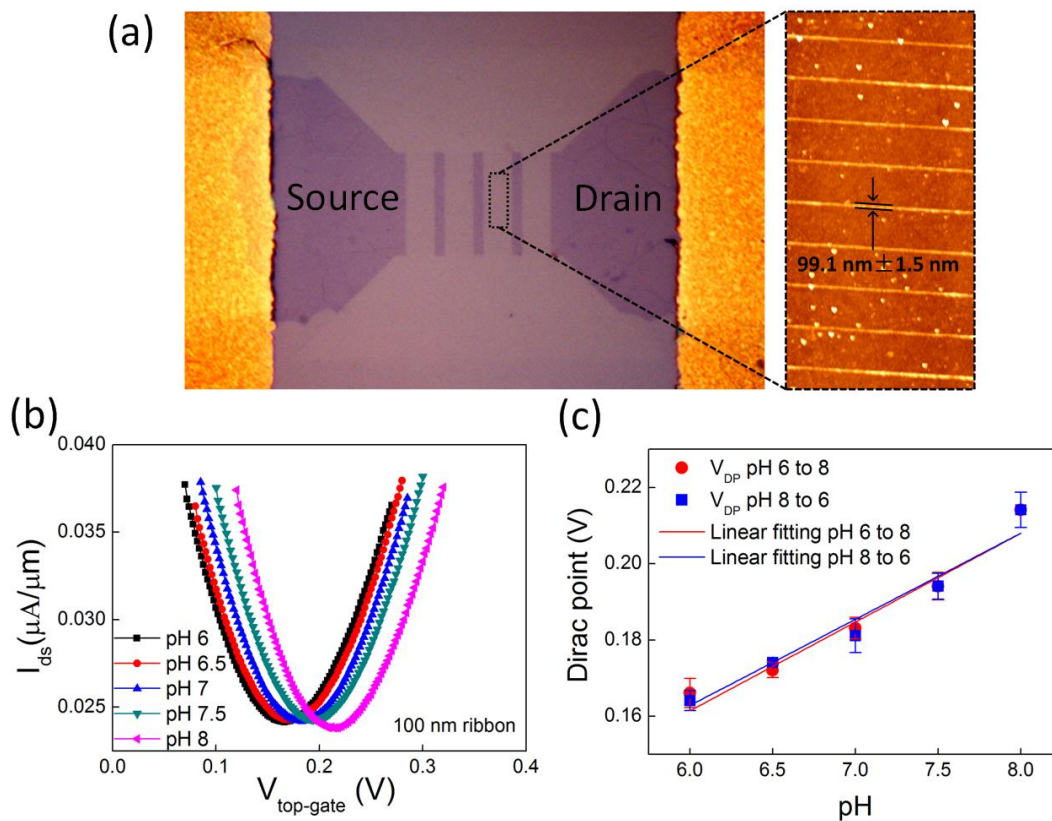


Figure 2.4 (a) An image of graphene FET after EBL edge patterning; AFM images to show graphene nanoribbons (b) The drain-source current density I_{ds} as a function of the top gate reference potential $V_{\text{top-gate}}$ in different pH buffer solutions for FET made of 100 nm width graphene nanoribbons. (c) The Dirac point shift in response to the different pH. The error bars shows the standard deviation of the pH sensitivity.

Encouraged by this interesting finding, we developed a novel approach to improve the pH response of graphene FETs by engineering edge defects. Figure 2.4(a) shows the microscopic image of a graphene FET consisting of GNR arrays patterned by EBL and oxygen plasma. The graphene channel consisted of four columns of ribbons connected by large graphene islands, where each GNR was determined to be $99.1 \text{ nm} \pm$

1.5 nm wide, 5.5 μm long, and mostly 1~2 layer by atomic force microscope (AFM). Before testing, the device was annealed at 600 $^{\circ}\text{C}$ with flow of forming gas (H_2/Ar) to remove the resist residue.[88] Figure 2.4(b) shows the transfer curve ($I_{ds}-V_g$) of a FET device consisting of 100 nm wide GNR arrays. Although the total channel width was reduced from 50 μm to 2 μm after patterning, the current density I_{ds} remains nearly the same. The mobility of GNRs FET also remains essentially the same ($1.02 \times 10^3 \text{ cm}^2\text{V}^{-1}\text{s}^{-1}$) compared to the pristine graphene FETs, suggesting that introducing edge defects would not degrade the electronic property of the graphene FETs. On the other hand, we observed a significant improvement of pH response increasing from $\sim 6.5 \text{ mV/pH}$ to $\sim 23.6 \text{ mV/pH}$ by patterning the graphene channel into arrays of narrow GNRs ($\sim 100 \text{ nm}$ wide). The strong enhancement of the pH response can be largely attributed to the increase of dangling bonds associated with the increase of total edge length per unit area after patterning the graphene channel into GNRs. Similar effects were observed in gas detection in atmosphere environment using graphene nanoribbons.[83] We also noticed that there was a small systematic shift of the Dirac point toward the negative voltages (0.16V) in the GNR FET compared to the pristine graphene FET device before patterning (0.21V). This could be attributed to the remaining resist residue from the fabrication process.[93] To further verify that the enhancement of the pH response in GNR FETs is primarily caused by the creation of more edges rather than by impurities such as resist residue, HSQ resist was also used to pattern GNRs. After development and oxygen plasma etching to form GNRs, HSQ was removed by buffered oxide etch (BOE) to minimize the doping effects.[82, 87] Similar pH response values were observed in GNR FETs patterned using HSQ as with PMMA. Figure 2.4(c) shows the Dirac point position

versus pH for the GNR FET device as the pH changes from pH 6 to 8 and then from pH 8 to 6. The pH response of the patterned GNR device is determined to be 23.6 mV/pH and 24 mV/pH, respectively. This result demonstrates that the pH response of GNRs is significantly higher than that of large area graphene and the pH response in GNR FETs is also reversible as in large area graphene FETs.

2.3.4 Statistic results of pH response with different ribbon edge to surface ratio

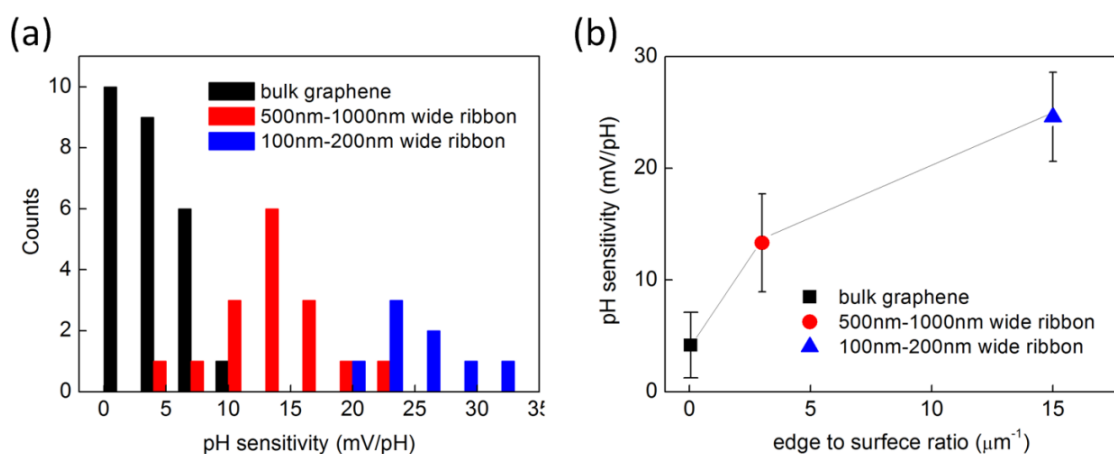


Figure 2.5 (a) A histogram of sensitivity for the FETs with pristine graphene and graphene ribbons of various widths, Sensitivity of different devices (mV/pH); (b) average pH sensitivity with different edge to surface area ratio. The error bars show the standard deviations.

Figure 2.5 summarizes the results from over 40 devices divided into three categories: pristine graphene, wide GNRs of width 500 nm ~ 1000 nm, and narrow GNR of width 100 nm ~ 200 nm. Figure 2.5(a) shows the histogram of the pH response of the devices clearly revealing that the pH response increases with reducing GNR width. The lowest (~0 mV/pH) and highest (30.6 mV/pH) sensitivity values were found in a pristine graphene FET and a 100 nm wide GNR device, respectively. The highest pH response of the pristine graphene FET was about 9.6 mV/pH, and the lowest pH response of 100 nm graphene ribbon was above 20 mV/pH. The average pH response for pristine graphene,

500 nm ~ 1000 nm ribbons, and the 100 nm~200 nm ribbon pattern was determined to be 4.2 mV/pH, 13.5 mV/pH, and 24.6mV/pH as shown in figure 2.5(b). Obviously, increasing edge defect sites by reducing the GNR width efficiently improves the pH response.

The sensitivity and sensing mechanisms of graphene-based FET are still under debate. Ohno[76] reported a sensitivity of 50mV/pH in an electrolyte-gated graphene field-effect transistors (GFET) made of mechanically exfoliated graphene. Cheng[75] reported a sensitivity of 25mV/pH of a suspended graphene sensor with improved signal to noise ratio by removing underneath SiO₂ with HF. Nevertheless, Fu showed that the large variation of the pH response may be associated with the quality of the graphene samples in terms of how they were prepared.[73] Here, we have shown that engineering edge defects significantly improves the pH response of graphene FETs in aqueous solutions. Controllable line edge defects can be created by patterning pristine graphene into graphene nanoribbons using EBL and oxygen plasma. The nanofabrication process does not noticeably degrade the electronic and electrochemical properties of the graphene FETs. The number of edge defect sites for pH sensing can be increased by reducing the width of GNRs, leading to the enhancement of pH response.

2.4 Summary

In this chapter, we demonstrated that higher pH response of graphene FETs can be achieved by introducing edge defects. The edge defects were created by patterning the graphene into GNR arrays using electron beam lithography and oxygen plasma. We have observed pH response increasing from 4.2 mV/pH to 24.6 mV/pH when the edge length

to surface area ratio increases from $0.04 \mu\text{m}^{-1}$ to $20 \mu\text{m}^{-1}$. We also demonstrated that the pH sensing is reversible for both pristine and patterned graphene FET.

CHAPTER 3 GRAPHENE BASED BIOSENSOR FOR BACTERIA DETECTION

3.1 Introduction

Human pathogenic bacteria, such as *E. coli*, *Salmonella*, *Listeria*, and *Staphylococcus*, are often shed by warm-blooded animals and survive well in the environment. They can contaminate urban surface water through human and animal fecal waste and storm water runoff, combined with sanitary sewer overflows and wastewater treatment plant effluents. These pathogens have been commonly found in surface water and can cause serious outcomes. The traditional microbiological methods such as PCR, ELISA and DNA hybridization either are labor-intensive or require bulky and expensive instrument. Biosensors have great advantages over the traditional methods, including ease of operation, short turnaround time, high accuracy, and wide detection capacity. Berry's group first reported the graphene based biosensor for achieving single bacteria detection.[94] However, their results were based on electrostatic adhesion of the bacteria due to the non-specific attaching, which was not practical for real sensing application. Moreover, their approach lacks the capability of detecting different bacteria species. A recent breakthrough shows that the interaction between biomaterials and graphene can be employed as a nanosensor platform for monitoring the bacteria growth on tooth enamel.[95] Bioselective detection of bacteria at single-cell levels was achieved by using the self-assembly antimicrobial peptides on graphene. Particularly, Chen *et al.* has demonstrated that graphene based biosensors can detect *E.coli* bacteria. [96] In their experiment, (1-pyrenebutanoic acid succinimidyl ester) bio-linker molecule was used to functionalize with CVD graphene and anti-*E.coli* O& K antibody was used for specific

binding with *E.coli* bacteria. The results showed that high sensitivity can be achieved by electrically detection with a limit of detection (LOD) of 10 cfu/mL.

In this chapter, we demonstrated the highly selective detection of *E.coli* bacteria based on phage tail spike proteins (TSPs) functionalized graphene biosensor. TSPs are the phage proteins that attach to the specific binding sites on the surface of bacteria and determine the specificity of the bacterial host. Each TSP has two terminal domains, the C-terminal domain binding to the cellular LPS receptor and the N-terminal domain that can be immobilized to the substrate through EDC/NHS method.[97] Attaching only the TSPs to the substrates will allow a greater concentration of the proteins that interact directly with bacteria. The anchoring of TSPs to the substrates allows the correct orientation of TSPs on the substrate. This also means exposing the C-terminal domain of the TSPs to bind directly to the bacterial surface, and therefore, increase the binding efficiency of ligand-receptor as well as the smoothness of surface to facilitate characterization. The immobilization of *P22* TSPs on silicon substrate has been studied and being used for selective bacterial detection.[98] However, the graphene based bacteria sensor through TSPs binding has not been reported yet. The electrical conductance measurement and optical microscope results showed that *E.coli* bacteria can be attached to the *E.coli* TSPs through specific binding.

3.2 Methods

3.2.1 Preparation of CVD

We used chemical vapor deposition (CVD) method to grow the pristine graphene. Typically, a 25 μm thick copper foil (Alfa Aesar) was loaded into a vacuum furnace and annealed at 1000 $^{\circ}\text{C}$ with 3sccm Hydrogen gas first. The graphene deposition was carried

out by adding a mixture gas of methane and hydrogen. The flow rate ratio is 1:10 to 1:11.5 ($H_2:CH_4$). When the temperature is above 700 °C, methane will thermal decompose into carbon and hydrogen on top of the copper surface. Due to the low solubility of carbon atoms in copper, a thin layer of graphene will form eventually.

3.2.2 Device Fabrication

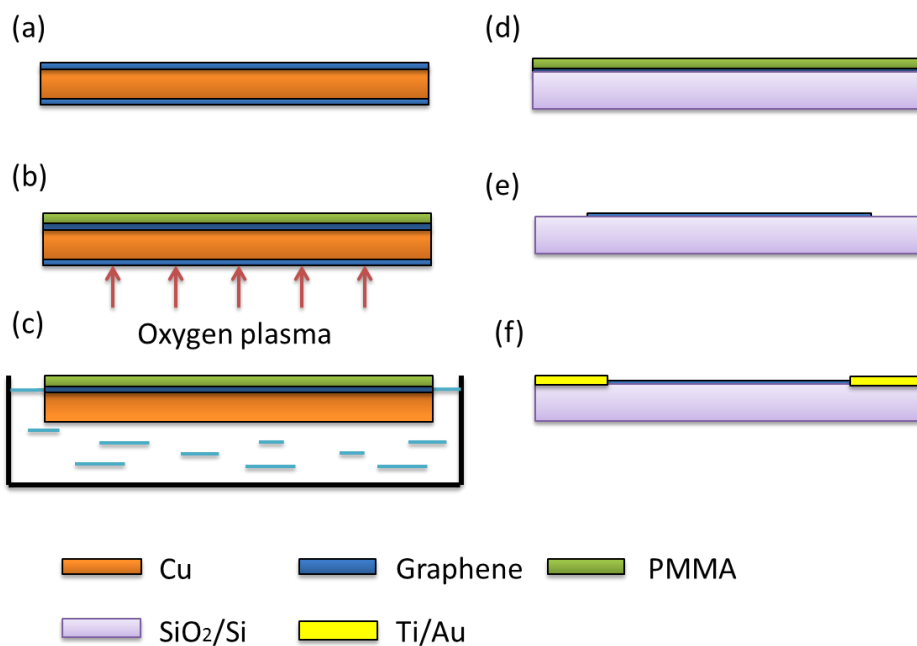


Figure 3.1 Process flow of device fabrication. (a) CVD graphene growth on copper foil, (b) oxygen plasma etching to remove the backside graphene with a pin-coated PMMA on the top side, (c) wet etching to remove the copper, (d) transfer PMMA/graphene to silicon substrate with thermal oxide, (e) remove PMMA, (f) graphene patterning and contact electrode deposition with e-beam evaporation.

Figure 3.1 shows the device fabrication process, which was similar to the strategy that we have been used for making the pH sensor device. [99] Briefly, the graphene was transferred onto a silicon substrate with 300 nm thermal oxide by using the chemical wet etching method. During the process, a 200 nm thick Poly(methyl methacrylate) (PMMA) was spin-coated on the top side of the graphene. We then etched the backside graphene

using 100 W oxygen plasma (30 sccm, 30 s). The copper foil was fully etched by using diluted copper etchant (APS-100). To remove the metal and other polymer contamination on the graphene, a modified RCA clean was used here to clean the graphene before transferred to the substrate. After rinse with deionized (DI) water the cleaned PMMA/graphene sheets were scooped out of the solution and gently attached to the substrates. We waited for 30 min to let the PMMA/graphene sheets dry in room temperature, and then removed the PMMA by using acetone. The patterning of graphene was done by photolithography and oxygen plasma etching; the graphene channel was designed as rectangular shape with a size about $80\ \mu\text{m} \times 50\ \mu\text{m}$. Finally, a layer of Ti/Au (5 nm /50 nm) was deposited as the contact electrodes as drain and source. The device can be tuned with both back gate (silicon) and top gate (reference electrode).

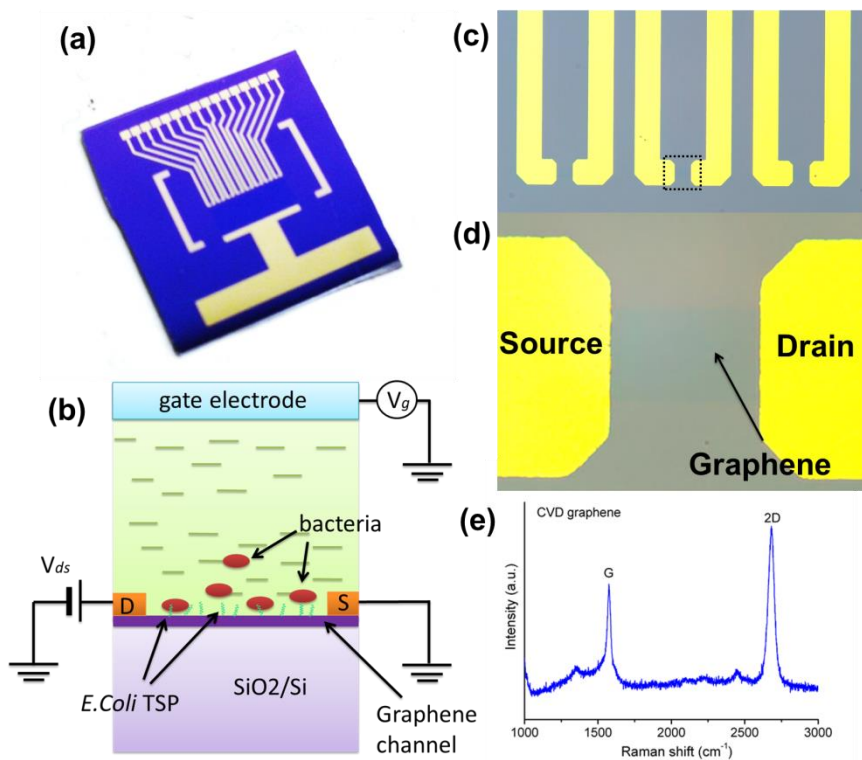


Figure 3.2 Graphene bacteria sensor device structure and testing setup. (a) Optical image of the whole graphene FET device for bacteria sensor, (b) test setup for sensor device, (c)

(d) zoom-in microscope images of the device structure, (e) Raman spectrum of the CVD graphene.

Figure 3.2(a) shows the macroscopic image of the graphene biosensor device. There are eight transistors in parallel and the detail structure is shown in figure 3.2 (c) and 3.2(d). Each graphene channel is measured 80 μm by 50 μm . Raman spectroscopy measurement reveals that most of the area is single layer graphene as shown in figure 3.2 (e). The sensing of the bacteria was conducted by measuring the change of the electrical conductance (I-V curve shift) after each binding step. Here we used the experience of pH sensing with graphene FET pH in Chapter 2 for setup the bacteria sensing platform. Figure 3.2 (d) shows the configuration of the sensing measurement with bacteria in solution. Briefly, the charge carrier on the cell wall of the bacteria will affect the local dipole and surface potential of the graphene.[100] Similarly to the pH sensing, when the negatively charged bacteria is attached to the graphene surface, a larger Dirac point will be expected due to the increased amount of hole doping to the graphene channel. On the other hand, if the bacteria are positively charged, the Dirac point will shift to the left, which indicates the contributing of electrons to the graphene. In our experiment, an Ag/AgCl reference electrode was used to avoid the potential change due to the electrochemical reaction. We measured the I-V curve between the drain and source of the graphene channel by sweeping the top gate voltage after we changed each sample.

3.2.3 Zeta Potential measurement

Zeta potential measurement was performed by using phase analysis light scattering with a Zetasizer Nano ZEN3600. *The E.Coli* bacteria and *E.Coli* TSP were diluted with tap water and the zeta potential was measured in Malvern capillary plastic

cells (DTS 1061). The scattering detection angle is 173 and the zeta potential value was calculated from the Smoluchowski equation using Malvern software.

3.2.4 Immobilization of *E. Coli* TSPs on graphene surface

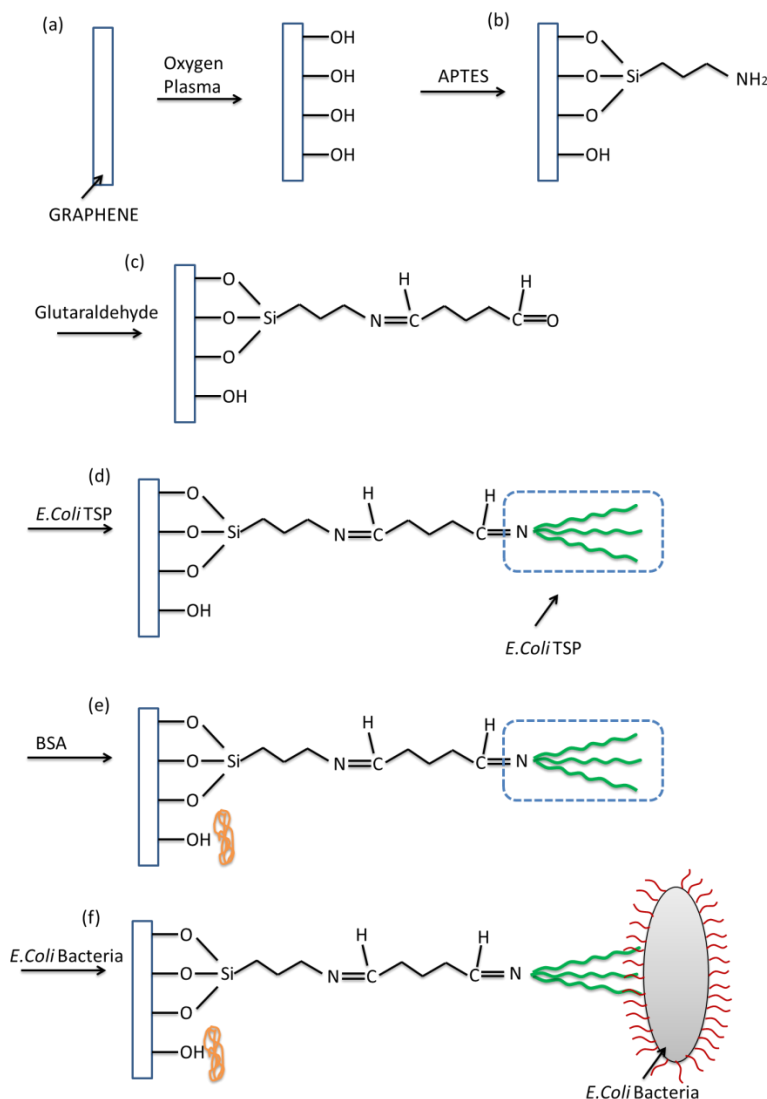


Figure 3.3 Chemical reaction mechanism of graphene surface functionalization (a) oxygen plasma to introduce the surface oxygen and hydroxyl group, (b) ATPES reaction to introduce the amine group, (c) glutaraldehyde (GA) to introduce the carboxyl group, (d) *E. coli* TSPs immobilization with the carboxyl groups, (e) 1% BSA was applied after step d for blocking the unconjugated sites, (f) *E. coli* bacteria specific binding with *E. coli* TSPs.

The protocol of graphene functionalization was adopted from the method used for TSPs binding on silicon. We used the modified method for the graphene surface functionalization with *E.coli* TSPs. We first treat the graphene with 1~2s oxygen plasma to introduce more oxygen and hydroxyl groups at the defect sites. Then, the graphene was immersed in a 2% solution of APTES in ethanol (95%) with pH 5. After 15 min, we rinsed the graphene with ethanol and DI water and blew dry with nitrogen gas. The device was baked at 100 °C for 5 min to cure the silane monolayer. After that, the device was rinsed again with ethanol and DI water. To active the amine group of the APTES, the graphene device was incubated in 2% glutaraldehyde for 30 min at room temperature. During this step, the amine group will form C=N group with the carboxyl group of the Glutaraldehyde. Also the other terminal of the glutaraldehyde can be used for the bioconjugation with TSP through its N-terminal. Here we used 180 µg/ml~400µg/ml *E.coli* TSPs to functionalize the graphene through bioconjugation. After the TSPs immobilization, 1% BSA was used to block the nonspecific binding.

3.2.5 Device Testing

To measure the binding of the bacteria with the graphene biosensor, a droplet of fresh *E.coli* bacteria with a concentration of $1 \times 10^9 \sim 1 \times 10^{10}$ cfu/ml was deposited to cover the graphene sensing channel to let the bacteria bind to the TSPs. After half an hour, we washed off the non-binding bacteria by rinsing the device with Tap water. The electrical conductance of the device in response to the bacteria binding was measured by an Ag/AgCl reference gate electrode. We used a semiconductor characterization system (Keithley 4200) to measure the I-V curve through the drain and source. All the curves were measured in tap water liquid environment.

3.3 Results and discussion

3.3.1 Zeta Potential

We characterized the electric properties of the *E.coli* bacteria by using the zeta potential, which is the electrical potential between the aqueous solution and the stationary layer of the surrounding liquid attached to the bacteria. Zeta potential of each material (BSA, TSP and bacteria) were measured in tap water at 25 °C. We have diluted original sample into 10 times and 100 times within tap water. It was found that the *E.coli* bacteria shows a Zeta potential around 0.328 mV to 0.517 mV in Tap water, which indicated that the surface charge of the bacteria in the tap water environment is positive. However, other research [101],[102],[103] show that zeta potential of the bacteria are mostly negative. This is because of the zeta potential is associated with the pH and also the ion concentration of the media.

Sample Name	Zeta Potential (mV)	Mobility (cm ² /Vs)	Conductivity (mS/cm)
<i>E.coli</i> bacteria	0.328 ~ 0.517	0.0257~ 0.0406	1.67~ 0.401
BSA	-13.1~ -15.8	-1.03 ~ -1.24	0.324~1.02
<i>E.coli</i> phage	-12.2~ -17.3	-0.954~ -1.354	0.396~1.69
<i>E.coli</i> TSP	-2.88 ~ -15.8	-0.226 ~ -1.236	0.158 ~6.71

Table 3.1 Zeta potential of *E.coli* bacteria, *E.coli* phage, BSA, and *E.coli* TSP in tap water.

3.3.2 Electrical testing

We studied the specific detection of the *E.coli* bacteria with *E.coli* TSPs. We first applied 1% Bovine serum albumin (BSA) to quench the unreacted *E.coli* TSPs immobilized on the graphene. After that, a different type of bacteria, *salmonella* bacteria, which will not form specific binding with the *E.coli* TSPs was cultured with the graphene

sample. Figure 3.4 (a) showed the transfer characteristics of the graphene biosensors after each binding steps. The initial Dirac point (the gate voltage that has the minimum drain current value) after immobilized with *E.coli* TSP was only 0.038 V, indicated a low level of defects of the graphene. The Dirac point had almost no shift after the BSA blocking. This denoted that the BSA blocking had very limited effects on TSPs immobilized graphene surface and would cause very small change to the electrical property of graphene in our case. However, other researches show that the BSA functionalized graphene can cause the resistance increase due to the adsorbed non-conductive molecules inhibited the graphene contact and prevented the electron transfer across the graphene film.[104] Here, the reason of small change of the Dirac point and conductance (resistance) may be due to the high level of uniform *E.coli* TSPs films that formed on the graphene surface and the Stericycle effect which will prohibit the attachment of the BSA to the unreactive binding site. The 5×10^{10} cfu/mL *salmonella* bacteria did not cause a significant shift of the Dirac point. This is attributed to the fact that the *salmonella* bacteria are not able to bind with the *E.coli* TSPs functionalized on the graphene. In addition, the non-specific binding of the *salmonella* bacteria was prevented by the BSA blocking. In figure 3.4 (b), the microscope image of the graphene biosensor after *salmonella* bacteria binding showed that there is no specific binding of the *salmonella* bacteria to the *E.coli* TSPs.

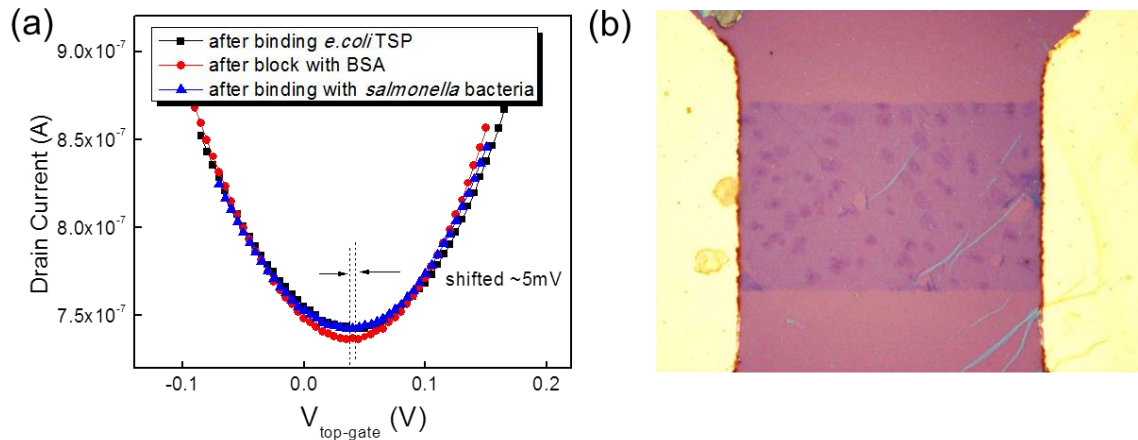


Figure 3.4 (a) I-V curve after *salmonella* bacteria, show no binding of bacteria, (b) optical microscope image of the device after *salmonella* bacteria binding.

In sharp contrast, the *E.coli* bacteria binding led to a significant shift of the Dirac point (20 mV) of the graphene FET. The left shift is in agreed with the zeta potential measurement of the *E.coli* bacteria we obtained. The positively charged bacteria increased the electron density in graphene. The mobility of the graphene FET can be derived by $m = (1/C_g)(dS/dV_g)$ [71], where C_g is the quantum capacitance of the graphene ($\sim 20 \text{ nFcm}^{-2}$), [90, 105] σ is the conductance, and V_g is the gate voltage. The calculated hole and electron mobility are almost the same ($1.1 \times 10^3 \sim 1.2 \times 10^3 \text{ cm}^2\text{V}^{-1}\text{s}^{-1}$). The numbers of the *E.coli* bacteria binding to the graphene was counted as 33 ± 2 in an area of $80 \mu\text{m}$ by $50 \mu\text{m}$.

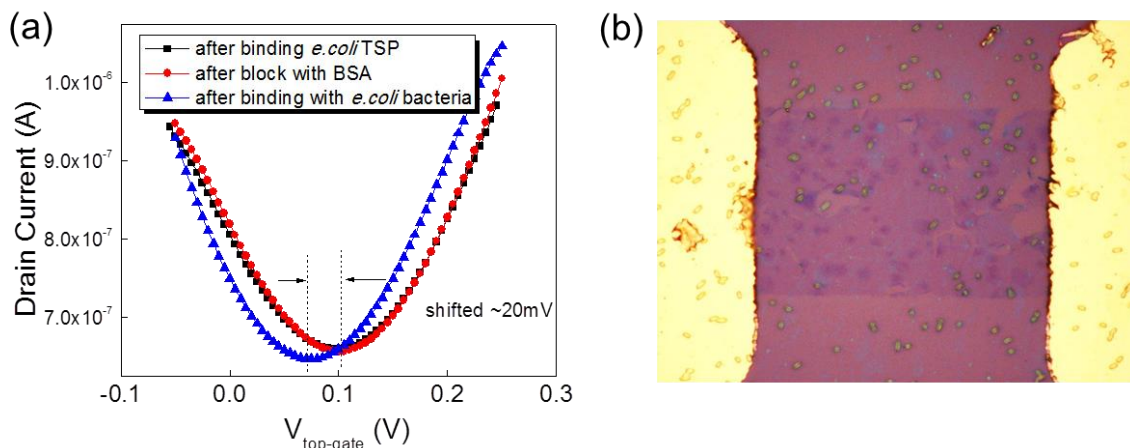


Figure 3.5 (a) I-V curve after *E.coli* bacteria, show Dirac point shifted around 20 mV to the left; (b) optical microscope image of the device after *E.coli* bacteria binding showed there are about 33 ± 2 bacteria counts.

A comprehensive specific binding experiment with different type of bacteria towards the *E.coli* TSPs was conducted. Potentially, after binding with *E.coli* bacteria, the graphene FET was unable to bind any other type of bacteria because of the specific bind. Here the transfer characteristics in figure 3.6(a) showed that after *E.coli* bacteria binding, there was no obvious shift of the Dirac point towards the left.

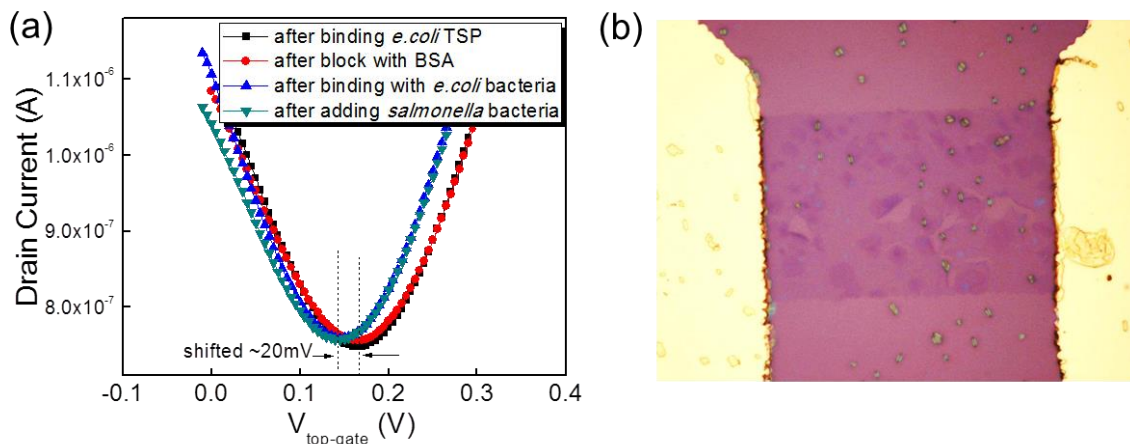


Figure 3.6 (a) I-V curve after *E.coli* and *salmonella* bacteria binding, showed no obvious shift after *salmonella* bacteria binding; (b) optical microscope image of the device after *salmonella* bacteria binding showed there are about 27 ± 2 bacteria counts.

3.3.3 Sensitivity

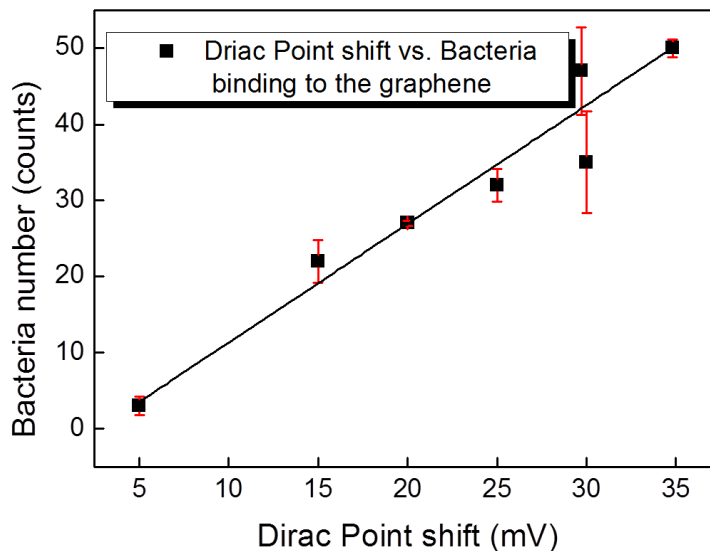


Figure 3.7 Dirac point shift in response to the bacteria numbers bind to the graphene FET. 7 devices were counted for obtaining the statistic information. Linear fitting showed that the sensitivity was 1.24 mV/*E.coli* bacteria.

We summarized the sensitivity of the graphene bacteria sensors related to the numbers of the *E.coli* bacteria that specifically bound to the *E.coli* TSPs. The observed results showed that with a higher population (~50) of bacteria bound to the graphene, the shift of the Dirac point could be as high as 35 mV, which gave sensitivity at 1.24 mV/bacteria.

3.4 Summary

In this chapter, a label-free graphene bacteria sensor was developed to detect the specific binding to *E.coli* bacteria. CVD graphene was patterned as transducer sensing arrays by utilizing the photolithography and oxygen plasma etching. We developed a method to functionalize the graphene surface with *E.coli* TSPs, which can directly bind to

the *E. coli* bacteria with high selectivity. The electrical conductivity properties for each functionalization step and bacteria binding were studied by the graphene FET system using a reference electrode as the top gate electrode. The linear sensitivity (1.24 mV/bacteria) was derived by analyzing the Dirac Point shift in response to the numbers of the bacteria binding to the graphene from 7 devices.

CHAPTER 4 ELECTROWETTING ON DIELECTRIC (EWOD) USING GRAPHENE ELECTRODE

4.1 Introduction of electrowetting

Electrowetting on dielectric (EWOD) is the control of contact angles (wetting) of droplets by applying an electrical voltage between the droplet and the counter electrode coated with a hydrophobic dielectric layer.[106] The contact angle in response to the voltage change is described by the Lippmann-Young equation $\cos \theta = \cos \theta_0 + \frac{CV^2}{2\gamma}$ (1), where θ is the contact angle of the liquid droplet with the applied voltage, θ_0 is the initial contact angle, γ is the surface tension of the liquid-vapor interface, C is the capacitance of the dielectric layer per area, and V is the applied voltage.[107] In EWOD, the capacitance per unit area is determined by $\frac{\epsilon_0 \epsilon}{t}$, where ϵ and t are the relative dielectric constant and thickness of dielectric materials, respectively, and ϵ_0 is the permittivity of free space. Because of the presence of an insulating dielectric layer, a large voltage can be applied between the conductive droplet and the electrode without electrolysis. The advantages of EWOD include (1) reversible and robust control of contact angles, (2) more applicable liquids that can be manipulated because of the hydrophobic surface coating of dielectric layers (typically fluoropolymer). Therefore, EWOD has been applied in various applications, including digital microfluidics, [47, 108-113] optics,[114-117] display,[118-121] and analysis of biological samples.[122-124]

Most of the current EWOD devices are based on planar substrates. The electrode materials commonly used in EWOD include metals (gold, platinum, copper, etc), semiconductors (silicon, carbon nanotube),[125] and ceramics (ITO). Table 4.1 summarizes the properties of selected materials. ITO (310nm thick) has a 85% optical transparency in the visible light range.[126] However, it is brittle and lacks flexibility. Gold offers more flexibility, but is rather expensive and optically opaque. None of these electrode materials can achieve both high optical transparency and mechanical flexibility. On the other hand, graphene is a novel nanomaterial with excellent material properties such as high conductivity, optical transparency, and mechanical flexibility. Graphene thin film can achieve better optical transmission (>90%) than ITO with a similar resistance $R_s=20\Omega/\square$. [29] It is also promising to fabricate low cost graphene electrode by chemical vapor deposition (CVD).[127-129] However, to the best of our knowledge, there has been no report on the application of graphene in EWOD.

In this chapter, superior EWOD performances can be achieved by depositing graphene on flexible transparent plastic substrates. The graphene-based EWOD devices were measured by applying both AC and DC driving voltages. The electrochemical properties of Teflon coated graphene were characterized using electrochemical impedance spectroscopy (EIS). Compared to gold electrode, Teflon layer on graphene electrode exhibits less electrolysis and less leakage current under the same applied voltages.

	Gold	ITO	Graphene
Optical transmission (%)	<20 (180nm)[130]	85 (310nm)[125]	97.7 (<1nm)[131]
Youngs' modulus (GPa)	80[132]	116[133]	500[19]
Yield strength (MPa)	55~200[134]	1200[135]	1.3×10^5 [18]
Electrical conductivity (S/cm)	4.52×10^5 [136]	1×10^4 [137]	9.6×10^5 [3]

Table 4.1 Properties of different electrode materials. The optical transmission uses 550nm wavelength as reference.

4.2 Materials and methods

The graphene sheets used in this study were grown using a CVD method [138]. CH₄ gas was used as the carbon source, and was thermally decomposed on copper at high temperature. A clean copper foil (Alfa Aesar) was first annealed for 2 hours while flowing a H₂ gas at a rate of 3 sccm and a pressure around 40 mTorr at 1000 °C. To grow graphene, a mixture of 30 sccm CH₄ and 2 sccm H₂ gases was flown into the chamber for 30 minutes at 1000 °C. The pressure was controlled around 500 mTorr. After growth, graphene sheets were transferred onto different substrates following the procedures reported by Colombo *et al.*[138] Briefly, a thin layer of PMMA 495 (MicroChem, Newton MA) was spin-coated (3000 rpm) on the graphene side of the copper foil and dried at room temperature for 1 hour. Subsequently, the copper foil was etched in a 1 M ferric chloride (FeCl₃) with the PMMA side facing up. The floating PMMA/graphene sheets were then carefully scooped out of FeCl₃ solution using a piece of silicon substrate and rinsed in DI water. To obtain a smooth graphene surface, the silicon substrate was kept close to the floating PMMA/graphene sheet until the whole sheet naturally attached to the substrates before it was removed from the beaker. The graphene/PMMA sheet was

dried overnight at room temperature. The PMMA layer was then removed by acetone, and the graphene sheet was rinsed several times in isopropyl alcohol (IPA). In this experiment, the transparent and flexible polyester film (PET) was used to demonstrate EWOD on a transparent, curved and three-dimensional substrate. Considering that the glass transient temperature of PET films was less than 200 °C, high temperature annealing was not applied for the device fabrication. However, it has been often used in literature to remove the PMMA residue on graphene with other substrates.[139]

For external electrical contact, 5 nm Cr/ 50 nm Au was deposited using electron beam evaporation through a shadow mask made of stainless steel. A Teflon dielectric layer (DuPont AF 1600 1%~6% diluted in 3M FC 72) was spin coated on top of graphene at 3000 rpm and baked at 165 °C for 2 hours. The thickness of Teflon was measured by both an ellipsometry and a surface profiler (Dektak, Bruker). The Raman spectroscopy of the CVD graphene deposited on various of substrates was measured by a Raman system consisting of a Jobin–Yvon Horiba Triax 550 spectrometer, a liquid-nitrogen cooled charge-coupled device (CCD) detector, Olympus model BX41 microscope with a 100×objective, and a 514.5 nm Modu-Laser (Stellar-Pro-L) Argon-ion laser. The Raman-scattered light from the sample was collected by the same microscope objective and was focused on the entrance slit of the spectrometer with a 1200 line/mm diffraction grating. The data was recorded and analyzed using the LabSpec software.

The contact angle measurement was performed on a home-built optical system consisting of a Navitar 12X zoom lens, a white light semi-flexible fiber optical source and a USB CCD camera (iSolution). The samples were placed on a three-axis stage while a Labview module was used to control a function generator (Agilent 33120A) and an AC

power amplifier. The CCD camera was also programmed using the Labview software to record movies with a maximum frame rate of 60 fps. The system is capable of generating AC voltages from 0 V~140 V with a frequency between 10 Hz and 10 KHz. For EWOD, KCl solution (10 mM, 100 mM) was used.

The AC impedance measurement was carried out using a PARSTAT 2273 advanced electrochemical system (Princeton Applied Research). A schematic illustration of the device structure is shown in figure 4.1, where a thin graphene sheet was deposited on top of a PET substrate and was coated with a thin Teflon layer. The working electrode of the potentiostat was connected to the tungsten probe (W1000-1605R, Rucker & Kolls) inserted in a droplet deposited on the dielectric surface, while the counter and reference electrodes were connected to the graphene electrode. The amplitude of the AC voltage was 0.1 mV. The frequency was swept from 0.1 Hz to 100 kHz. All the measurements were performed under ambient atmosphere conditions at room temperature inside a Faraday cage (in order to minimize electromagnetic noises). Nyquist plots were recorded with the x and y axes as the real part and imaginary part of the device impedance, respectively.[130] The leakage currents were measured by a digital multimeter (Agilent 34401A). Additional 1 μm Parylene C dielectric layer was deposited by a Parylene deposition system (Labcoater 2 SCS PDS2010, Specialty Coating Systems, Indianapolis, IN, USA).

4.3 Results and discussion

4.3.1 Graphene flexible EWOD device structure

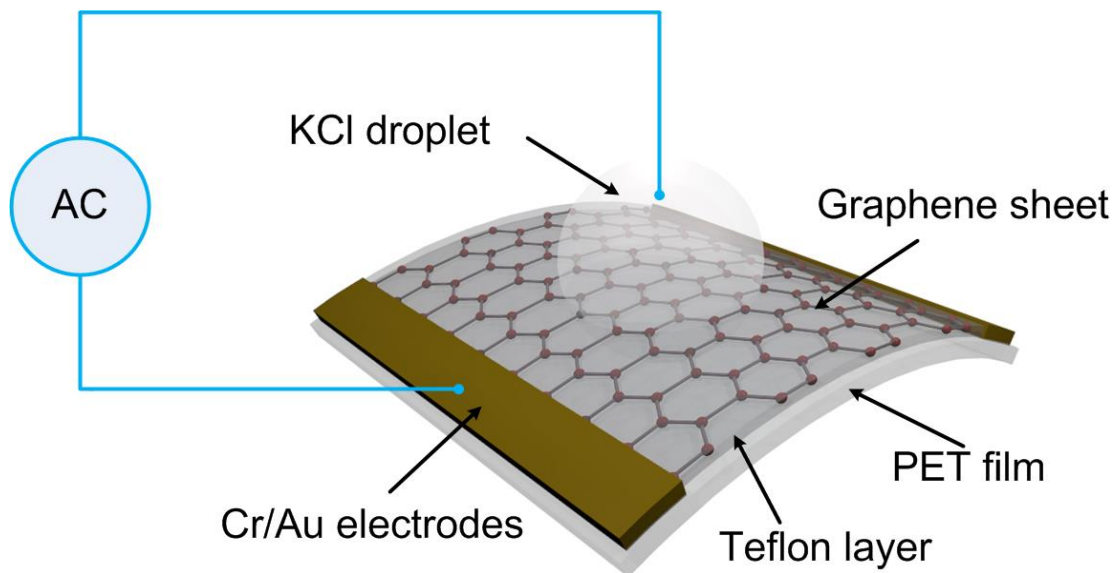


Figure 4.1 A schematic view of EWOD on a flexible and optically transparent graphene electrode.

Figure 4.2a and 4.2b show pictures of two types of graphene based EWOD devices. Figure 4.2a shows a graphene sheet after being transferred onto a PET film with Cr/Au contact pads. Figure 4.2b shows a graphene EWOD device on a glass slide for droplet manipulations. The graphene was defined using photolithography and oxygen plasma. The low optical contrast of graphene on the transparent glass is attributed to the lack of interference between glass and graphene as well as the high transmission rate of graphene. Figure 4.2c shows a Raman spectra of the graphene in figure 4.2a, where a relative intensity ratio of $\frac{I_G}{I_{2D}} \approx 0.4$ between G band ($\sim 1590 \text{ cm}^{-1}$) and 2D band ($\sim 2670 \text{ cm}^{-1}$) along with the shape of the 2D peak indicates that our graphene sample was a single layer.[140] The absence of D band ($\sim 1350 \text{ cm}^{-1}$) indicates low disorder and high quality of our graphene.[141] The average thickness of a 6% Teflon spin-coated (3000

rpm) device was measured to be $1.2 \mu\text{m} \pm 0.2 \mu\text{m}$, using ellipsometry. The surface profile of spin-coated Teflon by Dektak shows a 15%~20% thickness variations within the scanning range of 3 mm.

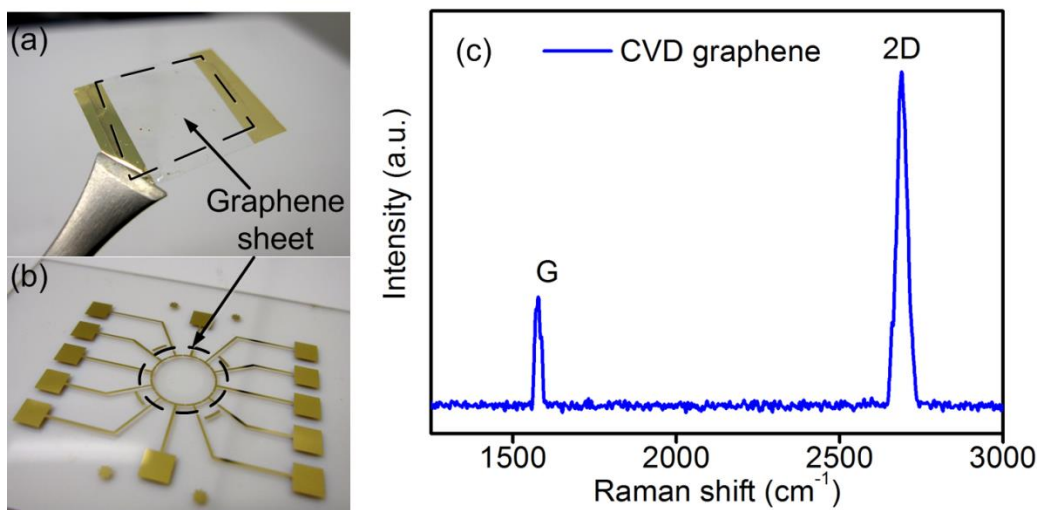


Figure 4.2 (a) and (b) Two types of EWOD devices with graphene electrodes and Cr/Au contact pads; (c) Raman Spectra of CVD graphene.

4.3.2 EWOD performance

Figure 4.3 shows the response of aqueous electrolyte droplets (KCl, 3 μL , 10 mM) to AC voltages (1 kHz) from 0 V to 100 V. The voltage was applied between the Teflon coated graphene electrode and the droplet. By using a droplet analysis tool of the ImageJ software, the initial contact angle of the KCl droplet placed on a 1 μm Teflon dielectric layer (6% in FC72) was determined to be $109.5 \pm 1^\circ$ at 0 V. This value was very similar to the literature.[108] The contact angle of the droplet decreased to $70.2 \pm 1^\circ$ as the voltage increased to 90 V without any electrolysis as shown in Figure 4.3a. The voltage dependence on the contact angle can be well described by the equation (1) as shown in Figure 4.3b (the solid line is the theoretical fit). The unit capacitance extracted from the fit (6.08×10^{-11} F) is in good agreement with that calculated using the double-

plate capacitance model (5.8×10^{-11} F, assuming $\gamma = 72.7$ dyn/cm,[142] $\varepsilon = 2.1$, and the thickness of the Teflon layer $t = 0.96$ μm). The variation of contact angles was probably due to the rough surfaces of Teflon coatings. As the voltage increased beyond 90 V, no further decrease of the contact angle was observed. This can be attributed to the instability of the applied electrical field where the high density of charge carrier is injected into the insulator, a phenomenon known as contact angle saturation.[107, 143, 144] In the experiment, the dielectric Teflon layer was still stable on graphene even at 140 V and the initial value of the contact angle of the droplet at 0 V was instantaneously restored when the applied voltage was turned off, suggesting high durability and reversibility of the Teflon on the graphene structure. Contact angle changes with DC voltage were also observed here. It is found that the contact angle change range varies depending on the thickness of the Teflon dielectric layer.

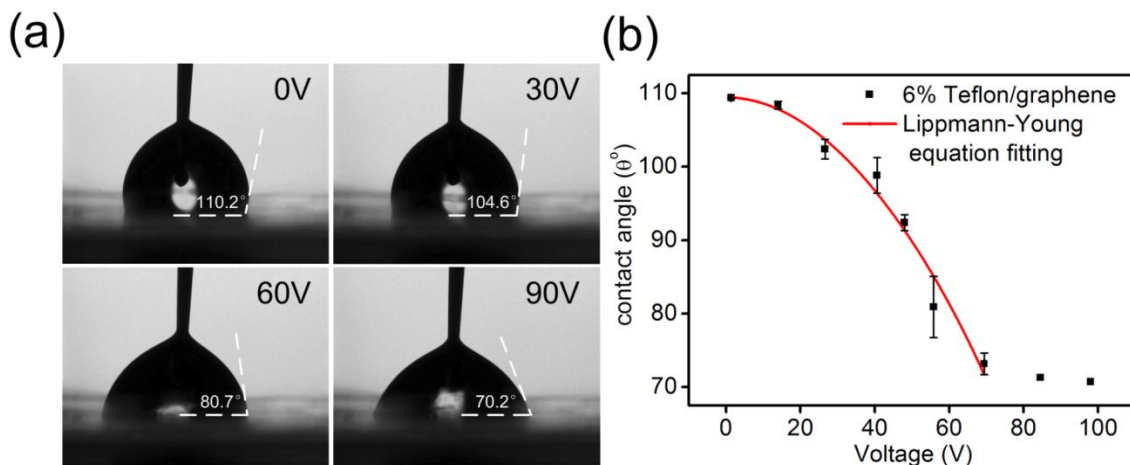


Figure 4.3 (a) Captured images of contact angle changes of a KCl droplet on a graphene electrode coated with 1 μm Teflon (6% in FC72); (b) Contact angle changes of a KCl droplet (10 mM) as a function of applied AC voltage (0 V~100 V, 1 kHz) on a 1 μm Teflon (6% in FC72) coated graphene. The solid line is the fitting result by using Lippmann-Young equation. The fitting parameters are: $\theta_0 = 109.45^\circ$, surface tension $\gamma = 72.7$ dyn/cm, relative dielectric constant for Teflon layer $\varepsilon = 2.1$, the thickness of the Teflon layer $t = 0.96 \mu\text{m}$ and $\varepsilon_0 = 8.85 \times 10^{-12}$ F/m.

The reversibility of electrowetting on graphene was tested with two different Teflon (1% and 3%) thicknesses using a Labview controlled power amplifier. Figure 4.4 shows the cyclability of the contact angles of a droplet on the thicker Teflon layer (3% in FC 72; 550 nm~750 nm) coated on graphene when an AC voltage (1 kHz) was switched between 15.3 and 46.9 V. The result shows that the contact angles changed reversibly between 112° and 92° for more than 50 cycles. On the thinner Teflon layer (1% in FC 72, less than 100 nm), the AC voltage (1 kHz) applied to a 3 μL KCl droplet was switched between 15 V and 36 V every second. The result shows the reversible electrowetting with the contact angles switched between 115° (at 15 V) and 95° (at 36 V). We speculate that the excellent cyclability of the reversible electrowetting demonstrated by Teflon coated graphene electrodes could be attributed to the higher chemical and mechanical stability of graphene compared to other commonly used electrode materials. It was also found that the reversible electrowetting was reproducible using both AC and DC voltages.

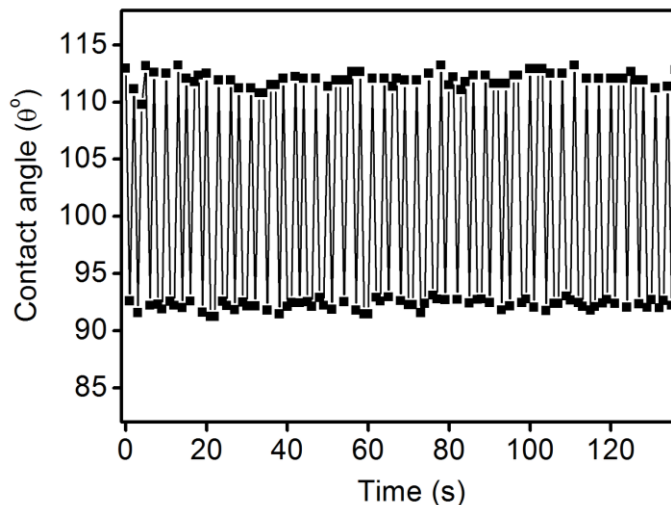


Figure 4.4 Reversibility tests of contact angles of a droplet (10 mM KCl) in air with AC voltage switched between 15.3 V and 46.9 V. This result shows a reversible contact angle changes for 50 cycles with a 550nm~750nm thick Teflon layer.

4.3.3 Electrochemistry modeling of graphene EWOD system

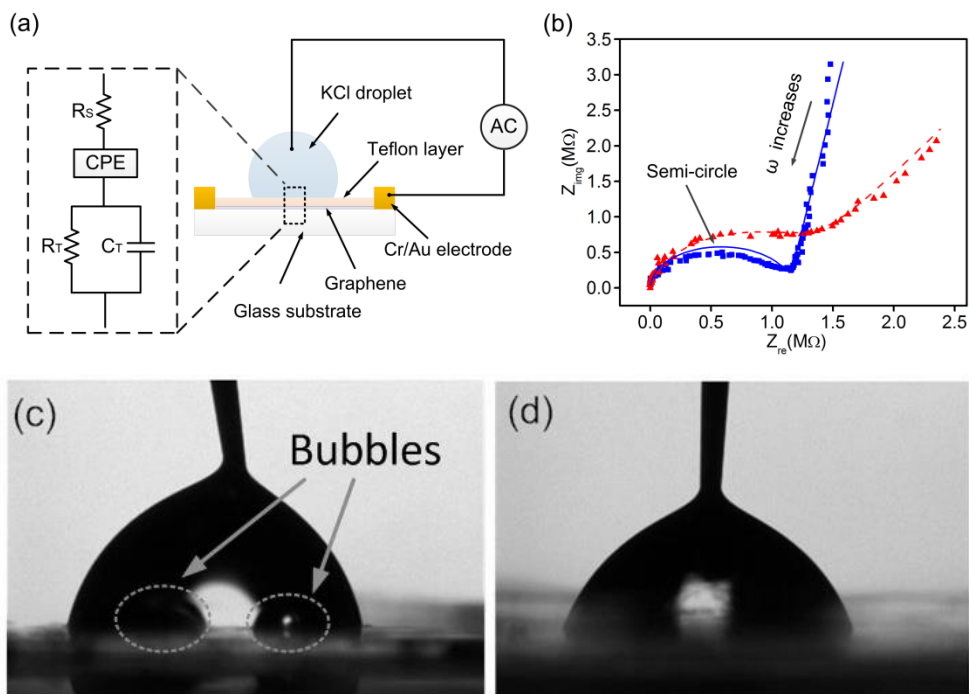


Figure 4.5 (a) An equivalent circuit model of EWOD electrode and the Teflon dielectric layer (b) Impedance measurements and simulations on Teflon coated graphene with 100 mM KCl solution. (blue square) 6% Teflon with graphene electrode; (red triangles) 6% Teflon with gold electrode; (c) 6% Teflon coated on gold electrode at 80V; (d) 6% Teflon on graphene electrode at 80V. There were bubbles from the Teflon coated gold electrodes (c) compared to no bubbles in Teflon coated graphene electrodes (d).

To further study the Teflon dielectric properties with different electrodes, we tested the AC impedance of graphene and gold electrodes using the same Teflon coating condition (6% in FC72). Electrochemical impedance measurement is a common technique to understand an electrochemical system. Critical parameters can be extracted by this method, including the capacitance and leaking resistance of Teflon, the double layer capacitor between electrolytes and solid, and electrolyte resistance. A simplified circuit model for the device is shown in figure 4.5a, where R_s is the electrolyte resistance, R_T and C_T are the resistance and the capacitance of the Teflon layer, and CPE is the constant phase element associated with the double layer of the electrolyte/Teflon

interface. Based on the Nyquist plots from Figure 4.5b, the circuit could be cataloged by two different regions depending on the frequency of the AC voltages. At high frequency (100 kHz to 100 Hz), CPE is negligible, and R_S in series with $R_T // C_T$ dominate the impedance. The depressed semi-circles (Z_{img} 0~1 M Ω and Z_{re} 0-1.2 M Ω) next to the origin of the plot represent high frequency responses. By fitting impedance data to this model, as shown in table 4.2, we found that R_S is approximately 2000 Ω and R_T is about $1.08 \times 10^6 \Omega$ to $1.15 \times 10^6 \Omega$. The capacitances of the Teflon layer C_T on graphene and gold electrodes are 3.8×10^{-11} F and 4.58×10^{-11} F respectively. These values are consistent with the theoretical capacitance $C = \frac{\epsilon_0 \epsilon A}{t}$ assuming a Teflon thickness of $1 \mu\text{m} \pm 0.2 \mu\text{m}$ and droplet size of 3 μL (from 5.8×10^{-11} F to 4.14×10^{-11} F). At low frequencies ($f < 100$ Hz), the circuit is dominated by the double layer capacitor of solid/electrolytes. The double layer capacitor is not an ideal capacitor because of presence of pin-holes and rough surfaces of electrodes. The circuit response is represented by a straight line connected to the depressed semi-circle. The straight line is modeled by a constant phase element (CPE). A CPE comprises a distribution of ohmic and capacitive elements which lead to non-uniform, frequency-dependent resistance and capacitance.[145] By fitting the impedance data, we estimated the slope $\alpha_{Teflon/graphene}=0.91$ and $\alpha_{Teflon/gold}=0.66$. The slope α gave the nature of the impedance properties. For capacitive impedance, α is close to 1, for resistive impedance, α is close to 0. The double layer capacitor of Teflon/gold is more electrically leaky compared to that of Teflon/graphene. For the same voltage range (0 V to 100 V), the contact angle changes on the Teflon coated graphene electrode ($\sim 40^\circ$) were found to be larger than that on Teflon coated gold electrode ($\sim 30^\circ$) under otherwise identical conditions, suggesting that the Teflon on graphene is slightly

thinner than the Teflon on gold. The higher capacitive impedance for the Teflon/graphene electrode system in comparison with the Teflon/gold electrode system can be mainly attributed to the lower density of pores and defects in the Teflon on graphene electrode than in the Teflon on gold electrode.[146]

4.3.4 Leakage current and dielectric breakdown

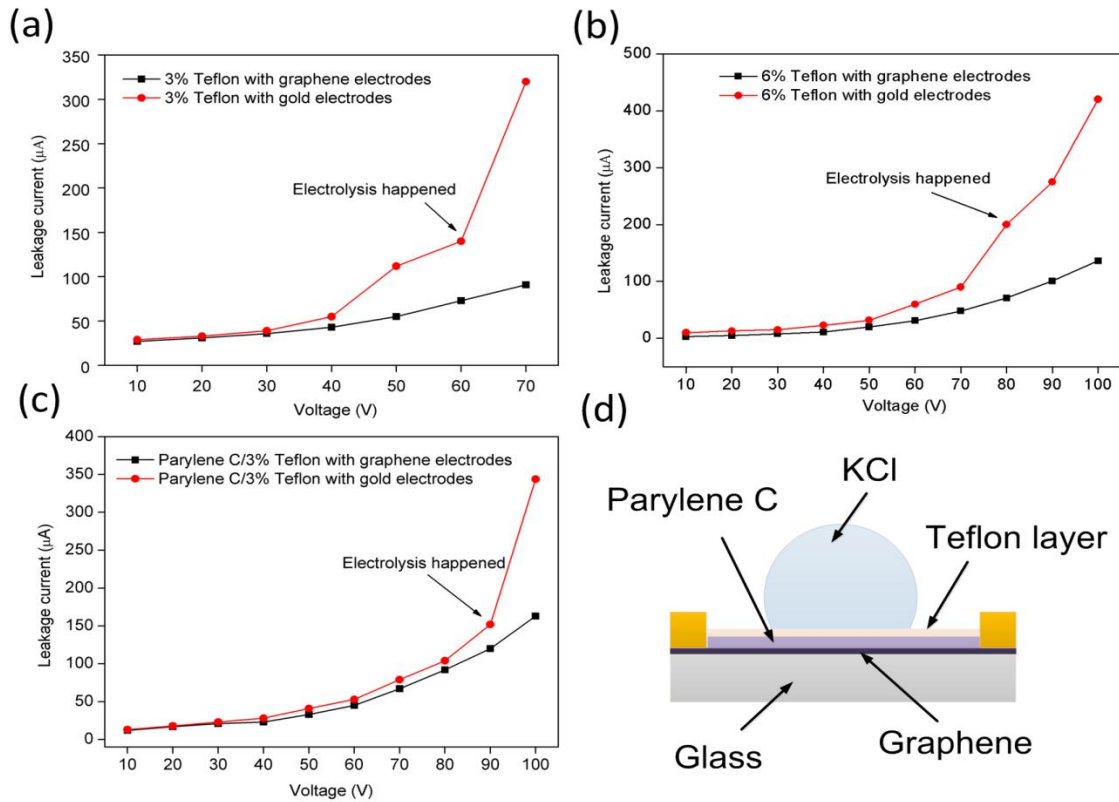


Figure 4.6 Leakage current across the EWOD device with different dielectric layers and electrodes. (a) a 3% Teflon layer with gold and graphene electrodes; (b) a 6% Teflon layer with gold and graphene electrodes; (c) Parylene C as a pinhole-free dielectric layer with a 3% Teflon hydrophobic layer; (d) EWOD device with two-layers stacking (Parylene C/3% Teflon dielectric layers) and graphene electrodes. (The thickness of the Parylene C is around 1 μm .)

We measured the leakage current and the breakdown voltage of dielectric layers of different thicknesses and configuration. The breakdown voltage is defined as the minimum voltage which results in an irreversible EWOD.[147] Figure 4.6(a) showed

leakage current measurements of thin Teflon coatings (3%, 0.55-0.75 μm) on gold and graphene electrodes. The leakage current jumped significantly from 50 μA to 110 μA with applied voltage from 40V to 50V for gold electrode. Electrolysis was observed around 60V. When we used a thicker Teflon layer (6%, 1 μm) as shown in Figure 4.6(b), the leakage currents reduced while breakdown voltage slightly increased. Nevertheless, at high voltage (>80V), leakage current dramatically increased for gold electrodes which was not the case for graphene electrodes. Severe electrolysis was observed on gold electrode when the voltage further increased. With graphene electrodes underneath, the leakage current was less than 200 μA and the breakdown voltage was larger than 100V in both cases (3% and 6% Teflon). Considering pin-hole surfaces and low dielectric constant of the Teflon layer, we also tested the leakage current of two-layers stacking which comprised a Parylene C layer coated with a hydrophobic Teflon layer. Parylene C has a higher dielectric constant (3.1 at 1000Hz), and is considered pinhole free with thickness higher than few nanometers.[148] Figure 4.6 (c) showed that the leakage current could be reduced for both electrode with Parylene C sandwiched between electrodes and Teflon. However, when the applied voltage was larger than 90 V, the dielectric layer began to breakdown on the gold electrodes rather than on graphene electrodes. By testing the EWOD of Parylene C/ Teflon stacking layers on graphene, it was found that the breakdown voltage with graphene electrodes could be larger than 140V without any electrolysis happening. Thus, graphene electrodes allowed Teflon coating to possess a higher breakdown voltage compared to gold electrodes. In addition, and the leakage current in the Teflon/graphene devices was also much smaller than that in

the Teflon/gold electrode devices. This is likely due to the fact that carbon atoms have a wide potential window in the electrode/electrolyte interface.

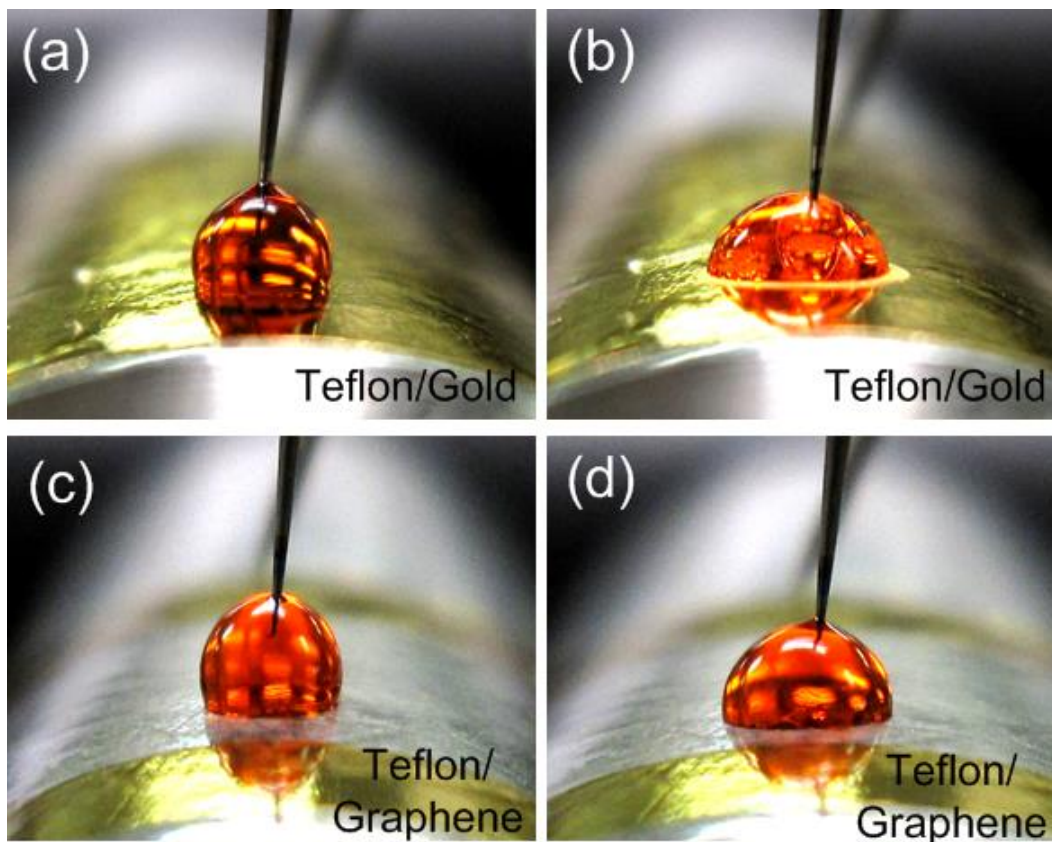


Figure 4.7 EWOD on curved PET films with a gold electrode (a, b) and a graphene electrodes (c, d) coated with Teflon dielectric layers. (a) A gold electrode on a PET film with a 6% Teflon layer with the applied voltage 0V; (b) A gold electrode on a PET film with a 6% Teflon layer with the applied voltage 60V; (c) A graphene electrode on a PET film with a 6% Teflon layer with the applied voltage 0V; (d) A graphene electrode on a PET film with a 6% Teflon layer with the applied voltage 60V. As the voltage increased, the contact angles on both electrodes decreased. Compared to the gold electrode, the graphene electrode was more stable. There were no bubbles (electrolysis) at a high voltage on Teflon-coated graphene. The voltage was AC sinusoidal wave with frequency 1kHz.

Based on our experiments with graphene electrodes and gold electrodes, the Teflon coatings are expected to be more stable on graphene than on gold for EWOD. Unlike gold, whose surfaces are hydrophilic, the surfaces of graphene are hydrophobic.

The interactions between hydrophobic graphene and hydrophobic Teflon may allow Teflon to self-assemble better and provide better adhesion during the coating process. This is further verified in our observation that, under AC 70 V, electrolysis was less likely to occur at Teflon/graphene electrodes than at Teflon/gold electrodes (as indicated by gas bubble generation around the Teflon/gold electrodes, figure 4.5c and figure 4.5d).

	R_S (Ω)	R_T (Ω)	C_T (F)	CPE	α
Teflon/Graphene	2000	1.15×10^6	3.8×10^{-11}	7.2×10^{-9}	0.91
Teflon/Gold	2000	1.08×10^6	4.58×10^{-11}	5.6×10^{-9}	0.66

Table 4.2 Parameters for fitting the Nyquist impedance plot with different electrode materials.

Reversible contact angle can also be observed in curved substrates using graphene. Figure 4.7 shows electrowetting performed on gold electrodes (4.7a and 4.7b) and graphene electrodes (4.7c and 4.7d) deposited on PET films. The KCl droplet (5 μ L 10 mM) with colored food dye was carefully placed on the curved PET film surface. With thickness 50nm, a gold electrode became optically non-transparent, and it blocked the light to transmit through a PET film. In addition, bubbles occurred with the applied voltage 60V due to water hydrolysis. While the breakdown voltage of a dielectric layer (Teflon) could be increased by its thickness, thick Teflon required higher driving voltage for EWOD. In contrast, a graphene electrode is optically transparent. Reversible EWOD on graphene has been observed by applying both DC and AC (10 Hz~1 kHz) voltages.

4.4 Summary

In summary, we demonstrate that the transparent graphene electrode exhibits superior performance in electrowetting on dielectric (EWOD) compared to other commonly-used electrodes such as gold, including higher breakdown voltage, optical transparency, flexibility, and electrical conductivity as well as lower cost. This study provides a new approach to using graphene as a promising transparent conducting electrode material for future EWOD applications. We envision that the improved EWOD properties using graphene as an electrode material will open the door to various applications, including flexible displays and droplet manipulation in three-dimensional microfluidics.

CHAPTER5 DIGITAL MICROFLUIDICS USING GRAPHENE EWOD

5.1 Introduction

Digital microfluidics is a lab-on-a-chip system that based on EWOD technology. It can be used for processing discrete unit-sized packet of fluid with operations such as transport, sort, mix, and react. Digital microfluidics technique has application potential in both biomedical and chemical field. Since we have showed the feasibility of graphene in EWOD system (chapter 4), we would like to know if it is possible to develop graphene-EWOD based microfluidics system for the moving the droplet in micro channels that can be used for detection and analysis of multiplex biological sample in liquid. Most of the digital EWOD devices use metal or ITO electrode materials for applying the electrical field to manipulate the droplet in a hydrophobic channel. Graphene is flexible and electrically conductive, which makes it an ideal electrode material for making the EWOD device on both planer and curved surface.

To design the digital microfluidics device by using graphene, we need to separate a droplet from its source (reservoir) and transport the droplet by the electrical field force. S. K.Cho *et al* developed a model and calculated the critical point of the design parameters to allow moving a droplet. [108] In this model, the static pressure drop inside a droplet should be equal and the droplet starts to separate when the R_1 shows negative. In equation, R_1 and R_2 are the curvature of droplet in the front end and middle point, d is the gap between the top layer electrodes and bottom layer electrodes.

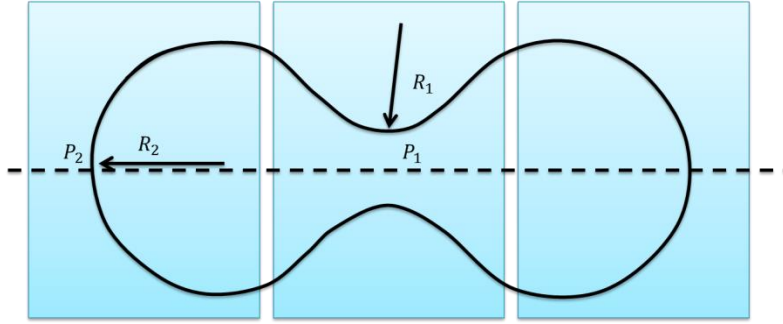


Figure 5.1 Droplets separation in EWOD.

$$\frac{R_2}{R_1} = 1 - \left(\frac{R_2}{d}\right) \frac{\epsilon_0 \epsilon V_d^2}{2\sigma t}$$

To achieve the split of the droplet, the requirements include: (1) necking in the middle of the droplet (Negative R_1) (2) large contact angle change (large V) (3) small gap (d) (4) large radius R_2 at the end regions of the droplet. Here we design a graphene-EWOD based microfluidic system; the objective is to achieve droplet movement on a transparent substrate with graphene electrodes. Figure 5.2 shows the cross-section view and the top view of the graphene EWOD system design. In general, the graphene electrodes are patterned onto a glass substrate and connected with the gold external electrodes. The channel is coated with hydrophobic insulating layer (Teflon AF 1600).

A typical process contains the steps as follows:

1. Alignment mark on glass substrate
2. Graphene transfer onto glass substrates
3. Graphene patterning (photolithography and O₂ plasma etching)
4. Ti/Au electrode patterning (photolithography and E-beam evaporation)
5. Insulating layer coating (Teflon AF 1600, hotplate 160C 10 min, and oven 90C 30 min)
6. Teflon patterning (photolithography and O₂ plasma etching)

7. Electrodes external wires connecting
8. Device assemble (2 layers)

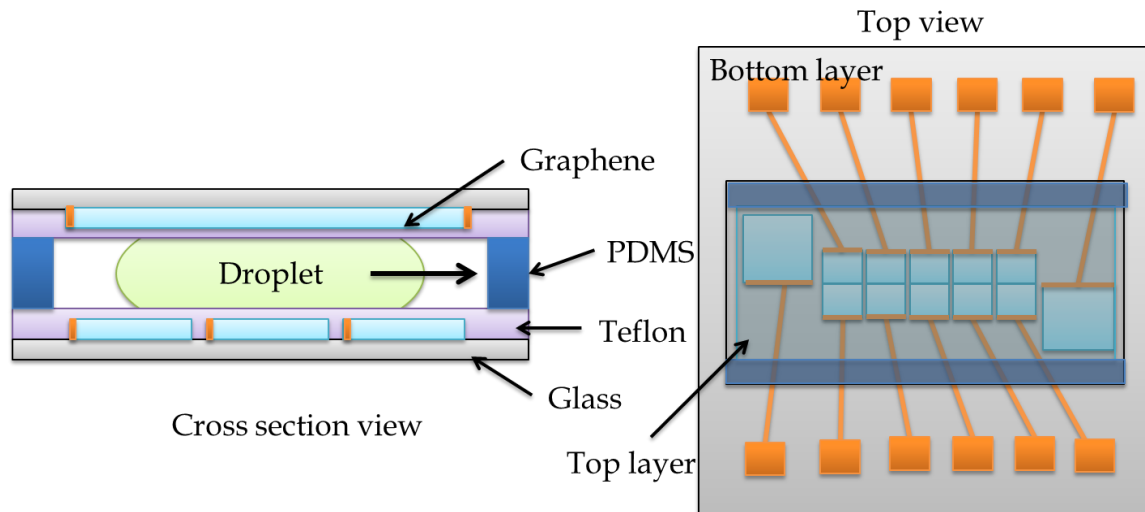


Figure 5.2 Schematics of graphene based EWOD microfluidics system

Current application of EWOD especially optical based devices such as display and lab on chip detection, require the device to be transparent and even flexible.[125] However, most electrodes material which is used in EWOD right now does not have both of these properties. We have demonstrated that graphene with its property of highly optical transparent and mechanical flexible can be used as the electrode material in EWOD.[149] The previous result show that with the Parylen C/Teflon dielectric layer, the graphene based EWOD devices can achieve 40° contact angle change on both glass slide and PET film with 70~100V AC voltage.

In this chapter, we proposed the manipulation of liquid droplet movements using graphene-based electrowetting on dielectrics (EWOD).[150] We show superior EWOD performances can be achieved using graphene thanks to Teflon layers assembled on graphene surfaces that permit low leakage current and less hydrolysis. The interactions

between hydrophobic Teflon and hydrophobic graphene surfaces allow better self-assembly and fewer pinholes of Teflon layers. In contrast, the leakage current of Teflon coated on gold with hydrophilic surfaces is three times higher than that of Teflon on graphene. A wide water window of graphene also allows higher voltage without hydrolysis compared with gold. The fundamental mechanisms of graphene-based EWOD such as leakage currents/impedance were investigated and the feasibility of digital microfluidics using patterned graphene electrodes on transparent substrates was demonstrated.

5.2 Experimental methods

5.2.1 CVD graphene growth

The graphene sheets were grown by using a chemical-vapor-deposition (CVD) method [109]. In detail, a 25 μm thick clean copper foil (Alfa Aesar, 99.9%) was first annealed with 3 sccm hydrogen gas under 40 mTorr at 1000 $^{\circ}\text{C}$ for 1 hour. Then the copper foil was kept in the CVD furnace to cool down to room temperature. To grow graphene, methane gas was used as carbon source and thermally decomposed on copper at high temperature ($>700^{\circ}$). Usually, the furnace was first heated up to 1000 $^{\circ}\text{C}$ with a ramp around 10 $^{\circ}\text{C}/\text{min}$. During this step, a 3sccm hydrogen gas was kept flown into the chamber. Then a mixture of 30 sccm methane and 2 sccm hydrogen gases was flown into the chamber for 30 minutes at 1000 $^{\circ}\text{C}$. The pressure was controlled around 500 mTorr.

5.2.2 CVD graphene transfer

Graphene sheets can be transferred onto different substrates using the following the procedures. First, a thin layer of PMMA was spin-coated on the graphene side of the copper foil and dried at room temperature. Then the backside graphene on the copper was

removed by 100W oxygen plasma. The copper foil was etched by 1 M iron (III) chloride (Sigma, 97%) for at least 3 hours. After copper was fully etched, the PMMA/graphene sheets were carefully scooped out of the iron chloride solution using a piece of glass substrate and rinsed in DI water. Additional clean use diluted hydrogen chloride can help to get better quality of transfer with less metal particle residues. The PMMA/graphene sheets were further rinsed with DI water for three times and finally scooped out using a target substrate (glass slide, PET film) and drying at room temperature. The PMMA layer was then removed by acetone; and the graphene sheet was rinsed several times with isopropyl alcohol (IPA).

5.2.3 EWOD device fabrication process

The fabrication process of the graphene electrodes of the EWOD device is shown in figure 5.3. The graphene was first transferred onto a glass slide substrate using the followed by the method previously mentioned. Then we used standard photolithography to pattern the graphene electrodes into a circular shape. During this step, 1 min oxygen plasma with 30sccm O₂ under 100W was used to etch the graphene electrodes. After etching the graphene, the photoresist was removed by Acetone and followed by baking at 115 °C for 1 min. The Ti/Au contact electrodes were then defined using e-beam evaporation and photolithography. After lift-off, the whole substrates were coated with 1 μm Parylene C. Finally a thin layer of Teflon was spin-coated on top of the Parylene as a hydrophobic layer.

The top layer electrodes were fabricated using an ITO glass coated with Parylene C and Teflon. The two electrodes plates were separated using double-side scotch tape with a gap about 100 μm. A 1.5 μL KCl droplet was introduced into the central electrodes

area with a pipette. The electrodes were wired to a circuit board functioned the PIC controlled sequential switches and power amplifier. The output voltage to active the droplet moving is about 70 V.

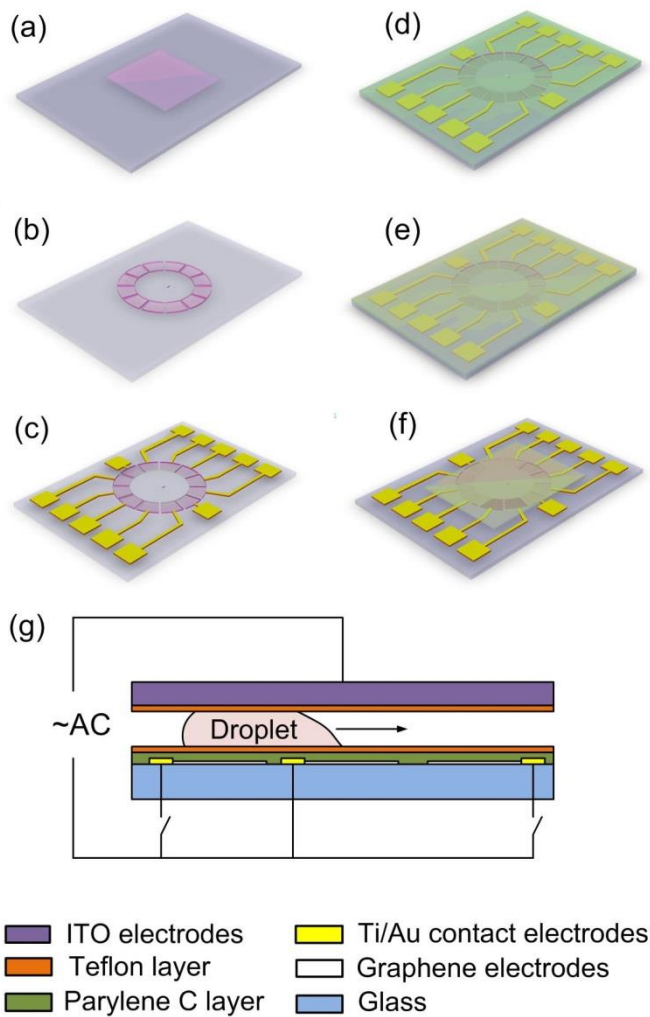


Figure 5.3 Process flow of bottom electrodes (graphene electrodes). (a) Transfer graphene onto a glass substrate, (b) Pattern graphene electrodes using photolithography and oxygen plasma etching, (c) Lift-off Ti/Au electrodes, (d) Deposit a Parylene C dielectric layer, (e) Spin-coat a Teflon layer, (f) Remove dielectric layers on the Ti/Au contact electrodes. (g) A schematic view of digital microfluidics using graphene electrodes.

5.3 Results and discussion

Figure 5.4 shows a typical graphene based digital EWOD device. The conducting area of the graphene electrodes were highlighted in the figure 6.4b. Each graphene

electrode was connected with an external Ti/Au electrode pads for applying the voltage. Since the graphene is a flexible and transparent electrode materials. This protocol can also be used on other electronic system, such as flexible PCB board, and PET film. Compare to traditional EWOD system which can only use ITO, semiconductor, and metal electrodes, graphene electrode can provide the most extensive application such as biology detection and display technology.

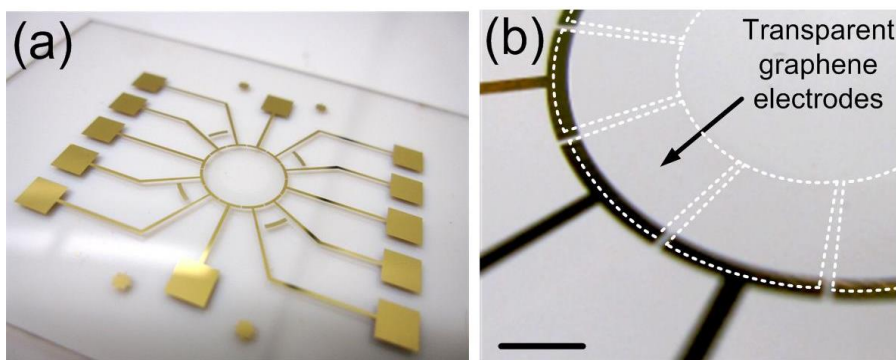


Figure 5.4 (a) An optical image of graphene electrodes with Ti/Au contact pads. (b) Zoom-in image of the transparent graphene electrodes on glass. Scale bar: 1mm.

Here we used a home-built optical system to measure the contact angle change of graphene electrode with ParyleneC /Teflon dielectric layer. The system consists of a Navitar 12X zoom lens, a white light semi-flexible fiber optical source and a USB CCD camera (iSolution). A Labview module was used to control a function generator (Agilent 33120A) and an AC power amplifier. The CCD camera was also programmed using the Labview software to record movies with a maximum frame rate of 60 fps. The system is capable of generating AC voltages from 0 V~140 V with a frequency between 10 Hz and 10 KHz. For EWOD, KCl solution (10 mM, 100 mM) was used. Figure 5.5 shows by using a pinhole free dielectric layer (Parylene C) sandwiched between graphene and Teflon, the breakdown voltage of dielectric layers increased, which allowed a higher

contact angle change ($\sim 36^\circ$) as shown in Fig 5.5. We also noticed that by using the Parylene C layer, the vibration of the droplet during its wetting can also be reduced due to the more smoothed Teflon surface. We have also tested the cyclability of the electrowetting on Parylene C/ Teflon system with graphene electrodes, the results show that the system is highly stable. The DC voltage is also tested and shows similar electrowetting performance compared to AC mode.

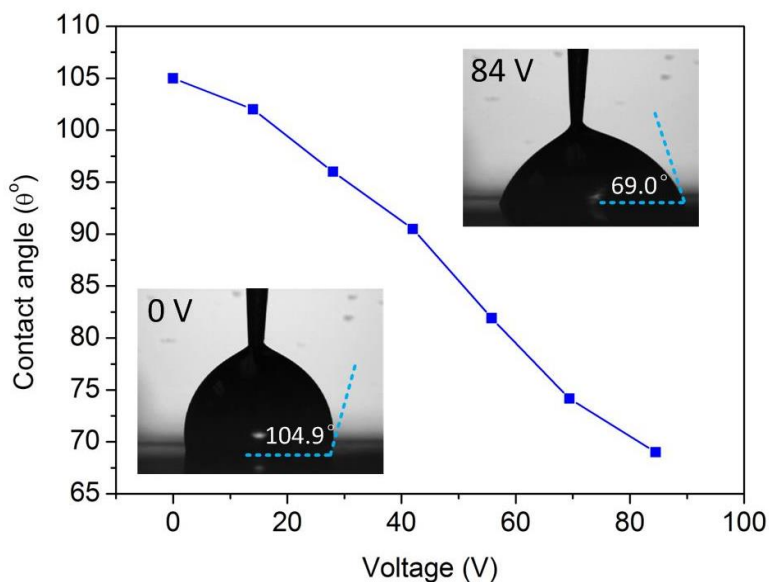


Figure 5.5 Contact angle change on Parylene C/ 3% Teflon coated graphene electrodes. The voltage was from 0V to 84 V, AC 1kHz.

The leakage current was tested here for comparing the electrowetting stability between graphene electrode and gold electrode with different dielectric system. The leakage current was measured by a digital multimeter (Agilent 34401A) using the setup system in figure 5.6. Figure 5.7 showed leakage current of the thin Teflon coatings (3%, 0.55-0.75 μm) on gold and graphene electrodes. Here we used 100mM KCl solution to test the leakage current. On Teflon/gold electrode, the leakage current was jumped significantly from 50 μA to 110 μA with applied voltage increased from 40V to 50V. For

graphene electrode, the leakage current was lower than 90 μA even the voltage increased to 70V, which the leakage current on Teflon/gold is above 300 μA . We also found bubbles on the Teflon/gold electrodes, which showed electrolysis on Teflon/gold around 60V. When we used a thicker Teflon layer (6%, 1 μm), the leakage currents reduced while breakdown voltage slightly increased. Nevertheless, at high voltage ($>80\text{V}$), leakage current dramatically increased for gold electrodes which was not the case for graphene electrodes. Severe electrolysis was observed on gold electrode when the voltage further increased. With graphene electrodes underneath, the leakage current was less than 200 μA and the breakdown voltage was larger than 100V in both cases (3% and 6% Teflon). Considering pin-hole surfaces and low dielectric constant of the Teflon layer, we also tested the leakage current of two-layers stacking which comprised a Parylene C layer coated with a hydrophobic Teflon layer. Parylene C has a higher dielectric constant (3.1 at 1000Hz), and is considered pinhole free with thickness higher than few nanometers.[85] Figure 5.7 (b) showed that the leakage current could be reduced for both electrode with Parylene C sandwiched between electrodes and Teflon. However, when the applied voltage was larger than 90 V, the dielectric layer began to breakdown on the gold electrodes rather than on graphene electrodes. By testing the EWOD of Parylene C/Teflon stacking layers on graphene, it was found that the breakdown voltage with graphene electrodes could be larger than 140V without any electrolysis happening. Thus, graphene electrodes allowed Teflon coating to possess a higher breakdown voltage compared to gold electrodes. In addition, and the leakage current in the Teflon/graphene devices was also much smaller than that in the Teflon/gold electrode devices. This is

likely due to the fact that carbon atoms have a wide potential window in the electrode/electrolyte interface.

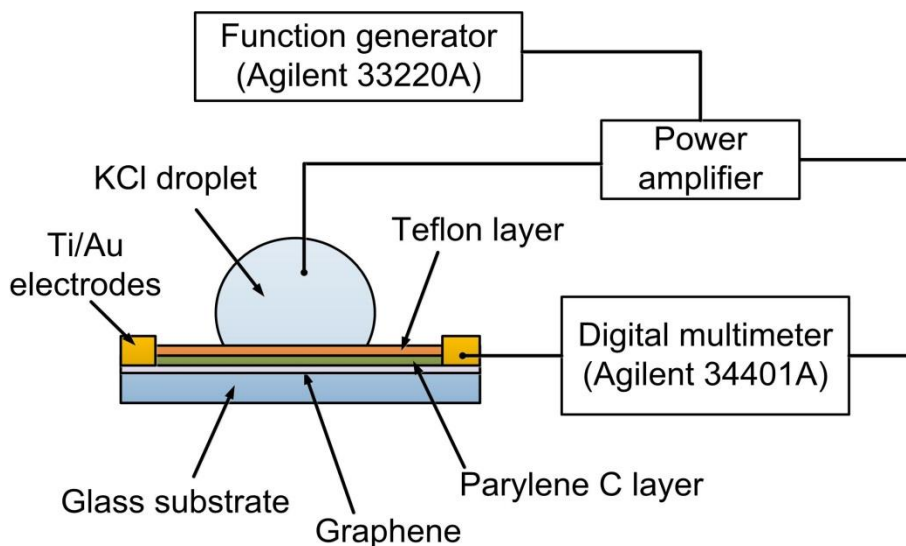


Figure 5.6 A system for leakage current test.

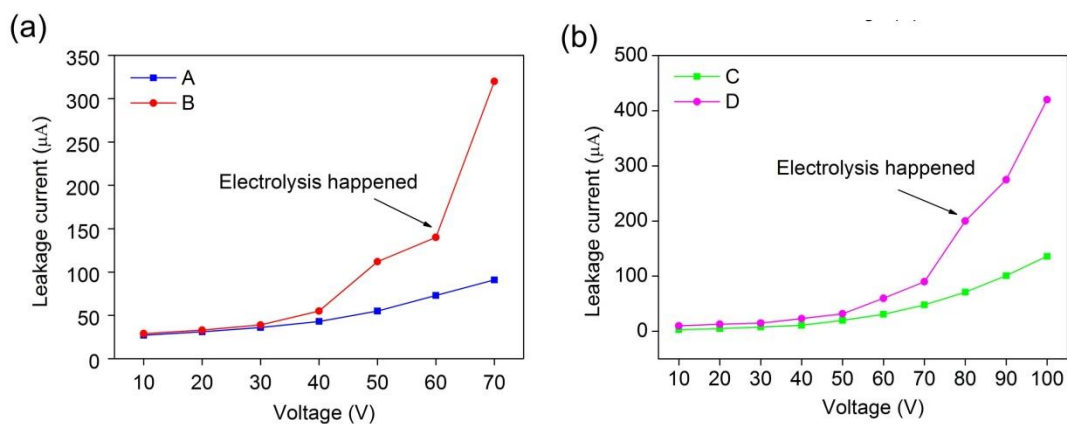


Figure 5.7 Comparison of leakage currents in the dielectric layers using different electrodes. (A)3% Teflon with graphene, (B) 3% Teflon with gold, (C)Parylene C/ 3% Teflon with gold, (D)Parylene C/ 3% Teflon with graphene.

Figure 5.8 showed the manipulation of a KCl liquid droplet movement using sequential switching voltage that was controlled by a programmable logic controller (PLC) relay array. 1kHz 70V AC voltage was used to drive liquid droplets. The voltage was applied on each electrode for 5 seconds before the next electrode was switched on.

We show it is feasible to manipulate droplet movement using graphene-based EWOD. Figure 5.9 showed a more detailed droplet movement with time frame on a square graphene electrode patterned EWOD devices. Same voltage was used here as the circular shape device. On this device, we used faster switching time (1s). It was observed that the movement of the droplet is responsive and highly repeatable. The moving direction and be easily programmed with the PLC controller.

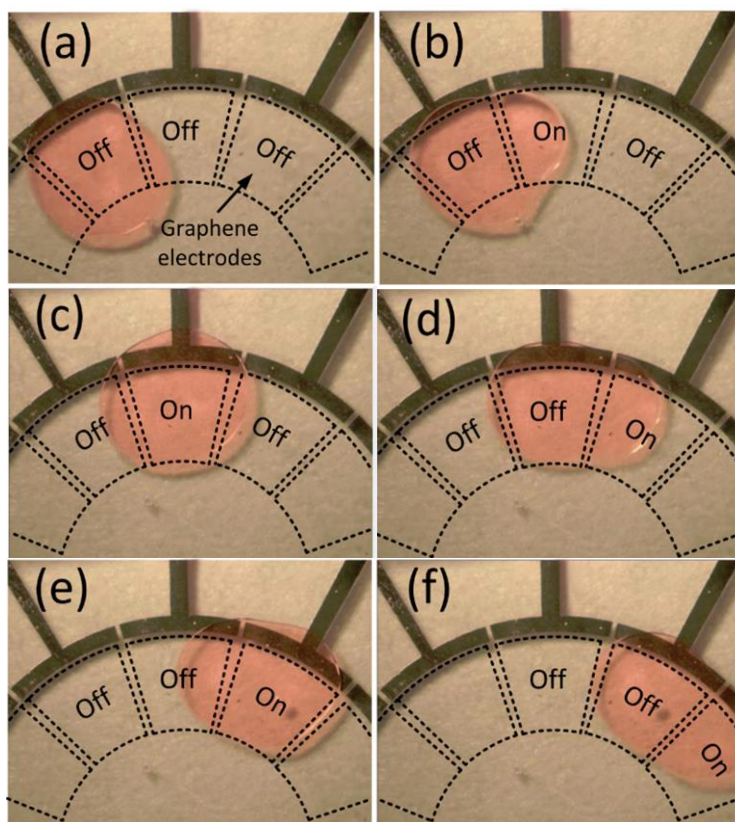


Figure 5.8 Control of droplet movements using graphene based EWOD. The voltage was AC 70V (1kHz) and the droplet was $1.5\mu\text{L}$ KCl (100mM). The droplet moved from the left side to the right side as voltage was sequentially turned on.

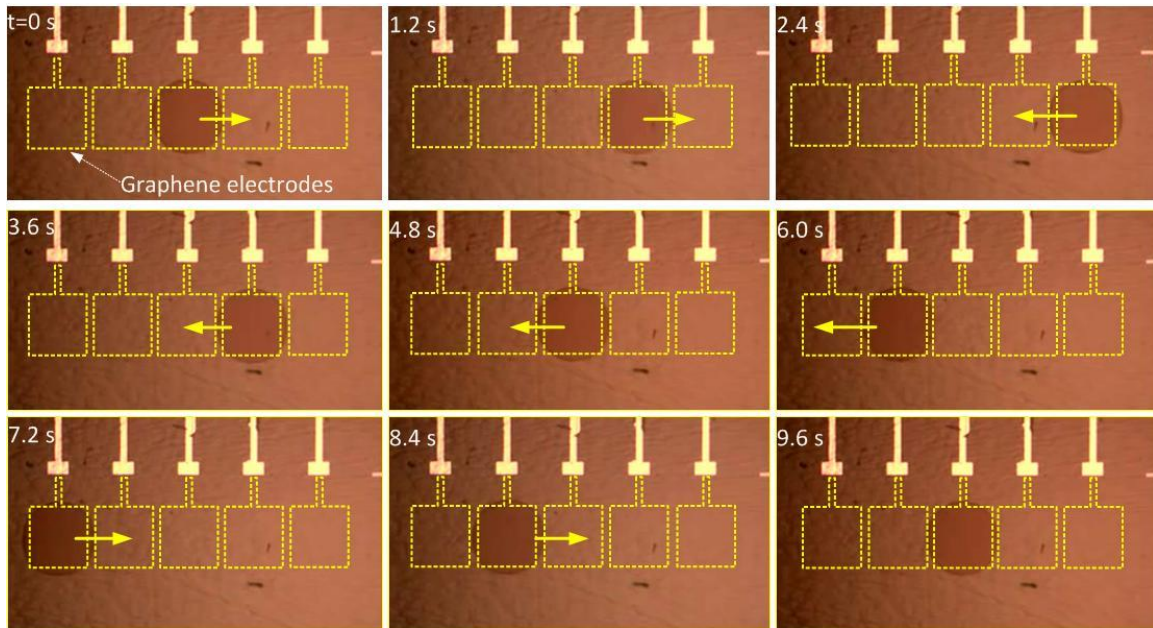


Figure 5.9 The droplet movement on graphene EWOD device with square electrodes.

5.4 Summary

In this chapter, we further demonstrated the capability of building digital microfluidics system using graphene electrodes instead of traditional metal and ITO electrodes. We suggest that with pin-hole free dielectric layer protection, the graphene can have higher breakdown voltage and lower leakage than gold electrodes. In additional, future applications such as flexible, total transparent electrowetting can be realized by using graphene electrodes.

CHAPTER 6 CONCLUSION AND FUTURE WORK

6.1 Conclusion

In this thesis work, we developed the applications of biosensing and microfluidics using CVD graphene. For graphene sensor devices, we focused on 1) the engineering of the graphene edge defects for the sensitivity enhancement using EBL, and 2) the surface functionalization of graphene for bio-specific binding. For the EWOD application, we first time demonstrated the integration of CVD graphene as the transparent and flexible ground electrode materials with the dielectric insulating layer. In addition, we proved the droplet manipulation on planer surface with the graphene electrode.

In Chapter 2, we reported a systematic study of the effects of defects and edges on the pH response of graphene pH sensors by 1) correlating Raman spectroscopy with pH-induced gate voltage shifts in the transfer characteristics of graphene FETs; and 2) patterning 2D graphene sheets into arrays of GNRs to significantly increase the density of attached hydroxyl groups. We observed a slightly increased pH response in graphene devices with a higher level of disorder as quantified by the D-band to G-band intensity ratio in the Raman spectra of the device channel made of chemical vapor deposition (CVD) grown graphene. We further demonstrated that the sensitivity of graphene pH sensors could be controllably increased by patterning the graphene channel into arrays of GNRs with decreasing width, without degrading the electrical properties of the graphene channel. The pH response of the devices increased as the width of the GNR reduced down to 200 nm, which can be attributed to the increased number of hydroxyl groups attached to the edges per unit area as the edge to surface area ratio increases with decreasing GNR width.

In Chapter 3, we developed a graphene biosensor for specifically detecting of *E.coli* bacteria. Functionalization of graphene with saline using solution immersion method was performed. We also studied the functionalization of graphene with P22 phage and *E.coli* phage to compare the bacteria binding efficiency with bacteria. By using APTES and Glutaraldehyde, we successfully immobilized the *E.coli* TSPs to the CVD graphene. Further experiment show that *E.coli* bacteria can be attached to the *E.coli* TSPs through specific binding.

In Chapter 4, we demonstrated the superior performance of graphene electrode in electrowetting on dielectric (EWOD) compared to other commonly-used electrodes such as gold, including higher breakdown voltage, optical transparency, flexibility, and electrical conductivity as well as lower cost. We also observed low leakage current and less hydrolysis of graphene electrode with Parylene/Teflon dielectric system. This study provided a new approach of using graphene as a promising transparent conducting electrode material for future EWOD applications.

In Chapter 5, we proposed the manipulation of liquid droplet movements using graphene-based electrowetting on dielectrics (EWOD). [150] [149] [148] [148] [148] [147] [146] [145] A double plate planer EWOD device was designed with CVD graphene as the ground electrodes. We designed both circular shape and square shape electrode patterns with graphene and both of them were able to move the droplet under an applied voltage between the electrode plates above 70 V. The experiments provided an alternate electrode material candidate for the digital microfluidics application.

All the graphene materials in our experiment uses CVD grow graphene. Compared to other graphene fabrication method, CVD graphene method is a promising

technique for its capability of large scale integration with good electrical mobility and conductivity. In the last, we also described the process of CVD graphene growth on copper, and compared the transfer process using different method. The EBL process for fabricating GNR was also discussed.

6.2 Future work

Although this work gives some proof of concept results for graphene biosensing and EWOD application. However, it should not be considered as an end, but rather as just a start. First of all, for the graphene biosensor, the functionalization with specific biomolecule without changing the electrical properties is still a big challenge. In our experiment in Chapter 3, although we have compared the gate potential change before and after the binding of the bacteria, the electrical property of the graphene before and after the TSP immobilization has not been studied yet. Since the top gate results have showed a huge doping from the single bacteria, it is worth to see the sensing capability of the graphene FET through the back gate measurement. Additionally, the sensitivity of the graphene FET in response to the channel size will give us more about the sensing mechanism. Graphene has a chemically inert basal surface and can it be used as the reference electrode for electrochemical sensing? If so, it will benefit to make the sensing device embedded with microfluidics system for detecting ions and biomolecules. And finally, the edge functionalization of graphene has not been fully studied. For the graphene electrode application, we have demonstrated the EWOD phenomena on graphene; it will be interesting to find some real applications by using the advantages of the graphene EWOD devices such as flexibility, transparent, high reliability.

APPENDIX A

A.1 Single layer graphene synthesis by CVD

The single layer graphene films used in this study were grown by using chemical-vapor deposition (CVD) method. CH_4 gas was used as the carbon source, and was thermally decomposed on copper at high temperature. A clean copper foil (Alfa Aesar) was annealed in a vacuum furnace for 2 hours with a 5 sccm H_2 gas flow and a pressure around 0.4 mTorr at 1000 °C. For graphene growth, a mixture of 30 sccm CH_4 and 2 sccm H_2 gases was flown into the furnace for 30 minutes at 1000 °C. The pressure was controlled around 500 mTorr.

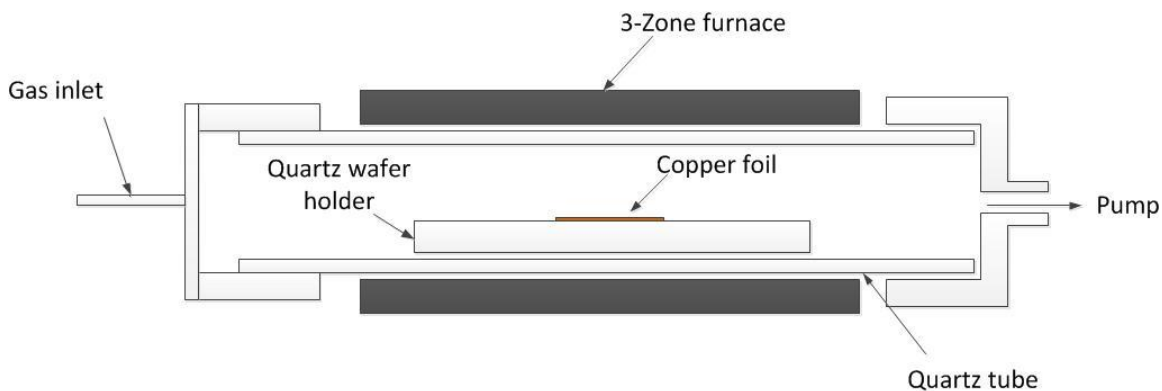


Figure A.1 A typical CVD furnace setup for graphene growth (on copper).

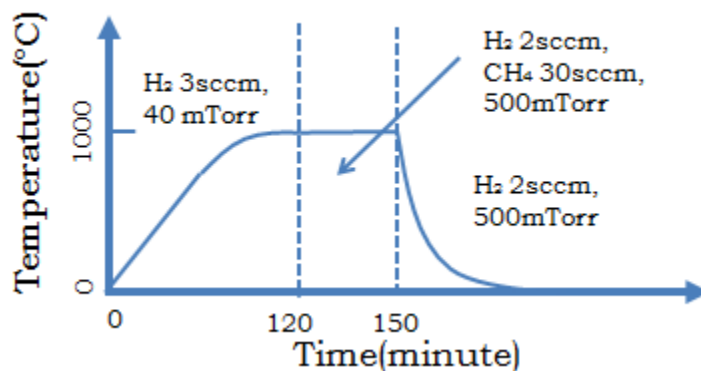


Figure A.2 A typical time dependent CVD experiment condition for graphene growth (flow rate, pressure, temperature).

Figure A.3 shows an SEM image of CVD graphene after using the above method. During the growth process, we noticed that some multilayer graphene will also appear (shown as the black area in the picture). The coverage of one layer graphene is above 90% in most of the cases. We also found that to the quality of the graphene is also related to the surface roughness of the copper foil that we used. It is generally observed that the flat copper will get better graphene growth results than the rough copper. In order to get flat copper, anneal is always used before the graphene growth, the anneal process is similar to the CVD graphene process. During the process, we used 3 sccm hydrogen gases to anneal the surface of the copper at 1000 C° for 1 hour. The whole process including the cooling down can take about 4 to 6 hours.

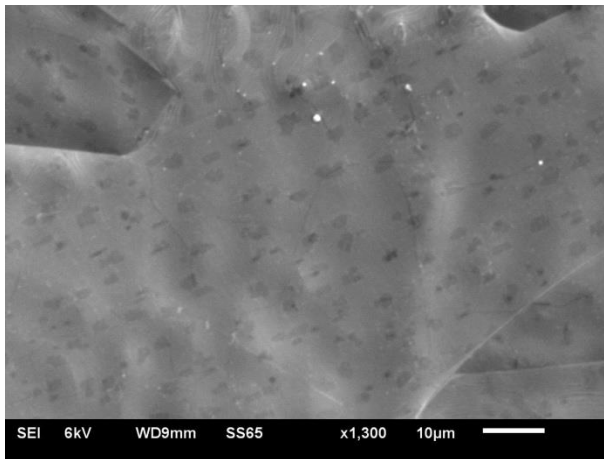


Figure A.3 An SEM image of CVD graphene after growth on copper foil, the black islands show the multilayer areas.

A.2 Comparison of different CVD graphene Transfer process

A.2.1 CVD graphene Transfer process by using FeCl_3 etching

A typical transfer process for CVD graphene is showed in figure A.4. Briefly, a thin layer of PMMA 495 (100 nm ~200 nm) was spin-coated (3000 rpm) on the copper foil with graphene on it and dried at room temperature for half an hour. Subsequently, the copper was etched in a 1 M ferric chloride (FeCl_3) with PMMA side facing up. The floating PMMA/graphene sheets were then carefully scooped out of FeCl_3 solution using a piece of glass slide and rinsed with DI water. After the whole sheets were attached to the substrates, they were taken out of the beaker and dried for 1hour at room temperature. The PMMA was removed by acetone or chloroform; and the graphene sheet was rinsed several times in isopropyl alcohol (IPA) and demonized (DI) water.

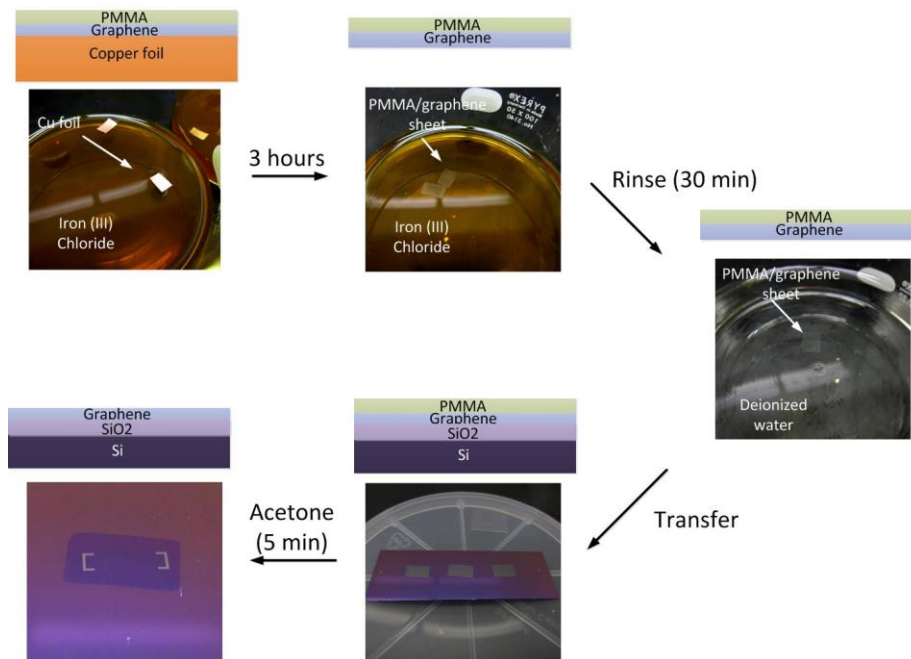


Figure A.4 A typical CVD graphene wet transfer process by using FeCl_3 .

A.2.2 CVD graphene Transfer process by using modified RCA clean

We noticed that when using the method introduced in A.2.1, some unsoluble nanoparticles will be deposited to the graphene and cause the contamination of the graphene samples. Those nanoparticles will not be able to remove even after high temperature anneal. In order to solve the problem, we developed a more effective method that based on the Liang *et al.*[86]. In the process, we first remove the copper foil by using the diluted copper etchant (APS-100) for overnight. Then we put the PMMA/graphene sheet into a beaker with diluted ammonia solution ($\text{H}_2\text{O}_2:\text{H}_2\text{O}:\text{NH}_4\text{OH}=20:1:1$) to remove the organic residue attached to the graphene. After rinse with the above solution for at least 15 min, we clean the sheets with DI water and then put them into the diluted Hydrochloric acid (HCl) solution ($\text{H}_2\text{O}_2:\text{H}_2\text{O}:\text{HCl}=20:1:1$) for at least 15 min to remove the inorganic waste. We found that by using this method, the graphene is much cleaner

than the one we transferred using FeCl_3 etching. Also the diluted solution will not cause the damage to the graphene.

Figure A.5 showed the AFM images of the CVD graphene transferred with two different methods. The graphene showed in figure A.4 (a) was etched with the APS copper etchant and cleaned with the diluted RCA solution. It is much smooth and cleaner than the graphene showed in figure A.4 (b) which was transferred without the RCA clean. The scan area of the AFM image was $5\ \mu\text{m} \times 5\ \mu\text{m}$ with tapping mode.

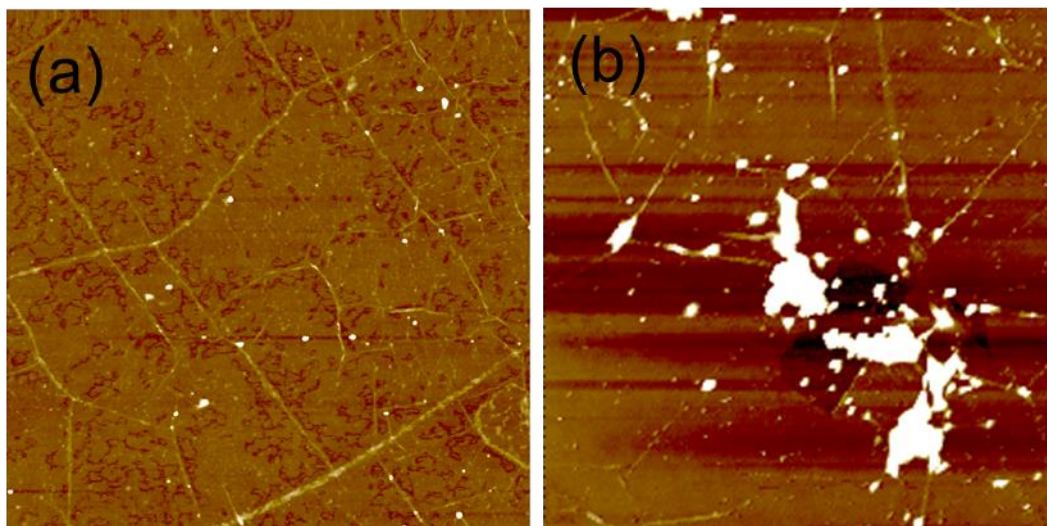


Figure A.5 AFM microscope images of CVD graphene transferred on silicon substrate with a 300 nm thick thermal oxide after (a) modified RCA clean with diluted Hydrochloric acid and ammonia solution, the surface is clean and only very few contamination are remaining on the graphene surface (b) graphene transferred with FeCl_3 and without modified RCA clean, showed very rough surface and some residues are still remaining.

We also notice that it is not necessary to use oxygen plasma to treat the substrate before graphene transfer. Oxygen plasma will introduce hydroxyl groups and oxygen groups to the substrates and because of the existing of these groups, during the transfer process, moistures will be difficult to remove. Under the optical microscope, the graphene will show a blue color compared to the original dark purple color as the figure

A.6 showed. Also after the e-beam lithography patterning and oxygen plasma etching, the stain of moisture will still remain on the substrate.

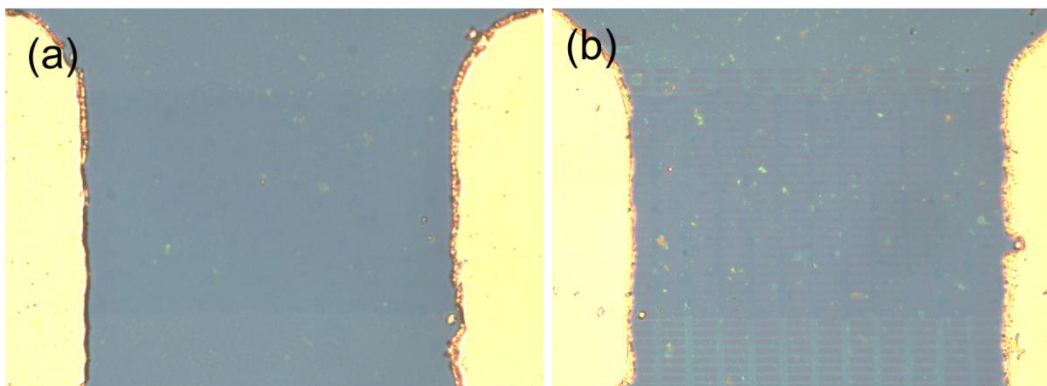


Figure A.6 (a) CVD graphene transferred onto SiO₂/Si substrate with oxygen plasma, (b) after e-beam patterning, showed the blue stain remain on the substrate.

A.3 Graphene sheet patterning

Graphene can be patterned by either photolithography or electron-beam lithography (EBL) combined with oxygen plasma etching. For photolithography, S1811 photoresist was spin coated onto the graphene sheets at 4000rpm (30s, 1.1 μm thick). We used a mask aligner (MA150) to expose photoresist for 8 seconds under a hard contact mode. After being developed for 30 seconds with CD-30, the graphene was etched by using oxygen plasma (Drytek). The parameters were oxygen 30 sccm, power 100 W, and 1 minute. The photolithography can only produce graphene channel larger than 5 μm because of the limit of optical diffraction. For smaller features (around 0.5 μm), we use E-beam lithography (EBL) to pattern the graphene. A 200nm Poly (methyl methacrylate) PMMA was spin-coated onto the graphene sheets and baked under 180 °C using a hotplate for 5 min. In specific, 100~150 nm line pattern could be fabricated with 1000X magnification and 10kV. After exposure, the PMMA was developed in the solution of

Methyl isobutyl ketone (MIBK) (30:1). After development, the devices were ready for oxygen plasma etching.

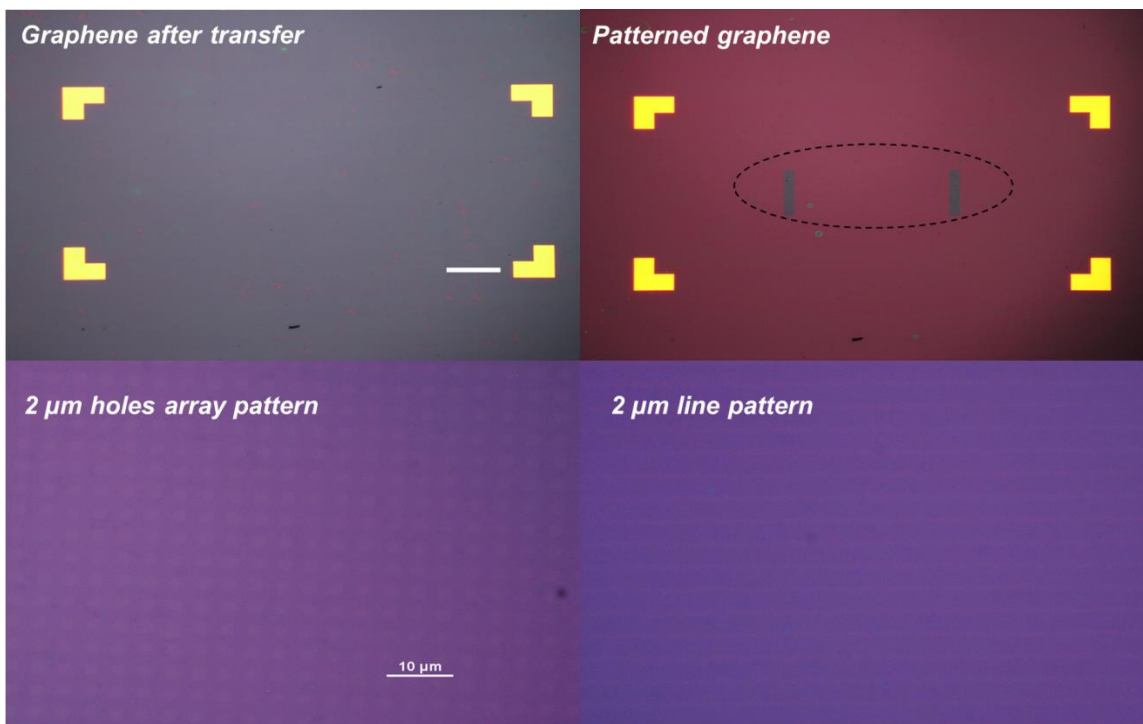


Figure A.7 Optical microscope images of CVD graphene before patterning with photolithography and oxygen plasma etching (top left), after patterning (top right), 2 μm holes array pattern (bottom left), 2 μm wide line pattern (bottom right).

Figure A.7 showed the patterns that we have made using photolithography and oxygen plasma. With current lithography system (EVG 620), the smallest feature size of the graphene pattern is 2 μm.

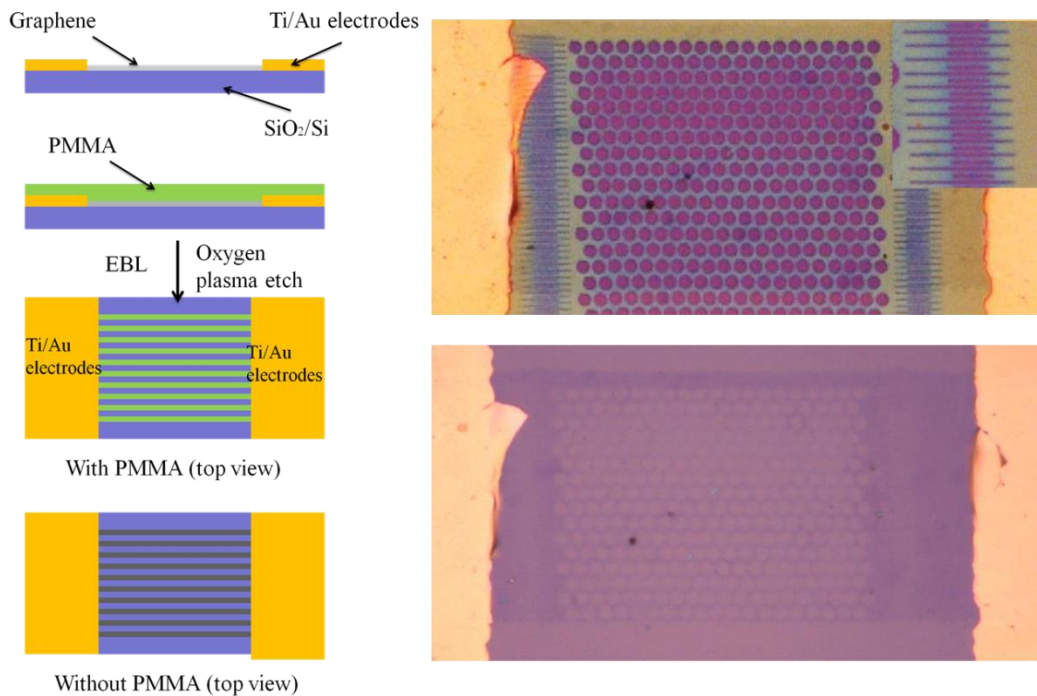


Figure A.8 Process flow of the e-beam lithography for writing sub-micron pattern on the graphene FET sensor device (left), graphene FET patterned with circular shape holes and lines with PMMA covered (top right), and after remove PMMA (bottom right).

Figure A.8 illustrated the process flow of the e-beam lithography for writing sub-micron pattern on the graphene FET sensor device. The top right figure showed the circular pattern and line pattern written by using PMMA e-beam resist. The bottom right figure showed the device with patterned graphene after removed the PMMA. It is noticed that the PMMA may be more difficult to remove after EBL due to the crosslink during the e-beam lithography process. Thermal annealing and hot acetone immersion will help to remove most of the residue but not perfectly.

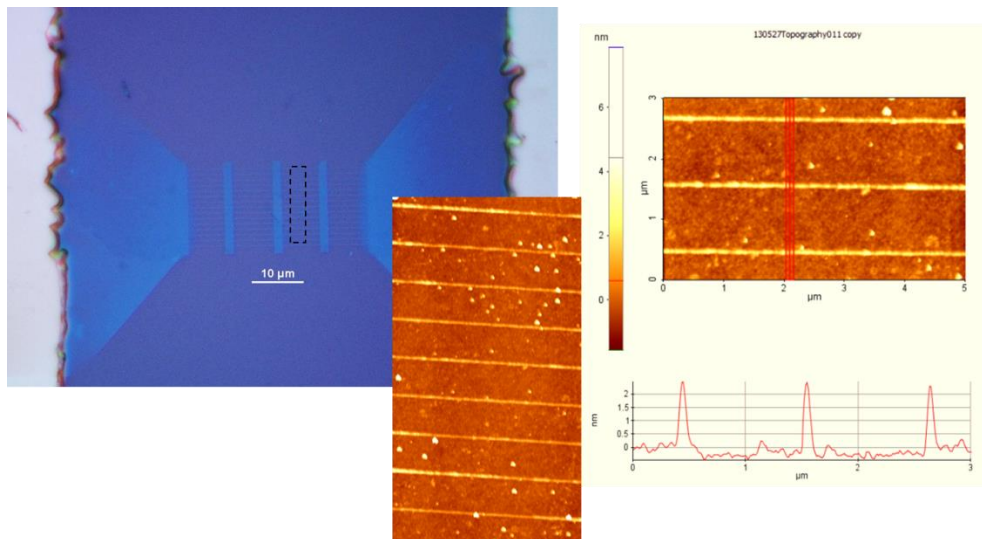


Figure A.9 Graphene nano ribbon pattern wrote by EBL with HSQ e-beam resist. The line width was only 100 nm.

Figure A.9 demonstrated the EBL method that we used in chapter 2 for making the graphene nano ribbon arrays less than 100 nm. For this process, it is important to properly control the expose dose to prevent the proximity effect. During the oxygen plasma etching process, the graphene ribbon underneath the HSQ can be over etched due to the undercut etching. It is necessary to shorten the etching time for about 50%, usually 10s~15s. Also to remove the HSQ covered on graphene ribbon, BOE was used.

A.4 External contact electrode and lift-off

The electrodes for external contact were fabricated by Electron-beam evaporation (BJD 1800, Temescal). An evaporation process was used to deposit material (source) on substrates by heating the materials to the point where it started to melt and evaporate. This process took place inside a vacuum chamber, enabling the molecules to evaporate freely in the chamber. Metal molecules would condense on the substrates. For e-beam evaporation, an electron beam was used to heat the source material. Compared to E-beam evaporation, physical evaporation methods like sputtering may cause graphene structure

defects by ion bombardment (Ar ions plasma) and by impurities from a gas mixture. To make electrode for external contact on the graphene sheet in devices, 5 nm Cr/ 50 nm Au (5 nm Ti/ 50 nm Au) was deposited using electron beam evaporation. After evaporation, we used Acetone/PG remover under 70 °C for lift-off in order to remove excess metal layers. During the lift-off process, ultrasonic cleaning was avoided because of the vibration of substrate can cause the damage to the graphene sheets. In general, we use gentle shaking to accelerate the lift-off process.

APPENDIX B

B.1 Microfluidics fabrication using PDMS (Polydimethylsiloxane)

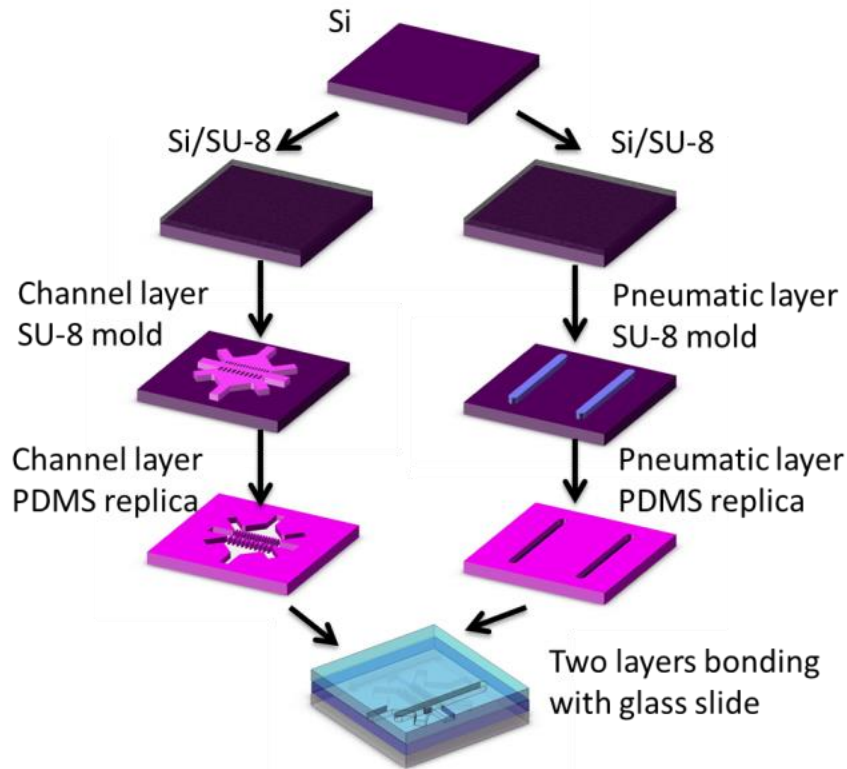


Figure B.1 A typical fabrication process of the two-layer microfluidics.

The fabrication of the microfluidic channels was adapted from standard soft lithography method as shown in figure 1. The two-layer microfluidic network was made by PDMS RTV 615 (GE) and sealed with a glass substrate. For one-layer device, Sylgard 184 is usually used. First, 200 μm thick SU-8 (Microchem SU-8 100) was spin coated on the silicon wafers. After hard bake with hot plate at 95 $^{\circ}\text{C}$, the SU-8 was exposed for 150 s and followed by 30 min post exposure bake. The fluidic channel was made by 250 μm PDMS replica (part A: part B = 20:1) and the pneumatic layer was made by a 4 mm thickness PDMS replica (2:1). The PDMS replicas were baked using the hotplate for 1 hour under 80 $^{\circ}\text{C}$. For bonding, the two PDMS replicas were first treated with corona

discharge for 30 s and then baked at 80 °C for 10 min. Finally, the PDMS replica was treated with corona discharge for 30 s and sealed with a glass slide. The whole device was baked at 80 °C for 10 min to enhance the bonding force.

BIBLIOGRAPHY

- [1] S. Iijima, "Helical Microtubules of Graphitic Carbon," *Nature*, vol. 354, pp. 56-58, Nov 7 1991.
- [2] H. W. Kroto, J. R. Heath, S. C. O'Brien, R. F. Curl, and R. E. Smalley, "C-60 - Buckminsterfullerene," *Nature*, vol. 318, pp. 162-163, 1985.
- [3] K. S. Novoselov, A. K. Geim, S. V. Morozov, D. Jiang, Y. Zhang, S. V. Dubonos, I. V. Grigorieva, and A. A. Firsov, "Electric field effect in atomically thin carbon films," *Science*, vol. 306, pp. 666-669, Oct 22 2004.
- [4] J. M. Rosenholm, E. Peuhu, J. E. Eriksson, C. Sahlgren, and M. Lindén, "Targeted intracellular delivery of hydrophobic agents using mesoporous hybrid silica nanoparticles as carrier systems," *Nano Letters*, vol. 9, pp. 3308-3311, 2009.
- [5] P. R. Wallace, "The Band Theory of Graphite," *Physical Review*, vol. 71, pp. 622-634, 1947.
- [6] X. Huang, Z. Y. Yin, S. X. Wu, X. Y. Qi, Q. Y. He, Q. C. Zhang, Q. Y. Yan, F. Boey, and H. Zhang, "Graphene-Based Materials: Synthesis, Characterization, Properties, and Applications," *Small*, vol. 7, pp. 1876-1902, Jul 18 2011.
- [7] P. Avouris, "Graphene: Electronic and Photonic Properties and Devices," *Nano Letters*, vol. 10, pp. 4285-4294, Nov 2010.
- [8] K. S. Novoselov, Z. Jiang, Y. Zhang, S. V. Morozov, H. L. Stormer, U. Zeitler, J. C. Maan, G. S. Boebinger, P. Kim, and A. K. Geim, "Room-temperature quantum hall effect in graphene," *Science*, vol. 315, pp. 1379-1379, Mar 9 2007.

- [9] K. I. Bolotin, K. J. Sikes, Z. Jiang, M. Klima, G. Fudenberg, J. Hone, P. Kim, and H. L. Stormer, "Ultrahigh electron mobility in suspended graphene," *Solid State Communications*, vol. 146, pp. 351-355, Jun 2008.
- [10] X. Du, I. Skachko, A. Barker, and E. Y. Andrei, "Approaching ballistic transport in suspended graphene," *Nature Nanotechnology*, vol. 3, pp. 491-495, Aug 2008.
- [11] A. H. Castro Neto, F. Guinea, N. M. R. Peres, K. S. Novoselov, and A. K. Geim, "The electronic properties of graphene," *Reviews of Modern Physics*, vol. 81, pp. 109-162, Jan-Mar 2009.
- [12] F. Banhart, J. Kotakoski, and A. V. Krasheninnikov, "Structural Defects in Graphene," *ACS nano*, vol. 5, pp. 26-41, Jan 2011.
- [13] J. Lahiri, Y. Lin, P. Bozkurt, I. I. Oleynik, and M. Batzill, "An extended defect in graphene as a metallic wire," *Nature Nanotechnology*, vol. 5, pp. 326-329, May 2010.
- [14] C. O. Girit, J. C. Meyer, R. Erni, M. D. Rossell, C. Kisielowski, L. Yang, C. H. Park, M. F. Crommie, M. L. Cohen, S. G. Louie, and A. Zettl, "Graphene at the Edge: Stability and Dynamics," *Science*, vol. 323, pp. 1705-1708, Mar 27 2009.
- [15] J. C. Meyer, C. Kisielowski, R. Erni, M. D. Rossell, M. F. Crommie, and A. Zettl, "Direct Imaging of Lattice Atoms and Topological Defects in Graphene Membranes," *Nano Letters*, vol. 8, pp. 3582-3586, Nov 2008.
- [16] M. C. Lemme, D. C. Bell, J. R. Williams, L. A. Stern, B. W. H. Baugher, P. Jarillo-Herrero, and C. M. Marcus, "Etching of Graphene Devices with a Helium Ion Beam," *ACS nano*, vol. 3, pp. 2674-2676, Sep 2009.

- [17] R. Balog, B. Jorgensen, L. Nilsson, M. Andersen, E. Rienks, M. Bianchi, M. Fanetti, E. Laegsgaard, A. Baraldi, S. Lizzit, Z. Sljivancanin, F. Besenbacher, B. Hammer, T. G. Pedersen, P. Hofmann, and L. Hornekaer, "Bandgap opening in graphene induced by patterned hydrogen adsorption," *Nature Materials*, vol. 9, pp. 315-319, Apr 2010.
- [18] C. Lee, X. D. Wei, J. W. Kysar, and J. Hone, "Measurement of the elastic properties and intrinsic strength of monolayer graphene," *Science*, vol. 321, pp. 385-388, Jul 18 2008.
- [19] I. W. Frank, D. M. Tanenbaum, A. M. Van der Zande, and P. L. McEuen, "Mechanical properties of suspended graphene sheets," *Journal of Vacuum Science & Technology B*, vol. 25, pp. 2558-2561, Nov 2007.
- [20] K. S. Kim, Y. Zhao, H. Jang, S. Y. Lee, J. M. Kim, K. S. Kim, J. H. Ahn, P. Kim, J. Y. Choi, and B. H. Hong, "Large-scale pattern growth of graphene films for stretchable transparent electrodes," *Nature*, vol. 457, pp. 706-710, Feb 5 2009.
- [21] J. S. Bunch, A. M. van der Zande, S. S. Verbridge, I. W. Frank, D. M. Tanenbaum, J. M. Parpia, H. G. Craighead, and P. L. McEuen, "Electromechanical resonators from graphene sheets," *Science*, vol. 315, pp. 490-493, Jan 26 2007.
- [22] A. D. Smith, F. Niklaus, A. Paussa, S. Vaziri, A. C. Fischer, M. Sterner, F. Forsberg, A. Delin, D. Esseni, P. Palestri, M. Ostling, and M. C. Lemme, "Electromechanical Piezoresistive Sensing in Suspended Graphene Membranes," *Nano Letters*, vol. 13, pp. 3237-3242, Jul 2013.

- [23] Y. H. Xu, C. Y. Chen, V. V. Deshpande, F. A. DiRenno, A. Gondarenko, D. B. Heinz, S. M. Liu, P. Kim, and J. Hone, "Radio frequency electrical transduction of graphene mechanical resonators," *Applied Physics Letters*, vol. 97, Dec 13 2010.
- [24] D. Garcia-Sanchez, A. M. van der Zande, A. S. Paulo, B. Lassagne, P. L. McEuen, and A. Bachtold, "Imaging mechanical vibrations in suspended graphene sheets," *Nano Letters*, vol. 8, pp. 1399-1403, May 2008.
- [25] R. R. Nair, P. Blake, A. N. Grigorenko, K. S. Novoselov, T. J. Booth, T. Stauber, N. M. R. Peres, and A. K. Geim, "Fine structure constant defines visual transparency of graphene," *Science*, vol. 320, pp. 1308-1308, Jun 6 2008.
- [26] G. Eda, Y. Y. Lin, C. Mattevi, H. Yamaguchi, H. A. Chen, I. S. Chen, C. W. Chen, and M. Chhowalla, "Blue Photoluminescence from Chemically Derived Graphene Oxide," *Advanced Materials*, vol. 22, pp. 505-+, Jan 26 2010.
- [27] Z. T. Luo, P. M. Vora, E. J. Mele, A. T. C. Johnson, and J. M. Kikkawa, "Photoluminescence and band gap modulation in graphene oxide," *Applied Physics Letters*, vol. 94, Mar 16 2009.
- [28] L. Ju, B. S. Geng, J. Horng, C. Girit, M. Martin, Z. Hao, H. A. Bechtel, X. G. Liang, A. Zettl, Y. R. Shen, and F. Wang, "Graphene plasmonics for tunable terahertz metamaterials," *Nature Nanotechnology*, vol. 6, pp. 630-634, Oct 2011.
- [29] F. Bonaccorso, Z. Sun, T. Hasan, and A. C. Ferrari, "Graphene photonics and optoelectronics," *Nature Photonics*, vol. 4, pp. 611-622, Sep 2010.
- [30] M. Pumera, "Electrochemistry of Graphene: New Horizons for Sensing and Energy Storage," *Chemical Record*, vol. 9, pp. 211-223, 2009.

- [31] W. R. Yang, K. R. Ratinac, S. P. Ringer, P. Thordarson, J. J. Gooding, and F. Braet, "Carbon Nanomaterials in Biosensors: Should You Use Nanotubes or Graphene?," *Angewandte Chemie-International Edition*, vol. 49, pp. 2114-2138, 2010.
- [32] K. R. Ratinac, W. R. Yang, J. J. Gooding, P. Thordarson, and F. Braet, "Graphene and Related Materials in Electrochemical Sensing," *Electroanalysis*, vol. 23, pp. 803-826, Apr 2011.
- [33] Y. W. Hu, F. H. Li, X. X. Bai, D. Li, S. C. Hua, K. K. Wang, and L. Niu, "Label-free electrochemical impedance sensing of DNA hybridization based on functionalized graphene sheets," *Chemical Communications*, vol. 47, pp. 1743-1745, 2011.
- [34] M. Zhou, Y. M. Zhai, and S. J. Dong, "Electrochemical Sensing and Biosensing Platform Based on Chemically Reduced Graphene Oxide," *Analytical Chemistry*, vol. 81, pp. 5603-5613, Jul 15 2009.
- [35] M. Pumera, A. Ambrosi, A. Bonanni, E. L. K. Chng, and H. L. Poh, "Graphene for electrochemical sensing and biosensing," *Trac-Trends in Analytical Chemistry*, vol. 29, pp. 954-965, Oct 2010.
- [36] A. Chou, T. Bocking, N. K. Singh, and J. J. Gooding, "Demonstration of the importance of oxygenated species at the ends of carbon nanotubes for their favourable electrochemical properties," *Chemical Communications*, pp. 842-844, 2005.

- [37] X. B. Ji, C. E. Banks, A. Crossley, and R. G. Compton, "Oxygenated edge plane sites slow the electron transfer of the ferro-/ferricyanide redox couple at graphite electrodes," *Chemphyschem*, vol. 7, pp. 1337-1344, Jun 12 2006.
- [38] M. Pumera, "The Electrochemistry of Carbon Nanotubes: Fundamentals and Applications," *Chemistry-a European Journal*, vol. 15, pp. 4970-4978, 2009.
- [39] J. Li, S. J. Guo, Y. M. Zhai, and E. K. Wang, "Nafion-graphene nanocomposite film as enhanced sensing platform for ultrasensitive determination of cadmium," *Electrochemistry Communications*, vol. 11, pp. 1085-1088, May 2009.
- [40] C. S. Shan, H. F. Yang, J. F. Song, D. X. Han, A. Ivaska, and L. Niu, "Direct Electrochemistry of Glucose Oxidase and Biosensing for Glucose Based on Graphene," *Analytical Chemistry*, vol. 81, pp. 2378-2382, Mar 15 2009.
- [41] N. Camara, G. Rius, J. R. Huntzinger, A. Tiberj, N. Mestres, P. Godignon, and J. Camassel, "Selective epitaxial growth of graphene on SiC," *Applied Physics Letters*, vol. 93, Sep 22 2008.
- [42] H. Huang, W. Chen, S. Chen, and A. T. S. Wee, "Bottom-up Growth of Epitaxial Graphene on 6H-SiC(0001)," *ACS nano*, vol. 2, pp. 2513-2518, Dec 2008.
- [43] A. Reina, X. T. Jia, J. Ho, D. Nezich, H. B. Son, V. Bulovic, M. S. Dresselhaus, and J. Kong, "Layer Area, Few-Layer Graphene Films on Arbitrary Substrates by Chemical Vapor Deposition," *Nano Letters*, vol. 9, pp. 3087-3087, Aug 2009.
- [44] Y. Zhang, L. M. G. De Arco, and C. W. Zhou, "Synthesis of large area single- and bilayer graphene on single crystalline nickel by chemical vapor deposition," *Abstracts of Papers of the American Chemical Society*, vol. 238, Aug 16 2009.

- [45] S. Stankovich, D. A. Dikin, R. D. Piner, K. A. Kohlhaas, A. Kleinhammes, Y. Jia, Y. Wu, S. T. Nguyen, and R. S. Ruoff, "Synthesis of graphene-based nanosheets via chemical reduction of exfoliated graphite oxide," *Carbon*, vol. 45, pp. 1558-1565, Jun 2007.
- [46] A. Reina, X. T. Jia, J. Ho, D. Nezich, H. B. Son, V. Bulovic, M. S. Dresselhaus, and J. Kong, "Large Area, Few-Layer Graphene Films on Arbitrary Substrates by Chemical Vapor Deposition," *Nano Letters*, vol. 9, pp. 30-35, Jan 2009.
- [47] L. Malic, T. Veres, and M. Tabrizian, "Biochip functionalization using electrowetting-on-dielectric digital microfluidics for surface plasmon resonance imaging detection of DNA hybridization," *Biosensors & Bioelectronics*, vol. 24, pp. 2218-2224, Mar 15 2009.
- [48] G. A. Lopez and E. Mittemeijer, "The solubility of C in solid Cu," *Scripta Materialia*, vol. 51, pp. 1-5, Jul 2004.
- [49] F. Schedin, A. K. Geim¹, S. V. Morozov, E. W. Hill, P. Blake, M. I. Katsnelson, and K. S. Novoselov¹, "Detection of individual gas molecules adsorbed on graphene," *Nature Mater.*, vol. 6, pp. 652-655, 2007.
- [50] A. C. Ferrari, J. C. Meyer, V. Scardaci, C. Casiraghi, M. Lazzeri, F. Mauri, S. Piscanec, D. Jiang, K. S. Novoselov, S. Roth, and A. K. Geim, "Raman spectrum of graphene and graphene layers," *Physical Review Letters*, vol. 97, Nov 3 2006.
- [51] F. Tuinstra and J. L. Koenig, "Raman Spectrum of Graphite," *Journal of Chemical Physics*, vol. 53, pp. 1126-&, 1970.
- [52] M. J. Allen, V. C. Tung, and R. B. Kaner, "Honeycomb Carbon: A Review of Graphene," *Chemical Reviews*, vol. 110, pp. 132-145, Jan 2010.

- [53] D. Graf, F. Molitor, K. Ensslin, C. Stampfer, A. Jungen, C. Hierold, and L. Wirtz, "Raman imaging of graphene," *Solid State Communications*, vol. 143, pp. 44-46, Jul 2007.
- [54] R. Martel, V. Derycke, C. Lavoie, J. Appenzeller, K. K. Chan, J. Tersoff, and P. Avouris, "Ambipolar electrical transport in semiconducting single-wall carbon nanotubes," *Physical Review Letters*, vol. 87, Dec 17 2001.
- [55] A. Colli, A. Fasoli, P. Beecher, P. Servati, S. Pisana, Y. Fu, A. J. Flewitt, W. I. Milne, J. Robertson, C. Ducati, S. De Franceschi, S. Hofmann, and A. C. Ferrari, "Thermal and chemical vapor deposition of Si nanowires: Shape control, dispersion, and electrical properties," *Journal of Applied Physics*, vol. 102, Aug 1 2007.
- [56] J. C. Charlier, P. C. Eklund, J. Zhu, and A. C. Ferrari, "Electron and phonon properties of graphene: Their relationship with carbon nanotubes," *Carbon Nanotubes*, vol. 111, pp. 673-709, 2008.
- [57] F. Schedin, A. K. Geim, S. V. Morozov, E. W. Hill, P. Blake, M. I. Katsnelson, and K. S. Novoselov, "Detection of individual gas molecules adsorbed on graphene," *Nature Materials*, vol. 6, pp. 652-655, Sep 2007.
- [58] A. K. Geim and K. S. Novoselov, "The rise of graphene," *Nature Materials*, vol. 6, pp. 183-191, Mar 2007.
- [59] X. Wang, L. J. Zhi, and K. Mullen, "Transparent, conductive graphene electrodes for dye-sensitized solar cells," *Nano Letters*, vol. 8, pp. 323-327, Jan 2008.
- [60] P. Blake, P. D. Brimicombe, R. R. Nair, T. J. Booth, D. Jiang, F. Schedin, L. A. Ponomarenko, S. V. Morozov, H. F. Gleeson, E. W. Hill, A. K. Geim, and K. S.

- Novoselov, "Graphene-based liquid crystal device," *Nano Letters*, vol. 8, pp. 1704-1708, Jun 2008.
- [61] S. Bae, H. Kim, Y. Lee, X. F. Xu, J. S. Park, Y. Zheng, J. Balakrishnan, T. Lei, H. R. Kim, Y. I. Song, Y. J. Kim, K. S. Kim, B. Ozyilmaz, J. H. Ahn, B. H. Hong, and S. Iijima, "Roll-to-roll production of 30-inch graphene films for transparent electrodes," *Nature Nanotechnology*, vol. 5, pp. 574-578, Aug 2010.
- [62] S. P. Pang, Y. Hernandez, X. L. Feng, and K. Mullen, "Graphene as Transparent Electrode Material for Organic Electronics," *Advanced Materials*, vol. 23, pp. 2779-2795, Jul 5 2011.
- [63] G. Jo, M. Choe, S. Lee, W. Park, Y. H. Kahng, and T. Lee, "The application of graphene as electrodes in electrical and optical devices," *Nanotechnology*, vol. 23, Mar 23 2012.
- [64] S. Ghosh, I. Calizo, D. Teweldebrhan, E. P. Pokatilov, D. L. Nika, A. A. Balandin, W. Bao, F. Miao, and C. N. Lau, "Extremely high thermal conductivity of graphene: Prospects for thermal management applications in nanoelectronic circuits," *Appl. Phys. Lett.*, vol. 92, p. 151911, 2008.
- [65] J. H. Seol, I. Jo, A. L. Moore, L. Lindsay, Z. H. Aitken, M. T. Pettes, X. Li, Z. Yao, R. Huang, D. Broido, N. Mingo, R. S. Ruoff, and L. Shi, "Two-Dimensional Phonon Transport in Supported Graphene," *Science*, vol. 328, pp. 213-216, April 9, 2010 2010.
- [66] K. I. Bolotin, K. J. Sikes, Z. Jiang, M. Klima, G. Fudenberg, J. Hone, P. Kim, and H. L. Stormer, "Ultrahigh electron mobility in suspended graphene," *Solid State Commun.*, vol. 146, pp. 351-355, 2008.

- [67] L. A. Ponomarenko, F. Schedin, M. I. Katsnelson, R. Yang, E. W. Hill, K. S. Novoselov, and A. K. Geim, "Chaotic Dirac Billiard in Graphene Quantum Dots," *Science*, vol. 320, pp. 356-358, April 18, 2008 2008.
- [68] J.-H. Chen, C. Jang, S. Xiao, M. Ishigami, and M. S. Fuhrer, "Intrinsic and extrinsic performance limits of graphene devices on SiO₂," *Nat Nano*, vol. 3, pp. 206-209, 2008.
- [69] F. Chen, J. Xia, D. K. Ferry, and N. Tao, "Dielectric Screening Enhanced Performance in Graphene FET," *Nano Letters*, vol. 9, pp. 2571-2574, 2009.
- [70] F. Schedin, A. K. Geim, S. V. Morozov, E. W. Hill, P. Blake, M. I. Katsnelson, and K. S. Novoselov, "Detection of individual gas molecules adsorbed on graphene," *Nature Mater.*, vol. 6, pp. 652-655, 2007.
- [71] P. K. Ang, W. Chen, A. T. S. Wee, and K. P. Loh, "Solution-Gated Epitaxial Graphene as pH Sensor," *Journal of the American Chemical Society*, vol. 130, pp. 14392-14393, Nov 5 2008.
- [72] Y. Y. Shao, J. Wang, H. Wu, J. Liu, I. A. Aksay, and Y. H. Lin, "Graphene Based Electrochemical Sensors and Biosensors: A Review," *Electroanalysis*, vol. 22, pp. 1027-1036, May 2010.
- [73] W. Y. Fu, C. Nef, O. Knopfnacher, A. Tarasov, M. Weiss, M. Calame, and C. Schonenberger, "Graphene Transistors Are Insensitive to pH Changes in Solution," *Nano Letters*, vol. 11, pp. 3597-3600, Sep 2011.
- [74] J. Ristein, W. Y. Zhang, F. Speck, M. Ostler, L. Ley, and T. Seyller, "Characteristics of solution gated field effect transistors on the basis of epitaxial

- graphene on silicon carbide," *Journal of Physics D-Applied Physics*, vol. 43, p. 345303, Sep 1 2010.
- [75] Z. G. Cheng, Q. Li, Z. J. Li, Q. Y. Zhou, and Y. Fang, "Suspended Graphene Sensors with Improved Signal and Reduced Noise," *Nano Letters*, vol. 10, pp. 1864-1868, May 2010.
- [76] Y. Ohno, K. Maehashi, Y. Yamashiro, and K. Matsumoto, "Electrolyte-Gated Graphene Field-Effect Transistors for Detecting pH Protein Adsorption," *Nano Letters*, vol. 9, pp. 3318-3322, Sep 2009.
- [77] I. Heller, S. Chatoor, J. Mannik, M. A. G. Zevenbergen, C. Dekker, and S. G. Lemay, "Influence of Electrolyte Composition on Liquid-Gated Carbon Nanotube and Graphene Transistors," *Journal of the American Chemical Society*, vol. 132, pp. 17149-17156, Dec 8 2010.
- [78] L. Larrimore, S. Nad, X. J. Zhou, H. Abruna, and P. L. McEuen, "Probing electrostatic potentials in solution with carbon nanotube transistors," *Nano Letters*, vol. 6, pp. 1329-1333, Jul 12 2006.
- [79] J. A. Robinson, E. S. Snow, S. C. Badescu, T. L. Reinecke, and F. K. Perkins, "Role of defects in single-walled carbon nanotube chemical sensors," *Nano Letters*, vol. 6, pp. 1747-1751, Aug 9 2006.
- [80] A. C. Ferrari, "Raman spectroscopy of graphene and graphite: Disorder, electron-phonon coupling, doping and nonadiabatic effects," *Solid State Communications*, vol. 143, pp. 47-57, Jul 2007.

- [81] X. Wang, X. Li, L. Zhang, Y. Yoon, P. K. Weber, H. Wang, J. Guo, and H. Dai, "N-Doping of Graphene Through Electrothermal Reactions with Ammonia," *Science*, vol. 324, pp. 768-771, May 8, 2009.
- [82] K. Brenner, Y. X. Yang, and R. Murali, "Edge doping of graphene sheets," *Carbon*, vol. 50, pp. 637-645, Feb 2012.
- [83] A. Salehi-Khojin, D. Estrada, K. Y. Lin, M. H. Bae, F. Xiong, E. Pop, and R. I. Masel, "Polycrystalline Graphene Ribbons as Chemiresistors," *Advanced Materials*, vol. 24, pp. 53-57, Jan 2012.
- [84] M.-W. Lin, C. Ling, L. A. Agapito, N. Kioussis, Y. Zhang, M. M.-C. Cheng, W. L. Wang, E. Kaxiras, and Z. Zhou, "Approaching the intrinsic band gap in suspended high-mobility graphene nanoribbons," *Phys. Rev. B*, vol. 84, p. 125411, 2011.
- [85] X. S. Li, W. W. Cai, J. H. An, S. Kim, J. Nah, D. X. Yang, R. Piner, A. Velamakanni, I. Jung, E. Tutuc, S. K. Banerjee, L. Colombo, and R. S. Ruoff, "Large-Area Synthesis of High-Quality and Uniform Graphene Films on Copper Foils," *Science*, vol. 324, pp. 1312-1314, Jun 5 2009.
- [86] X. L. Liang, B. A. Sperling, I. Calizo, G. J. Cheng, C. A. Hacker, Q. Zhang, Y. Obeng, K. Yan, H. L. Peng, Q. L. Li, X. X. Zhu, H. Yuan, A. R. H. Walker, Z. F. Liu, L. M. Peng, and C. A. Richter, "Toward Clean and Crackless Transfer of Graphene," *ACS nano*, vol. 5, pp. 9144-9153, Nov 2011.
- [87] Y. P. Dan, Y. Lu, N. J. Kybert, Z. T. Luo, and A. T. C. Johnson, "Intrinsic Response of Graphene Vapor Sensors," *Nano Letters*, vol. 9, pp. 1472-1475, Apr 2009.

- [88] X. R. Wang, S. M. Tabakman, and H. J. Dai, "Atomic layer deposition of metal oxides on pristine and functionalized graphene," *Journal of the American Chemical Society*, vol. 130, pp. 8152-8153, Jul 2 2008.
- [89] T. Fang, A. Konar, H. L. Xing, and D. Jena, "Carrier statistics and quantum capacitance of graphene sheets and ribbons," *Applied Physics Letters*, vol. 91, p. 092109, Aug 27 2007.
- [90] J. Guo, Y. Yoon, and Y. Ouyang, "Gate electrostatics and quantum capacitance of graphene nanoribbons," *Nano Letters*, vol. 7, pp. 1935-1940, Jul 2007.
- [91] A. C. Ferrari, J. C. Meyer, V. Scardaci, C. Casiraghi, M. Lazzeri, F. Mauri, S. Piscanec, D. Jiang, K. S. Novoselov, S. Roth, and A. K. Geim, "Raman Spectrum of Graphene and Graphene Layers," *Physical Review Letters*, vol. 97, p. 187401, 2006.
- [92] A. Salehi-Khojin, C. R. Field, J. Yeom, and R. I. Masel, "Sensitivity of nanotube chemical sensors at the onset of Poole-Frenkel conduction," *Applied Physics Letters*, vol. 96, p. 163110, Apr 19 2010.
- [93] A. Pirkle, J. Chan, A. Venugopal, D. Hinojos, C. W. Magnuson, S. McDonnell, L. Colombo, E. M. Vogel, R. S. Ruoff, and R. M. Wallace, "The effect of chemical residues on the physical and electrical properties of chemical vapor deposited graphene transferred to SiO₂," *Applied Physics Letters*, vol. 99, p. 122108, Sep 19 2011.
- [94] N. Mohanty and V. Berry, "Graphene-Based Single-Bacterium Resolution Biodevice and DNA Transistor: Interfacing Graphene Derivatives with Nanoscale and Microscale Biocomponents," *Nano Letters*, vol. 8, pp. 4469-4476, Dec 2008.

- [95] M. S. Mannoor, H. Tao, J. D. Clayton, A. Sengupta, D. L. Kaplan, R. R. Naik, N. Verma, F. G. Omenetto, and M. C. McAlpine, "Graphene-based wireless bacteria detection on tooth enamel," *Nature Communications*, vol. 3, Mar 2012.
- [96] Y. X. Huang, X. C. Dong, Y. X. Liu, L. J. Li, and P. Chen, "Graphene-based biosensors for detection of bacteria and their metabolic activities," *Journal of Materials Chemistry*, vol. 21, pp. 12358-12362, 2011.
- [97] H. Handa, S. Gurczynski, M. P. Jackson, G. Auner, J. Walker, and G. Mao, "Recognition of *Salmonella typhimurium* by immobilized phage P22 monolayers," *Surface Science*, vol. 602, pp. 1392-1400, Apr 1 2008.
- [98] A. Singh, S. K. Arya, N. Glass, P. Hanifi-Moghaddam, R. Naidoo, C. M. Szymanski, J. Tanha, and S. Evoy, "Bacteriophage tailspike proteins as molecular probes for sensitive and selective bacterial detection," *Biosensors & Bioelectronics*, vol. 26, pp. 131-138, Sep 15 2010.
- [99] X. Tan, H.-J. Chuang, M.-W. Lin, Z. Zhou, and M. M.-C. Cheng, "Edge Effects on the pH Response of Graphene Nanoribbon Field Effect Transistors," *The Journal of Physical Chemistry C*, 2013.
- [100] P. Nguyen and V. Berry, "Graphene Interfaced with Biological Cells: Opportunities and Challenges," *Journal of Physical Chemistry Letters*, vol. 3, pp. 1024-1029, Apr 19 2012.
- [101] Q. S. Luo, H. Wang, X. H. Zhang, and Y. Qian, "Effect of direct electric current on the cell surface properties of phenol-degrading bacteria," *Applied and Environmental Microbiology*, vol. 71, pp. 423-427, Jan 2005.

- [102] K. A. Soni, A. K. Balasubramanian, A. Beskok, and S. D. Pillai, "Zeta potential of selected bacteria in drinking water when dead, starved, or exposed to minimal and rich culture media," *Current Microbiology*, vol. 56, pp. 93-97, Jan 2008.
- [103] B. K. Li and B. E. Logan, "Impact of ultraviolet light on bacterial adhesion to glass and metal-oxide coated surfaces.," *Abstracts of Papers of the American Chemical Society*, vol. 228, pp. U547-U547, Aug 22 2004.
- [104] M. H. Yang and S. Q. Gong, "Immunosensor for the detection of cancer biomarker based on percolated graphene thin film," *Chemical Communications*, vol. 46, pp. 5796-5798, 2010.
- [105] T. Fang, A. Konar, H. L. Xing, and D. Jena, "Carrier statistics and quantum capacitance of graphene sheets and ribbons," *Applied Physics Letters*, vol. 91, Aug 27 2007.
- [106] H. Moon, S. K. Cho, R. L. Garrell, and C. J. Kim, "Low voltage electrowetting-on-dielectric," *Journal of Applied Physics*, vol. 92, pp. 4080-4087, Oct 1 2002.
- [107] F. Mugele and J. C. Baret, "Electrowetting: From basics to applications," *Journal of Physics-Condensed Matter*, vol. 17, pp. R705-R774, Jul 20 2005.
- [108] S. K. Cho, H. J. Moon, and C. J. Kim, "Creating, transporting, cutting, and merging liquid droplets by electrowetting-based actuation for digital microfluidic circuits," *Journal of Microelectromechanical Systems*, vol. 12, pp. 70-80, Feb 2003.
- [109] V. Srinivasan, V. K. Pamula, and R. B. Fair, "An integrated digital microfluidic lab-on-a-chip for clinical diagnostics on human physiological fluids," *Lab on a Chip*, vol. 4, pp. 310-315, 2004.

- [110] R. B. Fair, "Digital microfluidics: is a true lab-on-a-chip possible?," *Microfluidics and Nanofluidics*, vol. 3, pp. 245-281, Jun 2007.
- [111] S. K. Cho and H. Moon, "Electrowetting on dielectric (EWOD): New tool for bio/micro fluids handling," *Biochip Journal*, vol. 2, pp. 79-96, Jun 20 2008.
- [112] L. Clime, D. Brassard, and T. Veres, "Numerical modeling of electrowetting transport processes for digital microfluidics," *Microfluidics and Nanofluidics*, vol. 8, pp. 599-608, May 2010.
- [113] M. Abdelgawad and A. R. Wheeler, "The Digital Revolution: A New Paradigm for Microfluidics," *Advanced Materials*, vol. 21, pp. 920-925, Feb 23 2009.
- [114] B. Berge and J. Peseux, "Variable focal lens controlled by an external voltage: An application of electrowetting," *European Physical Journal E*, vol. 3, pp. 159-163, Oct 2000.
- [115] F. Krogmann, W. Monch, and H. Zappe, "Electrowetting for Tunable Microoptics," *Journal of Microelectromechanical Systems*, vol. 17, pp. 1501-1512, Dec 2008.
- [116] M. A. Bucaro, P. R. Kolodner, J. A. Taylor, A. Sidorenko, J. Aizenberg, and T. N. Krupenkin, "Tunable Liquid Optics: Electrowetting-Controlled Liquid Mirrors Based on Self-Assembled Janus Tiles," *Langmuir*, vol. 25, pp. 3876-3879, Mar 17 2009.
- [117] C. U. Murade, J. M. Oh, D. van den Ende, and F. Mugele, "Electrowetting driven optical switch and tunable aperture," *Optics Express*, vol. 19, pp. 15525-15531, Aug 1 2011.

- [118] R. A. Hayes and B. J. Feenstra, "Video-speed electronic paper based on electrowetting," *Nature*, vol. 425, pp. 383-385, Sep 25 2003.
- [119] A. Giraldo, J. Aubert, N. Bergeron, E. Derckx, B. J. Feenstra, R. Massard, J. Mans, A. Slack, and P. Vermeulen, "Transmissive electrowetting-based displays for portable multimedia devices," *Journal of the Society for Information Display*, vol. 18, pp. 317-325, Apr 2010.
- [120] D. Y. Kim and A. J. Steckl, "Electrowetting on Paper for Electronic Paper Display," *Acs Applied Materials & Interfaces*, vol. 2, pp. 3318-3323, Nov 2010.
- [121] K. Zhou and J. Heikenfeld, "Arrayed electrowetting microwells," *Applied Physics Letters*, vol. 92, Mar 17 2008.
- [122] J. Y. Yoon and R. L. Garrell, "Preventing biomolecular adsorption in electrowetting-based biofluidic chips," *Analytical Chemistry*, vol. 75, pp. 5097-5102, Oct 1 2003.
- [123] S. K. Fan, P. W. Huang, T. T. Wang, and Y. H. Peng, "Cross-scale electric manipulations of cells and droplets by frequency-modulated dielectrophoresis and electrowetting," *Lab on a Chip*, vol. 8, pp. 1325-1331, Aug 2008.
- [124] S. Yamaguchi, K. Morimoto, J. Fukuda, and H. Suzuki, "Electrowetting-based pH- and biomolecule-responsive valves and pH filters," *Biosensors & Bioelectronics*, vol. 24, pp. 2171-2176, Mar 15 2009.
- [125] L. B. Hu, G. Gruner, J. Gong, C. J. Kim, and B. Hornbostel, "Electrowetting devices with transparent single-walled carbon nanotube electrodes," *Applied Physics Letters*, vol. 90, Feb 26 2007.

- [126] H. Kim, C. M. Gilmore, A. Pique, J. S. Horwitz, H. Mattoussi, H. Murata, Z. H. Kafafi, and D. B. Chrisey, "Electrical, optical, and structural properties of indium-tin-oxide thin films for organic light-emitting devices," *Journal of Applied Physics*, vol. 86, pp. 6451-6461, Dec 1 1999.
- [127] L. G. De Arco, Y. Zhang, C. W. Schlenker, K. Ryu, M. E. Thompson, and C. W. Zhou, "Continuous, Highly Flexible, and Transparent Graphene Films by Chemical Vapor Deposition for Organic Photovoltaics," *ACS nano*, vol. 4, pp. 2865-2873, May 2010.
- [128] X. B. Wang, H. J. You, F. M. Liu, M. J. Li, L. Wan, S. Q. Li, Q. Li, Y. Xu, R. Tian, Z. Y. Yu, D. Xiang, and J. Cheng, "Large-Scale Synthesis of Few-Layered Graphene using CVD," *Chemical Vapor Deposition*, vol. 15, pp. 53-56, Mar 2009.
- [129] Y. W. Zhu, S. Murali, W. W. Cai, X. S. Li, J. W. Suk, J. R. Potts, and R. S. Ruoff, "Graphene and Graphene Oxide: Synthesis, Properties, and Applications," *Advanced Materials*, vol. 22, pp. 3906-3924, Sep 15 2010.
- [130] J. Beermann, T. Sondergaard, S. M. Novikov, S. I. Bozhevolnyi, E. Devaux, and T. W. Ebbesen, "Field enhancement and extraordinary optical transmission by tapered periodic slits in gold films," *New Journal of Physics*, vol. 13, Jun 17 2011.
- [131] A. B. Kuzmenko, E. van Heumen, F. Carbone, and D. van der Marel, "Universal optical conductance of graphite," *Physical Review Letters*, vol. 100, Mar 21 2008.
- [132] C. W. Baek, Y. K. Kim, Y. Ahn, and Y. H. Kim, "Measurement of the mechanical properties of electroplated gold thin films using micromachined beam structures," *Sensors and Actuators a-Physical*, vol. 117, pp. 17-27, Jan 3 2005.

- [133] D. G. Neerincx and T. J. Vink, "Depth profiling of thin ITO films by grazing incidence X-ray diffraction," *Thin Solid Films*, vol. 278, pp. 12-17, May 15 1996.
- [134] B. Wu, A. Heidelberg, and J. J. Boland, "Mechanical properties of ultrahigh-strength gold nanowires," *Nature Materials*, vol. 4, pp. 525-529, Jul 2005.
- [135] C. J. Chiang, C. Winscom, S. Bull, and A. Monkman, "Mechanical modeling of flexible OLED devices," *Organic Electronics*, vol. 10, pp. 1268-1274, Nov 2009.
- [136] R. A. Serway, *Principles of Physics*: Saunders College Pub, 1998.
- [137] C. G. Granqvist and A. Hultaker, "Transparent and conducting ITO films: new developments and applications," *Thin Solid Films*, vol. 411, pp. 1-5, May 22 2002.
- [138] L. Colombo, X. S. Li, W. W. Cai, J. H. An, S. Kim, J. Nah, D. X. Yang, R. Piner, A. Velamakanni, I. Jung, E. Tutuc, S. K. Banerjee, and R. S. Ruoff, "Large-Area Synthesis of High-Quality and Uniform Graphene Films on Copper Foils," *Science*, vol. 324, pp. 1312-1314, Jun 5 2009.
- [139] Y.-C. Lin, C.-C. Lu, C.-H. Yeh, C. Jin, K. Suenaga, and P.-W. Chiu, "Graphene Annealing: How Clean Can It Be?," *Nano Letters*, vol. 12, pp. 414-419, 2012/01/11 2011.
- [140] M. P. Levendorf, C. S. Ruiz-Vargas, S. Garg, and J. Park, "Transfer-Free Batch Fabrication of Single Layer Graphene Transistors," *Nano Letters*, vol. 9, pp. 4479-4483, Dec 2009.
- [141] P. E. Hopkins, M. Baraket, E. V. Barnat, T. E. Beechem, S. P. Kearney, J. C. Duda, J. T. Robinson, and S. G. Walton, "Manipulating Thermal Conductance at Metal-Graphene Contacts via Chemical Functionalization," *Nano Letters*, 2012.

- [142] O. Ozdemir, S. I. Karakashev, A. V. Nguyen, and J. D. Miller, "Adsorption and surface tension analysis of concentrated alkali halide brine solutions," *Minerals Engineering*, vol. 22, pp. 263-271, Feb 2009.
- [143] J. Ralston, A. Quinn, and R. Sedev, "Contact angle saturation in electrowetting," *Journal of Physical Chemistry B*, vol. 109, pp. 6268-6275, Apr 7 2005.
- [144] H. J. J. Verheijen and M. W. J. Prins, "Reversible electrowetting and trapping of charge: Model and experiments," *Langmuir*, vol. 15, pp. 6616-6620, Sep 28 1999.
- [145] P. Zoltowski, "On the electrical capacitance of interfaces exhibiting constant phase element behaviour," *Journal of Electroanalytical Chemistry*, vol. 443, pp. 149-154, 1998.
- [146] J. D. Weiland and D. J. Anderson, "Chronic neural stimulation with thin-film, iridium oxide electrodes," *Biomedical Engineering, IEEE Transactions on*, vol. 47, pp. 911-918, 2000.
- [147] F. Saeki, J. Baum, H. Moon, J. Y. Yoon, C. J. Kim, and R. L. Garrell, "Electrowetting on dielectrics (EWOD): reducing voltage requirements for microfluidics," *Polymeric Materials Science and Engineering*, vol. 85, pp. 12-13, 2001.
- [148] G. E. Loeb, M. J. Bak, M. Salcman, and E. M. Schmidt, "Parylene as a Chronically Stable, Reproducible Microelectrode Insulator," *Ieee Transactions on Biomedical Engineering*, vol. 24, pp. 121-128, 1977.
- [149] X. B. Tan, Z. X. Zhou, and M. M. C. Cheng, "Electrowetting on dielectric experiments using graphene," *Nanotechnology*, vol. 23, Sep 21 2012.

- [150] J. Lee, H. Moon, J. Fowler, T. Schoellhammer, and C. J. Kim, "Electrowetting and electrowetting-on-dielectric for microscale liquid handling," *Sensors and Actuators a-Physical*, vol. 95, pp. 259-268, Jan 1 2002.

ABSTRACT**THE APPLICATION OF GRAPHENE FILMS IN BIOSENSING AND ELECTROWETTING**

by

XUEBIN TAN**May 2014****Advisor:** Dr. Mark Ming-Cheng Cheng**Major:** Electrical Engineering**Degree:** Doctor of Philosophy

In recent years, graphene has been found to possess extraordinary electronic, optical, mechanical and electrochemical properties. Graphene is optically transparent and mechanically flexible, and has high electron mobility and conductivity. In this thesis, we propose to investigate graphene's properties in the detection of biomolecules as well as the manipulation of biological samples. Graphene without defects has high charge carrier mobility and surface areas, which is ideal for biosensors. However, literature shows a lot of variations in the measurements using graphene biosensors. In addition, the surface functionalization of graphene in order to enhance the specificity has not been fully investigated yet. We propose to combine e-beam lithography (EBL) and dry etching to generate edge defects for biosensor application. These edge defects not only enhance sensitivity but also control the binding sites for surface functionalization. We also demonstrate, for the first time, a microfluidic device based on electrowetting-on-dielectric (EWOD) using a graphene electrode. Hydrophobic surfaces of graphene facilitate self-assembly of the hydrophobic dielectric layer (Teflon). Using graphene

electrode, we are able to achieve robust and reversible changes in contact angle without electrolysis. Graphene enables the manipulation of droplets on flexible and transparent substrates using low-cost PET (polyethylene terephthalate). With its high optical transparency, mechanical flexibility and excellent electrical properties, graphene may be suitable in the manipulation of biological samples and in the detection of biomolecules. The research may be applicable in the development of the next generation point-of-care device.

AUTOBIOGRAPHICAL STATEMENT

XUEBIN TAN

Education

2009-2014 Doctor of Philosophy, Wayne State University, Detroit, MI, USA

2006~2009 Master Degree in Engineering, Southeast University, Nanjing, P.R. China

2002-2006 Bachelor Degree in Engineering, National University of Defense Technology,
Changsha, P. R. China

Honors and Awards

Wayne State University Summer 2013 Dissertation Fellowship

Andrzej Olbrot Travel Award for Excellence in Graduate Student Research

Thomas Rumble University Graduate Fellowship

IEEE MEMS conference student travel award funded by NSF and TRF

Selected Journal Publications

1. Tan, X.; Chuang, H.; Lin, M.; Zhou, Z.; and Cheng, M., Edge effects on the pH Response of Graphene-nanoribbon field-effect Transistors. *J. Phys. Chem. C*, 2013, 115(51), 27155
2. Tan, X.; Zhou, Z.; Cheng, M. M.-C., Electrowetting on dielectric experiments using graphene. *Nanotechnology*, 2012, 23 (37), 375501